



KU LEUVEN

ARENBERG DOCTORAL SCHOOL
FACULTY OF SCIENCE

Study of natural and synthetic polymer
systems by advanced microscopy
techniques

Tiago Andrade Chimenez

Supervisors:

Prof. Marcelo H. Gehlen

Prof. Johan Hofkens

Thesis presented in partial
fulfilment of the requirements for the
degree of PhD in Science

2016

Tiago Andrade Chimenez

Estudos de sistemas poliméricos naturais e sintéticos utilizando técnicas
avançadas de microscopia

Tese apresentada ao Instituto de Química de São Carlos da
Universidade de São Paulo e à Faculdade de Ciências da
Katholieke Universiteit Leuven como parte dos requisitos para a
obtenção do título de doutor em ciências

Área de concentração: Físico-Química

Orientadores: Prof. Dr. Marcelo Henrique Gehlen e Prof. Dr.
Johan Hofkens

São Carlos
2016

“Over a long period of time, the main force in favor of greater equality has been the diffusion of knowledge and skills.” Thomas Piketty

ACKNOWLEDGMENTS

I would like to use this space to express my gratitude to some people. First of all, I would like to thank my promoters, Prof. Marcelo H. Gehlen and Prof. Johan Hofkens. Thanks to them, I had the opportunity to perform my research in laboratories equipped with state-of-the-art microscopes. I would also like to thank Prof. Frans De Schryver and Prof. Hiroshi Uji-I for accepting to be my assessors at KU Leuven.

My thanks to the CAPES and CNPq for the scholarship granted during my Ph.D.

I would also like to thank Prof. Antonio Aprigio da Silva Curvelo for have given the sugarcane bagasse samples used in some studies and for all support and discussion about topics related to sugarcane bagasse.

I would like to thank Magda and Karel for all support they gave me when I started to work with polymerization of styrene in KU Leuven. I would also like to thank Daniel Jänsch from Max Planck Institute for providing the NMP initiator samples.

I have a lot to thank to Leen Cuyppers and Alexandre Mazzola, who helped in the establishment of the dual joint doctorate by USP and KU Leuven. Many thanks to Diego Lencione for all support related to the optical instrumentation.

I would also like to give my gratitude to those who have been working around the lab during the last years. I would like to mention some people that in some way have contributed to my PhD: Irlon, Isac, Vagner, Carlão, Adriel, Mafrinha, Camilo, Ronaldo, Carol, Anderson, Aline, Rafael, Renato, Paulo, Papako, Edson, Patricia, Stoyan, Kris, Eduardo, Ann Petré, Carine, Marino, Karolien, Wouter B, Elke, Bart, Stijn, Wouter S.

I would also like to take this opportunity to express my gratitude to my whole family. Special thanks to my mother Cida, my sister Talita, and my cousin Bruno. Without their support, I would never get up here.

The last but not least acknowledgement is going to Milena. The person who has been at my side since my first day in the lab. Thank you so much for everything, I have no words to describe how important you are in my life.

PREFACE

This PhD thesis was initiated in the first half of 2011 in the Laboratory of Molecular Fluorescence (LFM/IQSC), under supervision of Prof. Marcelo H. Gehlen. The two first chapters are related to the study of sugarcane bagasse by autofluorescence confocal microscopy and to the optical microscopy characterization of nanocrystalline cellulose.

From July 2013 to July 2014, a sandwich doctorate was performed in the Laboratory for Photochemistry and Spectroscopy from KU Leuven/Belgium, under supervision of Prof. Johan Hofkens. During this period, a study related to the nitroxide-based polymerization of styrene was performed, in which single-molecule spectroscopy and microscopy such as FCS and WFM were used. This stage of the research is described in Chapter 4.

On the way back to LFM, in Brazil, a FCS setup was implemented and a study of diffusion properties of nanocrystalline cellulose fluorescently labelled was performed, which is described in Chapter 3.

Therefore, this thesis is divided in four chapters. Each chapter contains, respectively, abstract, introduction, experimental part, results and discussion and, conclusion.

ABSTRACT

In the first chapter, the spatial distribution of fluorescent compounds in the sugarcane bagasse matrix is investigated by confocal fluorescence microscopy and spectroscopy with one and two-photon excitation. Autofluorescence images, emission spectra and fluorescence lifetime measurements provided a tool for the characterization of natural bagasse samples. Moreover, the technique allows the following of processes related to the lignin removal.

Nanocrystalline cellulose (NCC) is a rod-shaped nanofibre with 1–100 nm in diameter, and tens to hundreds of nanometres in length. In Chapter 2, NCC was obtained via sulphuric acid hydrolysis from Avicel®. Afterwards, the material was characterized by classic electronic microscopy SEM and TEM, confirming the rod-shaped morphology and the nano-sized structure. Conventional wide field microscopy was used as fluorescence microscopy tool in the characterization of NCC, when dispersed in polymeric solutions of PVA and PVP. The last part of Chapter 2 describes the characterization of NCC structures by using the super-resolution fluorescence microscopy STED (Stimulated Emission Depletion). The STED images showed a resolution down to 50 nm, allowing the comparison with TEM and AFM microscopy results.

In Chapter 3, the NCC was covalently labelled, by a click-chemistry reaction, with the ATTO-532 dye. Properties related to diffusion coefficient of NCC were determined by Fluorescence Correlation Spectroscopy (FCS). The diffusion of NCC dispersed in solution of PEG, containing different amounts polymer, was also studied by FCS and WFM methods. The use of spectroscopy and microscopy imaging techniques revealed

heterogeneity details of NCC dispersions, which are related to the hydrophilic and hydrophobic properties of the polymer solution.

In Chapter 4, it is presented a study of controlled radical polymerization by fluorescence correlation spectroscopy (FCS) and wide-field fluorescence microscopy (WFM). These techniques were used to determine the diffusion coefficients of growing polymer chains, during the controlled radical polymerization process. Linear and star-shaped polystyrene were grown via nitroxide-mediated polymerization (NMP) from alkoxyamine-based initiators containing a highly fluorescent perylene diimide moiety. We demonstrate that direct investigation of heterogeneity emerging during a controlled radical polymerization process by means of fluorescence of single-molecule chain initiator allows to obtain unravelling information related to the diffusion processes of the growing polymer chain.

RESUMO

O bagaço de cana-de-açúcar é um abundante coproduto obtido a partir da produção convencional de etanol. No entanto, o bagaço vem se mostrando como uma importante fonte para a produção de etanol de segunda geração. No primeiro capítulo da tese é apresentado um estudo referente à distribuição espacial dos compostos na matriz de bagaço de cana-de-açúcar. A investigação foi realizada utilizando microscopia de fluorescência confocal e espectroscopia por excitação com um e dois fótons. Imagens de autofluorescência em combinação com as medidas de fluorescência e tempos de vida forneceram uma gama de informações necessárias para a caracterização de amostras de bagaço. Além disso, a técnica permite o acompanhamento de processos relacionados com a remoção de lignina.

A nanocelulose cristalina (NCC) é um material promissor devido as suas propriedades intrínsecas, tais como seu formato alongado, medindo de 1 a 100 nm de diâmetro e seu comprimento variando de algumas dezenas a centenas de nanômetros. No capítulo 2, a nanocelulose cristalina foi obtida através da hidrólise da celulose cristalina (de Avicel®) com ácido sulfúrico. Em seguida, o material foi caracterizado por técnicas de microscopia SEM e TEM, confirmando a morfologia em forma de haste e a estrutura de tamanho nanométrico. A microscopia de campo largo convencional foi utilizada como ferramenta na caracterização da NCC dispersa em soluções poliméricas de PVA e PVP. A última parte do capítulo 2 descreve a caracterização de estruturas de NCC usando a microscopia de super-resolução de fluorescência STED (depleção de emissão estimulada). As imagens mostraram uma resolução de até 50 nm, permitindo a comparação com resultados de TEM e AFM.

No capítulo 3, a nanocelulose cristalina foi covalentemente marcada com o corante ATTO-532, através da chamada reação “click”. As propriedades relacionadas com o coeficiente de difusão da NCC foram determinadas por espectroscopia de correlação de fluorescência (FCS). Em uma etapa posterior, a NCC foi colocada em diferentes soluções do polímero PEG, contendo quantidades diferentes. As propriedades dinâmicas foram analisadas por métodos de FCS e WFM. O uso de técnicas de espectroscopia e microscopia revelou detalhes relacionados à heterogeneidade das dispersões de NCC, as quais estão relacionadas com as propriedades hidrofílicas e hidrofóbicas das soluções poliméricas.

LIST OF ABBREVIATIONS

AAc – Acid ascorbic

AFM - Atomic force microscopy

APD - Avalanche photodiode detector

ATRP - Atom transfer radical polymerization

BF - Bleached fibre

BP - Bleached pith

BS - Beam splitter

BWB - Bleached whole bagasse

CAA - Camera assembly attached

CAQUI - Central Analítica de Química

CCD - Charge coupled device

CRP - Controlled radical polymerization

CU - Control unit

CW - Continuous wave

DCTP - Degenerative chain transfer polymerization

DF - Dichroic filter

DMSO - Dimethyl sulfoxide

EDTA - Ethylenediamine tetraacetic acid

EM-CCD - Electron-multiplying charge coupled device

EXP – Beam expander

FCS - Fluorescence correlation spectroscopy

FLIM - Fluorescence lifetime microscopy

GC-MS - Gas chromatography mass spectrometry

GPC - Gel permeation chromatography

HMF - Hydroxymethylfurfural

CI - Crystallinity index

IQSC - Instituto de Química de São Carlos

IR - Infrared

IR - Iris

KULeuven - Katholieke Universiteit Leuven

L - Lens

LPF - Low-pass filter

M - Mirror

MM - Mobile mirror

MSD - Mean square displacement

MW - Molecular weight

NA - Numeric aperture

NADH - Nicotinamide adenine dinucleotide - hydrogen

NCC - Nanocrystalline cellulose

NF - Notch filter

NLC - Non-linear crystal

NMP - Nitroxide-mediated polymerization

NMR - Nuclear magnetic resonance

OB - Objective

OF - Optical fibre

OMRP - Organometallic-mediated radical polymerization

P - Prism

PA - Piezoelectric

PBS - Prism beam splitter

PDI - Polydispersity index

PDI* - Perylene diimide

PEG - Polyethylene glycol

PFD - Pre-focus system

PH - Pinhole

PP - Pulse picker

PRE - Persistent Radical Effect

PVA - Polyvinyl Alcohol

PVP - Polyvinylpyrrolidone

S - Sample

SD - Silicon detector

SEM - Scanning electron microscopy

SPT - Single-particle tracking

STED - Stimulated emission depletion

STEM - Scanning transmission electron microscopy

TEM - Transmission electron microscopy

THF - Tetrahydrofuran

TIRF - Total internal reflection fluorescence

TTL - Transistor-transistor logic

USP - Universidade de São Paulo

UV–Vis - Ultraviolet–visible spectroscopy

WP - Wave plate

WFM - Wide field microscopy

XRD - X-ray diffraction

LIST OF TABLES

Table 1. Decay times (τ_i) and normalized amplitudes (a_i) of micrometre-sized emission spots from cellulose samples isolated from sugarcane bagasse obtained by multiexponential fitting. ⁴⁰	20
Table 2. Decay times and normalized amplitude related to Avicel® and NCC.....	42
Table 3. Diffusion coefficients Dt_1 and Dt_2 of rhodamine 6G, ATTO-532 and NCC....	60
Table 4. Weight Average Molecular Weight (M_w), Number Average Molecular Weight (M_n) and Polydispersity index (PDI), related to the system 1, system 2 and system 3.	87

LIST OF FIGURES

Figure 1. Molecular structure of cellulose. ⁷	3
Figure 2. Structural composition of lignocellulosic biomass based on sugarcane. Adapted from. ¹⁰	4
Figure 3. Confocal microscopy setup. Top picture: Microscope IX71 containing two APD detectors, piezoelectric PI controller. Bottom picture: Maya 2000 Pro spectrometer attached to the microscope (IQSC – USP) ⁴⁰	10
Figure 4. Confocal optical schematic setup. APD: avalanche photodiode; BS: beam splitter; CU: control unit; DF: dichroic filter; EXP: expander beam; IR: iris; L: lense; LPF low-pass filter; M: mirror; MM: mobile mirror; NF: notch filter; NLC: non-linear crystal; OB: objective; OF: optical fibre; PBS: prism beam splitter; PA: piezoelectric; PH: pinhole; PP: pulse picker; S: sample; SD: silicon detector; W: wave plate. (IQSC – USP) ⁴¹	11
Figure 5. Wide field optical schematic. CAA: camera assembly attached; CU: control unit; DF: dichroic filter; EXP: expander beam; IR: iris; M: mirror; MM: mobile mirror; NF: notch filter; OB: objective; P: prism; PFD: pre-focus system; S: sample; W: wave plate (IQSC – USP) ⁴¹	12
Figure 6. SEM images of bagasse samples: a whole bagasse, b fibre, c pith, d BWB, e BF and f BP. Micro sized splinters are indicated by arrows in samples after bleaching process. ⁴³	14
Figure 7. Fluorescence microscopy images of a whole bagasse, b fiber, c pith, d BWB, e BF and f BP. Samples were excited at 405 nm. The lateral colour scale bars are related to the fluorecence intensity. ⁴³	15
Figure 8. Fluorescence intensity image and decay traces of indicated emission spots obtained by two-photon excitation at 800 nm of a) whole bagasse, b) fibre, c) pith, and corresponding bleached samples, d) BWB, e) BF and f) BP. Scale bar 10 nm. ⁴³	17
Figure 9. Two-photon fluorecence microscope images of a whole bagasse sample obtained at a focal plane of a) 0 μ m, b) 5 μ m and c) 10 μ m. Scale bar 10 μ m. The lateral colour scale bars are related to the fluorecence intensity. ⁴³	18

Figure 10. Fluorescence intensity images and decay of each indicated emission spot obtained by two-photon excitation at 800 nm of samples stained with safranin: a) whole bagasse and b) BWB. Scale bar 10 nm. The lateral colour scale bars are related to the fluorescence intensity. ⁴³	22
Figure 11. Fluorescence spectra from (solid curve) fibre, (long dashed curve) fibre/safranin, (two dotted dashed curve) BF, single dotted dashed curve) BF/safranin and (shorted dashed curve) Avicel. Samples were excited at 405 nm and spectral intensity was recorded using a linear CCD spectrometer fibre coupled to the binocular side port of the microscope. ⁴³	24
Figure 12. From the cellulose sources to the cellulose molecules: Details of the cellulosic fiber structure with emphasis on the cellulose micro fibrils. ⁶⁵	29
Figure 13. SEM images of Avicel® samples. Morphologic details of microcellulose particles.....	35
Figure 14. TEM images of nanocrystalline cellulose, obtained from sulphuric acid hydrolysis.	36
Figure 15. Diffratograms of Avicel® and NCC. The values of crystallinity index calculated from method Segal et al were 57% to Avicel® and 70% to NCC.	37
Figure 16. WFM images of Avicel® (a and b) and NCC (c and d).	39
Figure 17. Fluorescence spectra of a) Avicel® and b) NCC obtained by excitation at 405 nm.	40
Figure 18. Fluorescence decays of a) Avicel® and b) NCC obtained by two-photon excitation at 800 nm.	41
Figure 19. Wide field fluorescence images of a) solution of PVA-water/NCC and b) PVP-isopropanol/NCC.	43
Figure 20. Images of NCC obtained via sulphuric acid hydrolysis. a) Confocal: λ_{exc} = 635 nm, power = 28.5 mW, size = 400x400p (10x10mm), dwell time = 0.4 ms and b) STED: λ_{exc} = 750 nm, power = 4.4 mW (20mW), size = 400x400p (10x10mm), dwell time = 0.4 ms.	44

Figure 21. a) Confocal and b) STED microscopy images and the respective profile of the spot pointed from the yellow arrow.....	45
Figure 22. Schematic diagram illustrating the various types of chemical modifications on NCC surface. ³⁵	50
Figure 23. Autocorrelation curves of rhodamine 6G, ATTO-532 and NCC/ATTO-532.	59
Figure 24. Prolate particle shape, in which b is the semi-minor axis of the structural unit and a is the semi-major axis of the structural unit.....	60
Figure 25. Autocorrelation curves of a) NCC/PEG/water, b) NCC/PEG/methanol and c) NCC/PEG/acetonitrile at the PEG concentration of 2%, 5%, 10% and 20%.....	63
Figure 26. a) NCC fraction and diffusion coefficient (Dt) in function of PEG content. b) ATTO-532 fraction and diffusion coefficient (Dt) in function of PEG content.....	65
Figure 27. Step-length distribution for a) NCC/PEG (50%)/water; b) NCC/PEG (70%)/water; c) NCC/PEG (50%)/methanol; d) NCC/PEG (70%)/methanol; e) NCC/PEG (50%)/acetonitrile and f) NCC/PEG (70%)/acetonitrile. Single particle trajectories in a representative area are shown in the insets.....	66
Figure 28. Mean square displacement (MSD) for a) NCC/PEG/water; b) NCC/PEG/methanol and c) NCC/PEG/acetonitrile.	68
Figure 29. Diffusion coefficient of NCC as a function of PEG content (%).....	70
Figure 30. General concept of controlled/living radical polymerization (CRP). ¹⁶²	75
Figure 32. Activation–deactivation equilibrium in nitroxide-mediated polymerization. Bicomponent initiating system (a) and monocomponent initiating system (b). ¹⁶²	76
Figure 32. Structures of styrene (1) and of the alkoxyamine-based NMP initiators used in this work (2 and 5: non-fluorescent initiators; 3 and 4: fluorescent initiators).	77
Figure 33. Sample holder device.	79
Figure 34. Schematic setup of the FCS and WFM (KU Leuven).	82
Figure 35. Raman spectra for the polymerization of styrene, mediated by a) System 1, b) System 2 and c) System 3.....	84

Figure 36. GPC traces of the polystyrene obtained via NMP for the a) System 1, b) System 2 and c) System 3.....	86
Figure 37. Normalized FCS autocorrelation curves for the polymerization of styrene, mediated by a) System 1, b) System 2 and c) System 3 at different reaction time.	88
Figure 38. a) Monomer conversion in function of polymerization time. B) Diffusion coefficients plotted versus styrene conversion. Square symbols represent diffusion coefficients related to polymerization mediated by linear initiator (system 1), round symbols represent diffusion coefficients related to polymerization mediated by linear initiator, containing fluorescent star-shaped initiator (system 3), and triangle symbols represent diffusion coefficients related to polymerization mediated by star-shaped initiator system 2).	90
Figure 39. Step-length distribution for a) system 1, b) system 2 and c) system 3. The distributions exhibited are related to polymeric systems after 180 minutes of reaction. Single molecule trajectories in a representative area are shown in the insets.	92
Figure 40. Mean square displacement (MSD) for system 1 (a), system 2 (b) and for system 3 (c). Below of MSD graphs is shown the schematic representation of labelled chain in their surroundings of respective system. Yellow circles shown in some chains represent th the labelling by perylene diimide (PDI*).	94

SUMMARY

ACKNOWLEDGMENTS	i
PREFACE	ii
ABSTRACT	iii
RESUMO	v
LIST OF ABBREVIATIONS	vii
LIST OF TABLES	xi
LIST OF FIGURES	xii
CHAPTER 1: OPTICAL MICROSCOPY STUDY OF SUGARCANE BAGASSE	
ABSTRACT	2
1 INTRODUCTION	3
2 EXPERIMENTAL	7
2.1 Preparation of sugarcane bagasse samples	7
2.2 Labelling of sugarcane bagasse by safranin.....	7
2.3 Techniques	8
2.3.1 Scanning electron microscopy	8
2.3.2 Fluorescence confocal microscopy	8
2.3.3 Wide field microscopy	11
3 RESULTS AND DISCUSSION	13
3.1 Characterization of sugarcane bagasse by autofluorescence microscopy.....	13
4 CONCLUSIONS	25

CHAPTER 2: PRODUCTION AND OPTICAL MICROSCOPY CHARACTERIZATION OF NANOCRYSTALLINE CELLULOSE

ABSTRACT	27
1 INTRODUCTION	28
2 EXPERIMENTAL	32
2.1 Production of nanocrystalline cellulose by acid hydrolysis.....	32
2.2 Preparation of nanocrystalline/polymer composites	32
2.3 Techniques	32
2.3.1 X-ray diffraction.....	32
2.3.2 Transmission electron microscopy.....	33
2.3.3 Scanning electron microscopy	33
2.3.4 Confocal fluorescence microscopy	33
2.3.5 Wide field microscopy	34
2.3.6 Super-resolution microscopy by Stimulated emission depletion (STED)	34
3.1 Characterization of Avicel® NCC by electron microscopy and X-ray diffraction	35
3.2 Characterization of Avicel® NCC by wide field microscopy	38
3.3 Characterization of Avicel® NCC by steady and time-resolved fluorescence spectroscopy.....	39
3.4 Dispersion of NCC in polymers.....	42
3.5 Super-resolution optical microscopy of Avicel® and NCC	43
4 CONCLUSIONS.....	46
 CHAPTER 3: FLUORESCENT LABELLING OF NANOCRYSTALLINE CELLULOSE	
ABSTRACT	48

1 INTRODUCTION	49
2 EXPERIMENTAL	52
2.1 Obtaining NCC	52
2.2 Preparation of 1-azide-2,3-epoxypropane.....	52
2.3 Introducing azide groups to the surface of NCC	53
2.4 Labeling of azide functionalized NCC with ATTO-532 dye.....	53
2.5 FCS measurements	53
2.6 Wide Field Measurements	56
3 RESULTS AND DISCUSSION.....	58
3.1 Determination of diffusion coefficient of NCC dispersions	58
3.2 Study of dynamic properties of different composites based on the interaction of NCC/polymer.....	60
4 CONCLUSIONS.....	71

CHAPTER 4: POLYMERIZATION OF STYRENE

ABSTRACT	73
1 INTRODUCTION	74
2 EXPERIMENTAL	77
2.1 Polymerization of styrene	77
2.2 Polymerization process	78
2.3 Measurements	80
2.3.1 GPC.....	80
2.3.2 Raman	80
2.3.3 FCS	81
2.3.4 WFM.....	81

3 RESULTS AND DISCUSSION	83
3.1 Styrene nitroxide mediated polymerization	83
4 CONCLUSIONS.....	95
REFERENCES	96

CHAPTER 1

OPTICAL MICROSCOPY STUDY OF SUGARCANE BAGASSE

ABSTRACT

The spatial distribution of the components in the sugarcane bagasse is a very important issue related to its industrial application, including the production of second generation ethanol. In addition, several cellulosic materials have been used to produce diverse polymeric composites. Sugarcane bagasse samples including whole bagasse, fibre, pith, and respective samples obtained after chemical bleaching were investigated using confocal fluorescence microscopy and spectroscopy with one and two-photon excitation. Images from unbleached samples showed longitudinally oriented emission patterns in fibre walls containing lignin fraction. After bleaching treatment, the oriented emission was partially disrupted. Autofluorescence from bleached samples, with a residual lignin content of about 1%, was attributed to the presence of fluorophores dispersed throughout the matrix, which induced the concomitant reduction of fluorescence self-quenching. The combination of autofluorescence images with spectral emission and lifetime measurements provides a tool for microscopic characterization of natural bagasse samples. Moreover, the technique allows the monitoring of bleaching processes related to the lignin removal.

1 INTRODUCTION

Lignocellulosic compounds are widely used as source of different fermentable sugars, showing a great potential in production of ethanol of second generation and production of biomaterials.¹⁻³ Lignocellulose may be found in plant tissues, wherein the major composites are cellulose, polyoses and lignin. Polyoses are branched polysaccharides, consisting of pentose, hexose and uric acid.⁴ Lignin is an aromatic biopolymer, which is synthesized from the phenylpropanoid pathway. Figure 1 shows the chemical structure of the cellulose, a linear biopolymer with high molecular weight, containing units of 1,4 D-glucose, and crystalline and amorphous regions.^{5;6}

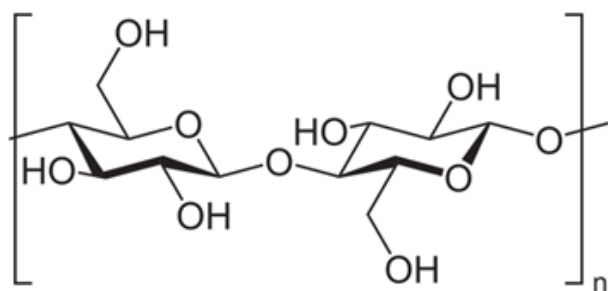


Figure 1. Molecular structure of cellulose.⁷

The reduction of emission of global warming gases provides a growing demand on production of fuel obtained from renewable source. In this scenario, there is the increasing necessity to produce biofuels.^{8;9} In order to attend to the green production claim it is necessary the development of new technologies related to the depolymerization of lignocellulose materials. Sugarcane bagasse is a by-material that has been used in sugarcane plant boilers to generate vapour and electricity. Figure 2 shows the schematic illustration of a typical lignocellulosic biomass based on sugarcane.

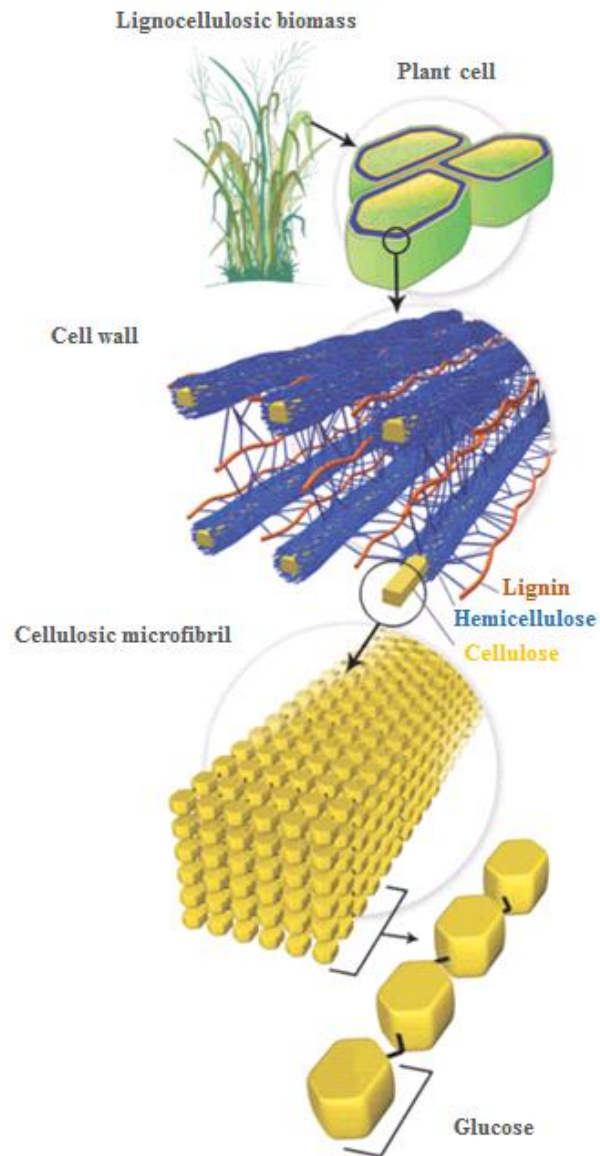


Figure 2. Structural composition of lignocellulosic biomass based on sugarcane. Adapted from.¹⁰

Bagasse is a residue obtained from the processing of sugarcane. This product has a substantial chemical and morphological heterogeneity. The two main parts of bagasse are fibre bundles and pith. The last one is composed by structural elements similar to vessels, parenchyma and epithelial cells. Sugarcane is a raw-material that has a great potential as cellulose source. In general, the process that produce second generation

ethanol is initiated by hydrolysis of the cellulose forming glucose.¹¹ Several methodologies, including fluorescence based methods, may be used in characterization of compounds in plant cell walls.¹²⁻¹⁵ Optical microscopy represents an important technique to identify and localize the presence of lignocellulosic compounds, besides, it has the advantage of being a non-invasive and non-destructive method. In this scenario, two-photon microscopy has been used successfully to study lignocellulosic materials, because of its high spatial resolution and improved signal collection efficiency that gives images with higher contrast and better quality. Due to its larger penetration depth, it is possible to obtain images from thick sections. Images can be recorded several times deeper than by single-photon microscopy. Fluorophore compounds that are active at single-photon excitation can often be excited by two photons of twice the wavelength (2λ). However, one must recognize that single-photon and two-photon excitation show different quantum-mechanical processes and have very different selection rules.¹⁶⁻²⁰

Plant tissues are complex biomaterials with intrinsic fluorescence properties. The distribution of lignin in cellulosic matrices is an important parameter to evaluate the quality of cellulosic material for ethanol production. Safranin has been used as a probe in studies of plant tissues and cellulosic fibres^{13; 21-23} because of the preferential interaction of the dye with the region containing lignin. Fluorescence lifetime microscopy (FLIM) is a technique that has been used by some authors to identify and quantify lignin in sugarcane bagasse.¹⁵ In the investigation of the autofluorescence from plant biomaterials, some authors have attributed the observed emission to the presence of lignin fractions and aromatic compounds as lignans, flavonoids and tannins.²⁴⁻²⁶ On the other hand, the autofluorescence has also been ascribed to the presence of flavins and flavoproteins.²⁷ Until the present time, there is still no consensus about the presence of autofluorescence signal after chemical bleaching processes, which

should eliminate almost all primary compounds responsible by the natural emission of lignocellulose materials.

Different studies have shown the capacity of fluorescence microscopy techniques to reveal information about the spatial distribution and concentrations of components in lignocellulosic matrices.²⁸⁻³⁰ Confocal and wide field fluorescence microscopy in combination with spectroscopy techniques are useful tools in the study of structure and composition of plant materials.

The hydrolysis of micro cellulose that uses concentrated inorganic acids as sulphuric and hydrochloric is a well-established methodology used to convert cellulose into sugars and to generate nanocrystalline cellulose. The structural properties combined with chemical and physical composition represent the most important features of fibres in application as, for example, reinforcement additives to the production of polymeric composites.^{1; 31} The use of nanocrystalline cellulose to reinforce composites require strong adherence between the fibre and the polymeric solution. Moreover, it is necessary a high degree of dispersion of fibre into that material.³² The structure of the fibre may be modified by different treatments, depending on the required aim and application. Samir *et al* showed that the presence of nanocrystalline cellulose in polymeric composites induces the phenomenon of percolation, which contributes to the improvement of thermal, mechanical, and barrier properties.³³⁻³⁵ One of the major difficulties related to the use of nanocrystalline cellulose in composites is associated to its dispersion into the polymeric solution without degradation or formation of self-aggregated phases. To overcome such obstacles, several studies have been developed aiming at the increase of compatibility between the polymeric matrix with the nanocrystalline cellulose.³⁶⁻³⁸

2 EXPERIMENTAL

2.1 Preparation of sugarcane bagasse samples

The process of preparation of different sugarcane bagasse samples were performed by Karen Marabezi from the laboratory of Organic Physical-Chemistry (University of São Paulo – São Carlos/SP), coordinated by the Professor Antonio Aprigio da Silva Curvelo. All the samples were washed with water aiming to eliminate interstitial impurities. The process of separation of bagasse fractions were carried out by the use of sieves with diameter mesh of 16–60. The remain compounds were removed by extraction using the solvent mixture cyclohexane/ethanol (1:1, v/v) and water.

The methodology of removal of lignin was performed according to known delignification oxidative process.³⁹ Before the process, the sugarcane sample was separated into three groups: integral bagasse, fiber and pith. The crystallinity of sugarcane bagasse was determined by X-ray diffraction and showed the value of 0.55 g/g.

2.2 Labelling of sugarcane bagasse by safranine

The samples of integral bagasse and bleaching integral bagasse (5g) were labelled by the use of aqueous solution of safranine ($3 \cdot 10^{-5} \text{ mol.L}^{-1}$). The bagasse remained immerse in solution under stirring for 5 minutes. Afterwards the sample was washed 3 times for 10 minutes using distilled water in temperature of 40°C.

2.3 Techniques

2.3.1 Scanning electron microscopy

The samples were deposited in specific aluminium supports. The measurements were performed in the Instrumental Analysis Centre of the Institute of Chemistry of São Carlos (CAQUI/IQSC/USP) using a Zeiss Leo 440 scanning microscopy with Oxford detector, operating with an electron beam of 20 kV. The sample were covered by 10 nm of gold in a metallizer device BAL-TEC (model MED 020) and kept in desiccator.

2.3.2 Fluorescence confocal microscopy

All the samples used were suspended in water and spin-coated (~3000 rpm, 30 s) on cover glasses (0.13 mm, 22 x 22 mm, VWR International). The cover glasses were cleaned by rinsing Milli-Q water, drying with argon gas and overnighting in a muffle at 450 °C.

The confocal microscopy setup was “lab built” in Molecular Fluorescence Laboratory at IQSC - USP, containing an inverted microscope IX71-Olympus, with a nanometric scanning controlled by piezoelectric device (E-710.3CD – PI). The system was used to achieve data related to confocal fluorescence images, steady-state emission and fluorescence decays.

The confocal microscopy and steady-state emission measurements of sugarcane bagasse and Avicel® samples were performed by using a CW laser excitation at 405 nm using a Cube Coherent diode laser operating with adjustable output power from 1 – 40 mW. The measurements of safranin labelled lignocellulosic material were carried out by excitation with a Verdi-Coherent laser at 532 nm, operating at low intensity (20 mW). In both setup features were applied circularly polarized light, generated from $\frac{1}{4}$ wave

plates of zero order (Del Mar Photonics). Two Olympus objectives lenses were used, 40X, NA = 0.75 model UPLFLN 40XPH and 60X, NA = 1.35 model UPLSAPO 60XO. The detection system used a photon counting detector APD type, Perkin Elmer, model SPCM-AQRH.

Confocal images were obtained due to the controlling and synchronizing of the piezoelectric scanning system and two plates of National Instruments (PCI-GPIB NI-488.2 e PCI-6601) applied to acquisition of TTL signal. Communication and interfacing of the instruments were achieved by two programs developed in our laboratory, written in LabView 8.5, and in the Laboratory for Photochemistry and Spectroscopy from KU Leuven, written in C#.

Steady-state emission fluorescence spectra were obtained by the spectrometer Maya 2000 Pro – (Ocean Optics), fibre optical attached to IX71 microscope through a side port, which is showed in Figure 3.

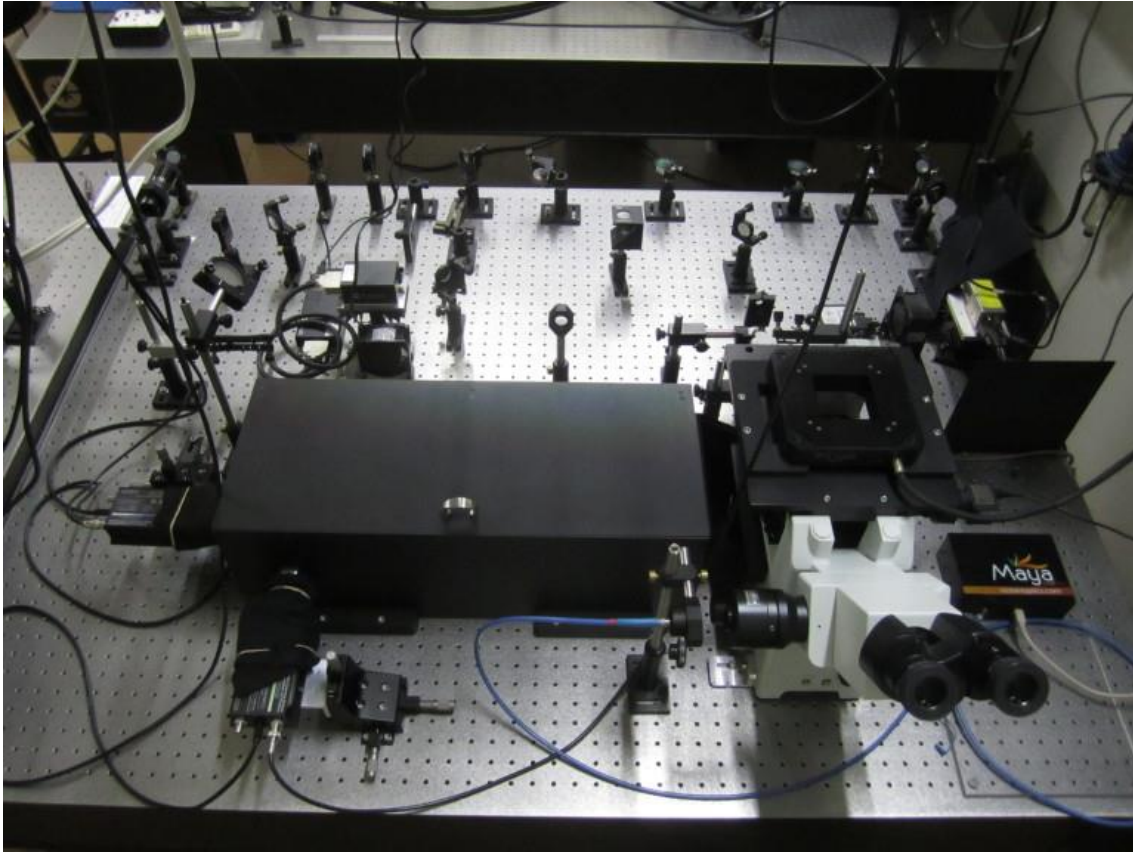


Figure 3. Confocal microscopy setup. Top picture: Microscope IX71 containing two APD detectors, piezoelectric PI controller. Bottom picture: Maya 2000 Pro spectrometer attached to the microscope (IQSC – USP).⁴⁰

A pulsed laser beam (Ti:Safira Mira 900 – Coherent) at 400 nm with pulse width of 150 fs and frequency of 76 MHz was applied to perform fluorescence decay measurements. Pulse picker (Conoptics) kept excitation pulse frequencies in 4 MHz. Photodiode model TDA 200- PicoQuant with Becker & Hickl 140 was used to counting and synchronizing of photons. Figure 4 shows the schematic setup related to decay measurements.

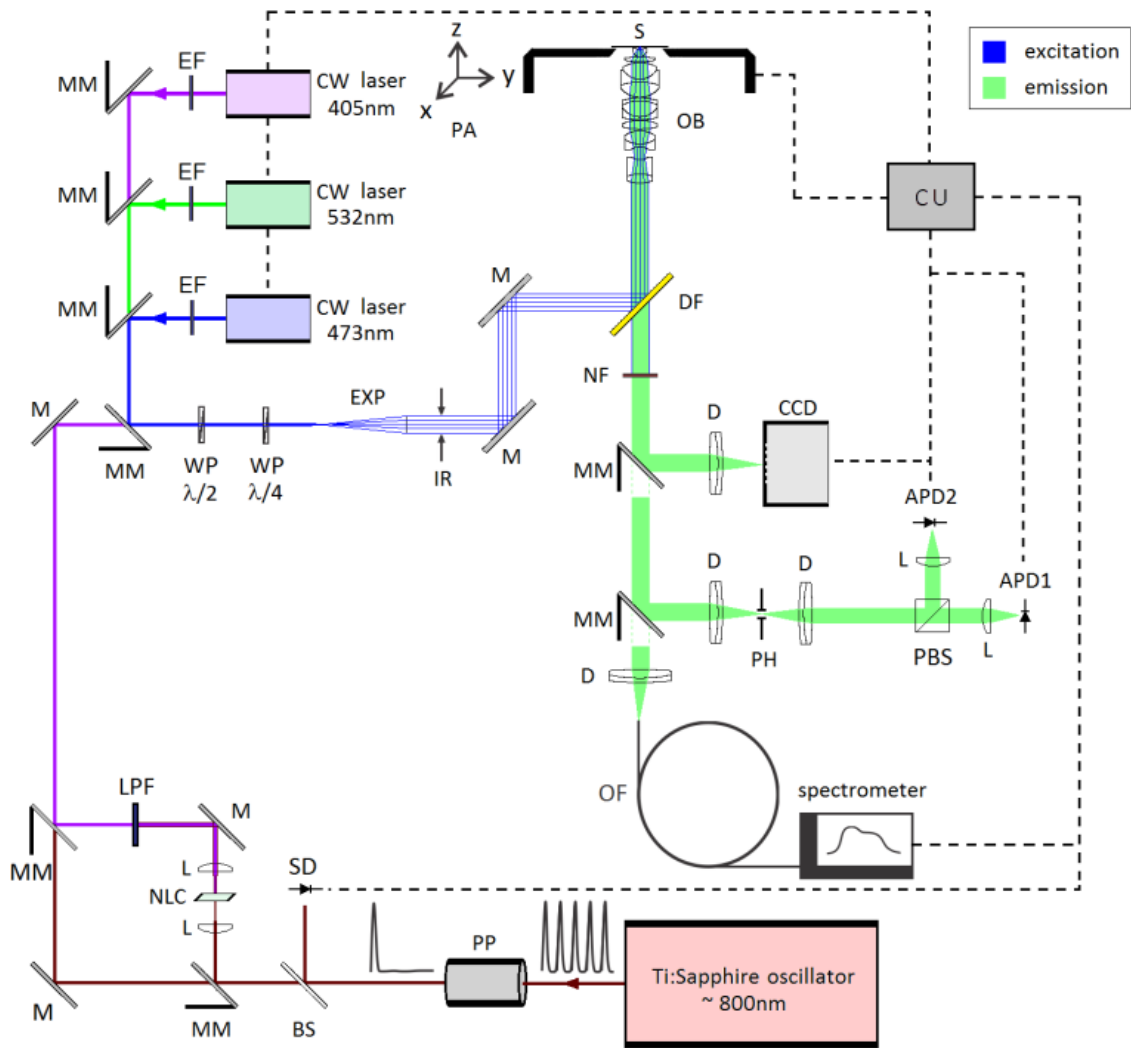


Figure 4. Confocal optical schematic setup. APD: avalanche photodiode; BS: beam splitter; CU: control unit; DF: dichroic filter; EXP: expander beam; IR: iris; L: lens; LPF low-pass filter; M: mirror; MM: mobile mirror; NF: notch filter; NLC: non-linear crystal; OB: objective; OF: optical fibre; PBS: prism beam splitter; PA: piezoelectric; PH: pinhole; PP: pulse picker; S: sample; SD: silicon detector; W: wave plate. (IQSC – USP).⁴¹

2.3.3 Wide field microscopy

The fluorescence wide field images were obtained by using an inverted IX71 Olympus microscope and an objective model UPlanFLN Olympus, with magnification of 100X and numerical aperture of 1.3 in oil. The images were recorded on EMCCD Evolve 512

– Photometrics, coupled to a side output of microscope. The laser sources were Verdi at 532 nm and Cobolt Blues at 473 nm with average power of 50 mW. The schematic setup is illustrated in Figure 5.

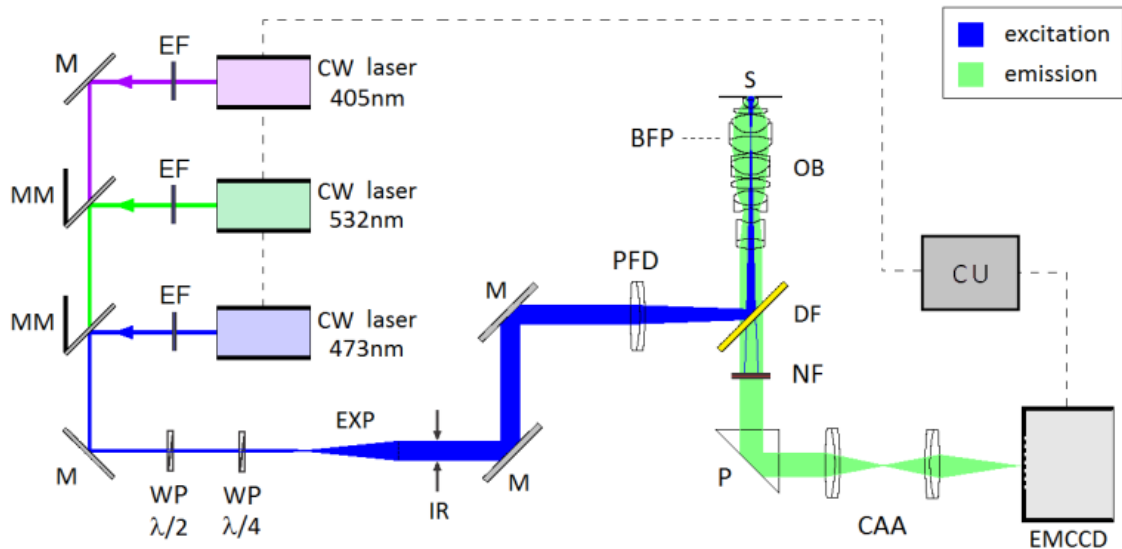


Figure 5. Wide field optical schematic. CAA: camera assembly attached; CU: control unit; DF: dichroic filter; EXP: expander beam; IR: iris; M: mirror; MM: mobile mirror; NF: notch filter; OB: objective; P: prism; PFD: pre-focus system; S: sample; W: wave plate (IQSC – USP).⁴¹

3 RESULTS AND DISCUSSION

3.1 Characterization of sugarcane bagasse by autofluorescence microscopy

SEM analysis of sugarcane bagasse samples (whole bagasse, fibre and pith), and the corresponding bleached samples (bleached whole bagasse (BWB), bleached fibre (BF) and bleached pith (BP)) were used to determine the effect of chemical bleaching. These regions were analysed because they present unique characteristics with respect to their recalcitrance and morphology. Integral bagasse basically consists of fibre and pith. The fibre surface is formed by parallel stripes and has a high length/diameter ratio. In contrast, pith has a fragile and fragmented structure associated to parenchyma cells designed to store sucrose. These features are very important to the understanding of hydrolysis and bleaching processes. In Figure 6 SEM micrographs of unbleached and bleached samples are compared. Unbleached samples (Fig. 6 a, b, c) present a rigid and compact morphology. After chemical bleaching, fibre and pith exhibited disorganized morphology. The roughness and some micro sized splinters were observed on the surfaces (Fig. 6 d, e, f). Therefore, after bleaching, samples showed most exposed structure, which allows more accessibility hydrolysis reaction of lignocellulosic biomass.⁴²

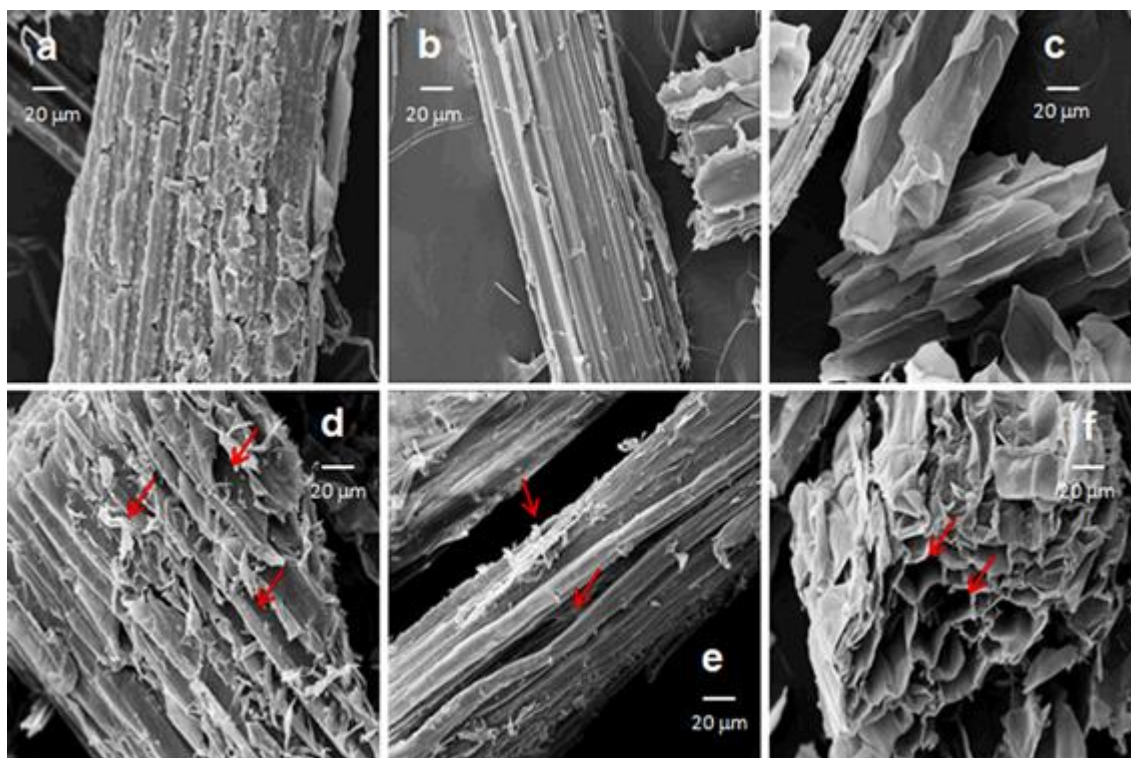


Figure 6. SEM images of bagasse samples: a whole bagasse, b fibre, c pith, d BWB, e BF and f BP. Micro sized splinters are indicated by arrows in samples after bleaching process.⁴³

Autofluorescence images of bleached and unbleached sugarcane bagasse samples were performed to improve the understanding of morphological microenvironment in cellulose matrix and to evaluate distribution of lignin fraction before and after the treatment. Confocal fluorescence images, obtained by single-photon excitation at 405 nm, of whole bagasse, pith and fibre samples, and the corresponding bleached ones BWB, BF and BP, are compared in Figure 7. The material absorbs light in a wide spectral range, from the near ultraviolet to the visible, due to their complexity and micro environmental diversity. However, the samples showed higher emission intensity when excited at 405 nm region. All samples exhibited quite strong autofluorescence without fine structure. In other words, it is not possible to show the individual dots related to the structure. Therefore, well oriented straight row tracks structures formed by the

longitudinal organization of fibres do not appear in any region observed in both natural and bleached samples. Autofluorescence arises from compounds dispersed in the plant cell walls⁴⁴ mostly from the lignin fraction. Features related to structure and thickness affect resolution and contrast of fluorescence images. In addition, the excitation light at UV–Vis region cause light scattering in the samples, and conventional confocal microscopy study of plant tissues may be limited by the opacity of the medium.^{45; 46} This problem can be overcome by using two-photon microscopy, because scattering and absorption are substantially reduced in the near-infrared range compared to the visible range.^{18; 47}

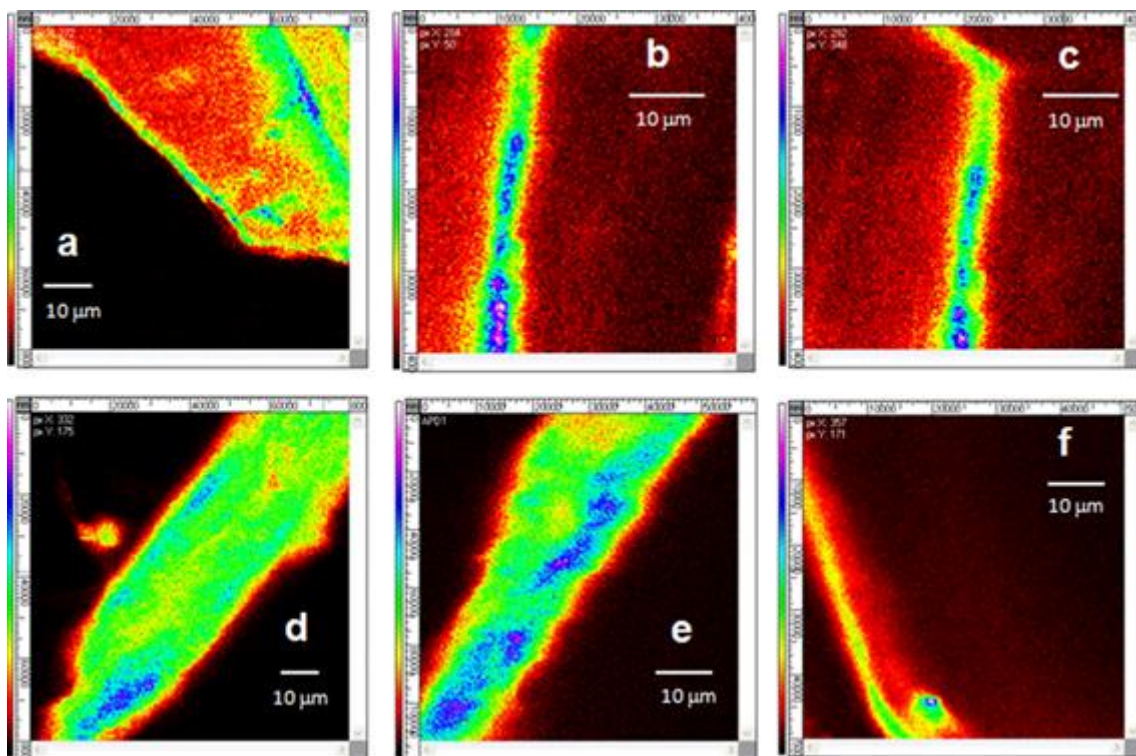


Figure 7. Fluorescence microscopy images of a whole bagasse, b fiber, c pith, d BWB, e BF and f BP. Samples were excited at 405 nm. The lateral colour scale bars are related to the fluorescence intensity.⁴³

Images of sugarcane cellulose materials measured by two-photon microscopy are illustrated in Figure 8. The images show greater structural details compared to images obtained using confocal microscopy via single-photon excitation. In addition, images generated from two-photon excitation contained some microstructure information and more detailed fluorescence mapping than single-photon excitation images. Two-photon microscopy offers supplementary characterization of lignocellulosic materials,^{45; 48} because transitions between states of the same parity are forbidden for single-photon excitation, but they are allowed for the two-photon excitation.¹⁶ The fluorescence images in Figure 8 show sequences of small fluorescent spots that form well oriented straight row tracks, which are related to lignin fraction, especially from unbleached whole bagasse and fibre samples. The spots indicated were used to accumulate the fluorescence decay of each sample. The average distance between two oriented fluorescence tracks is about 12 μm , which is comparable with the distance between cell walls determined by SEM (see Figure 6b). Fluorescence spots in pith samples show a decrease in intensity and disordered structure, it does not generate straight tracks format. Bleached samples do not contain emission tracks; instead, some blurry emission spots are evident. This result is consistent with disorder increasing in the samples after chemical bleaching because of dispersion of crystalline cellulose domains.

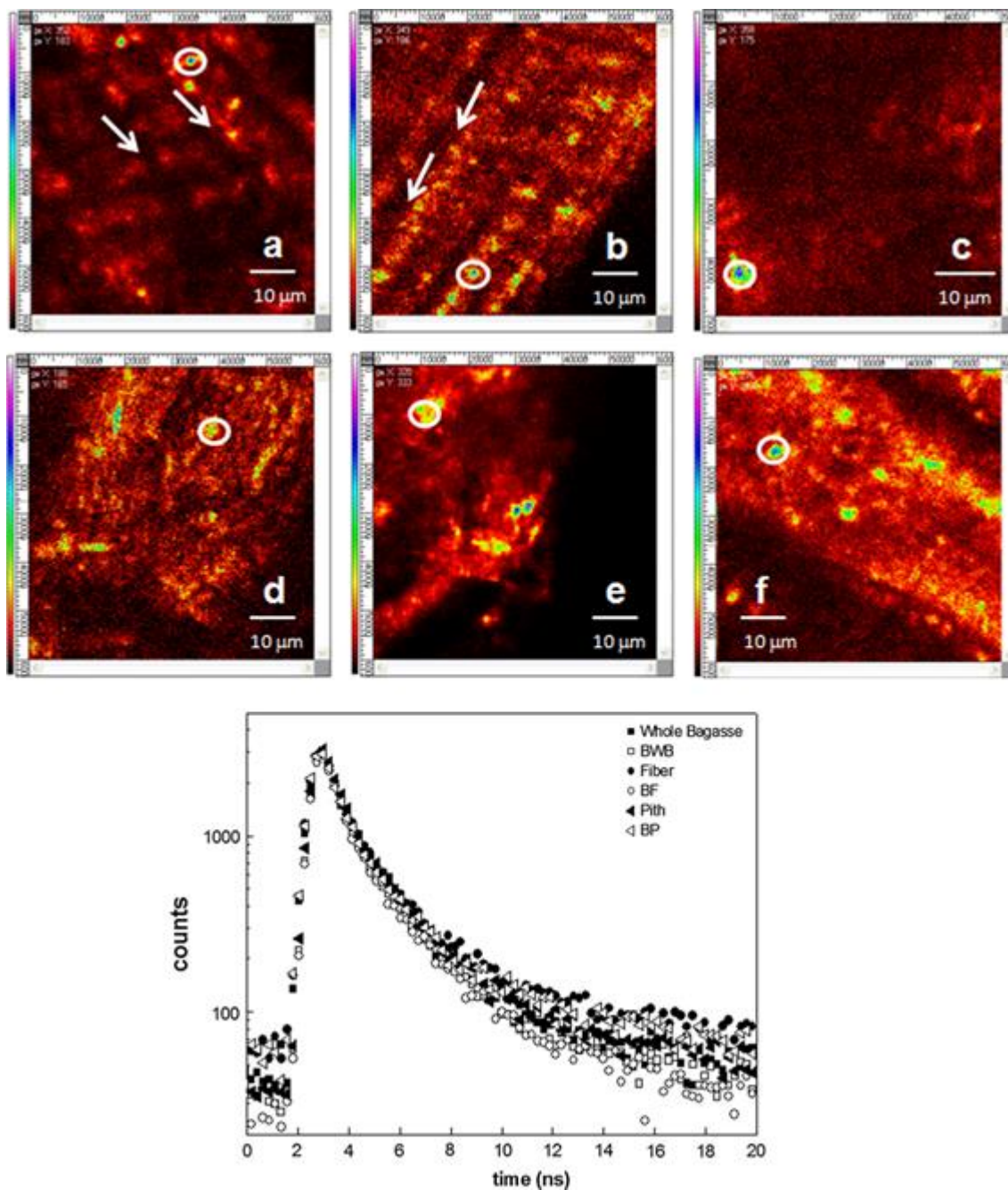


Figure 8. Fluorescence intensity image and decay traces of indicated emission spots obtained by two-photon excitation at 800 nm of a) whole bagasse, b) fibre, c) pith, and corresponding bleached samples, d) BWB, e) BF and f) BP. Scale bar 10 nm.⁴³

Scanning the z-position of the focal plane using two-photon fluorescence microscopy allowed us to visualize the architecture, fibril patterns, and other details of the microstructure of cellulosic materials. 2D images at various depths of z-axis from 0 to 10 μm are shown in Figure 9. Orientation of micrometre-sized emission tracks is

thoroughly dependent of z-position. Each micrometre change in depth of the focal plane leads to loss of orientation. This effect may be related to the SEM images of the bagasse sample in Figure 6a, where oriented walls of the fibre are located near its surface.

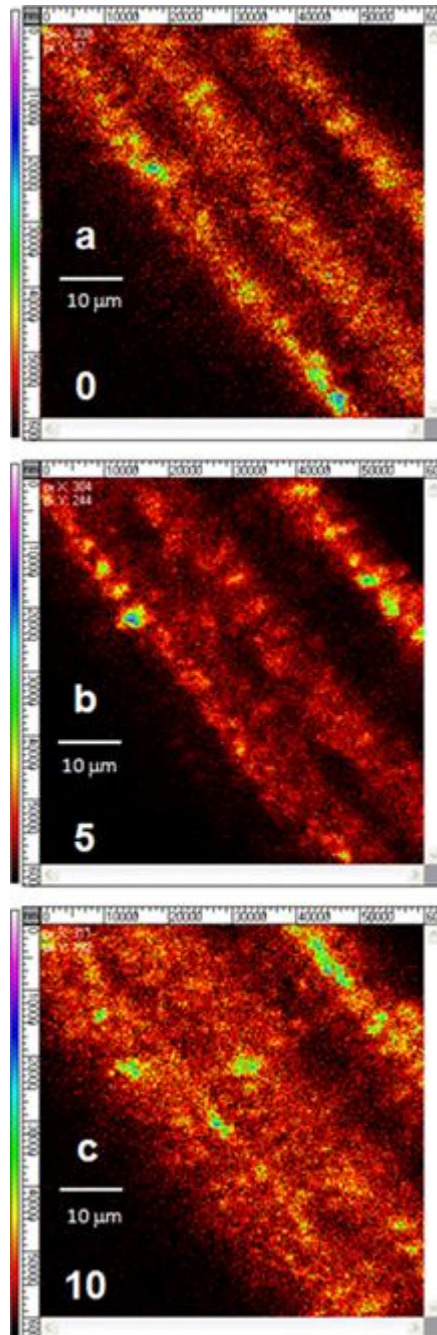


Figure 9. Two-photon fluorescence microscope images of a whole bagasse sample obtained at a focal plane of a) 0 μm , b) 5 μm and c) 10 μm . Scale bar 10 μm . The lateral colour scale bars are related to the fluorescence intensity.⁴³

Lifetime measurements in combination with microscopy techniques can be used to study biological materials.^{49; 50} Samples were investigated by fluorescence decay measurements aiming at the investigation of lignin-rich regions. Fluorescence decay traces were recorded at wavelength of 500 nm, as well as at 575 nm for samples labelled with safranine, which corresponds to emission maximum of the dye. Decay analyses were performed by FAST software (Edinburgh Instruments), fitted by multiexponential function without deconvolution. The fitting range was chosen by considering the decay part of the time dependent data according to optimal parameters. Typical decay profiles of untreated and bleached samples are illustrated in Figure 8. The fluorescence relaxation was fitted with a biexponential decay function. The decay components, normalized amplitudes and average values are presented in Table 1. A fast decay component occurs in the range of 0.4–1.4 ns, and a long-lived component takes more than 2.0 ns to decay. Such biexponential decay behaviour with a short decay component of about 0.4 ns was first observed in the fluorescence emission of *Abies* wood.⁵¹

Table 1. Decay times (τ_i) and normalized amplitudes (a_i) of micrometre-sized emission spots from cellulose samples isolated from sugarcane bagasse obtained by multiexponential fitting.⁴³

Sample	τ_1 (ns)	τ_2 (ns)	τ_3 (ns)	a_1	a_2	a_3	$\langle\tau\rangle$	χ^2
Whole bagasse (500 nm)	0.4	1.9		0.43	0.57		1.7	1.15
Whole bagasse/safranine (500 nm)	0.8	2.8		0.71	0.29		2.0	1.20
Whole bagasse/safranine (575 nm)	0.4	1.3	4.8	0.73	0.23	0.04	2.0	1.05
BWB (500 nm)	0.9	3.1		0.58	0.42		2.5	1.03
BWB/safranine (500 nm)	0.8	3.3		0.56	0.44		2.7	1.13
BWB/safranine (575 nm)	1.1	2.8		0.44	0.56		2.2	1.00
Fiber (500 nm)	0.7	2.4		0.63	0.37		1.6	1.18
Pith (500 nm)	0.7	2.2		0.61	0.39		1.7	1.16
BF (500 nm)	0.9	3.4		0.60	0.40		2.7	1.12
BP(500 nm)	0.7	2.7		0.39	0.61		2.4	1.05

$\langle\tau\rangle$ = Amplitude-weighted average decay time

Complex matrices such as sugarcane bagasse contain multiple intrinsic fluorophores, which may be aromatic compounds with phenolic and acid groups from the lignin fraction (cinnamic residues), and traces of endogenous biomolecules such as enzymes and cofactors, chlorophyll, xanthophylls, coumarin and flavonoid derivatives.^{26; 52; 53;}
⁵⁴Hafren and Oosterveld-Hut⁵⁵ studied wood fibers using fluorescence lifetime imaging. Biexponential fitting at two emission regions of 436 and 480 nm resulted in wavelength-independent decay times of about 0.7 and 4.3 ns. These values are within the range of decay times observed for our samples.

Analysis of decay parameters in this system is a difficult task because of its complexity. Nevertheless, some important issues were identified. In general, the fluorescence decay of untreated and bleached samples are biexponential and occurs in time intervals longer than 20 ns, as illustrated in Figure 8. The calculated average decay time increases by about 68% from fibre to BF, 47% from whole bagasse to BWB, and 41% from pith to BP (see Table 1).

Samples stained with safranin show slightly different decay behaviour, as illustrated in Figure 10. First, unbleached samples like whole bagasse show a third decay component with a lifetime of 4.8 ns. This component is ascribed to the decay of the singlet-excited state of safranin formed mainly through energy transfer from the natural compounds to the added dye. In addition, the fluorescence lifetime of safranin in other solvents was also measured. In a polyvinylpyrrolidone film, a single component with a lifetime of about 4 ns was recorded, while the fluorescence lifetime of safranin in propanol was 3 ns. Therefore, the observed increase of safranin fluorescence lifetime in bagasse samples is a result of absorption of the dye in lignin-rich regions. The second difference is the moderate quenching of the second decay component of the whole bagasse sample, which is reduced from 1.9 to 1.3 ns. This result is consistent to fluorescence quenching of excited chromophores of the lignin fraction by energy transfer to the adsorbed safranin. Fluorescence behaviour is thoroughly linked to the chemical environment of the cellulosic matrix.⁵⁶ Chemical bleaching of lignin fraction causes decomposition and dispersion of the components generated. The bleaching reaction also decreases the amount of organic materials and intrinsic fluorophores in the sample. Therefore, bleaching reduces energy migration and fluorescence self-quenching in the samples. Self-quenching is mainly observed when the lignin matrix is intact and its intrinsic fluorophores are closely confined. The emission intensity of the bleached samples is still strong because most of the remaining chromophores are partially isolated or dispersed in the cellulosic matrix, reducing excited state deactivation by self-quenching. These results are in agreement with those obtained by using fluorescence lifetime imaging (FLIM) to map the distribution of lignin in sugarcane bagasse.¹⁵ They also obtained two components related to fluorescence decay, one with the fast and another

with the slow decay time. The faster decay is associated to dense lignin regions and becomes slower after samples undergo pre-treatment to remove lignin.

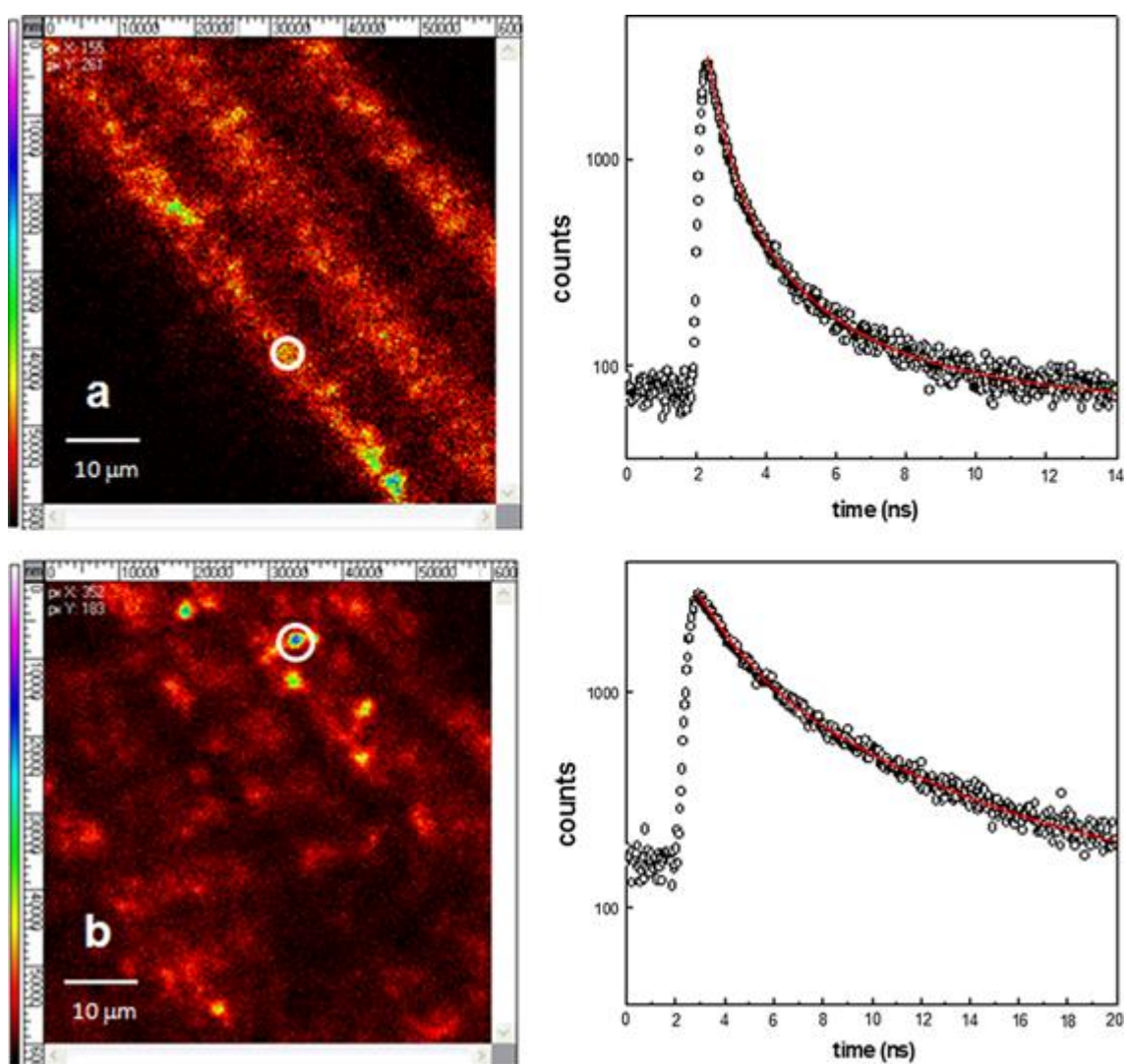


Figure 10. Fluorescence intensity images and decay of each indicated emission spot obtained by two-photon excitation at 800 nm of samples stained with safranin: a) whole bagasse and b) BWW. Scale bar 10 nm. The lateral colour scale bars are related to the fluorescence intensity.⁴³

Emission spectra of the fibre samples were also measured under the same conditions and the results are exhibited in Figure 11. Untreated fibre presented high intensity emission with a maximum at about 500 nm, consistent with the emission spectra reported for wood samples.⁵⁷ When safranin was added to the fibre sample, the

emission was quenched and a new band appeared at about 575 nm corresponding to the fluorescence of the added dye. Safranin has negligible absorption at the excitation wavelength of 405 nm, so dye emission may occur after energy transfer from the intrinsic fluorophores to safranin. The BF sample exhibited a similar emission profile to that of the untreated fibre, but its intensity was reduced by half. The reduction in intensity confirms that chemical bleaching removed the lignin fraction, so autofluorescence from the sample decreased. However, the intensity is much higher than would be expected from a sample containing a lignin fraction of about 1% after chemical bleaching. This means that there are still intrinsic fluorophores remaining in some regions of the sample, and these fluorophores showed higher emission efficiency than in the unbleached sample, because of the matrix dispersion and the lower self-quenching process. Chemical treatment cleaves the lignin macrostructure into smaller components, which then disperse all over the solid matrix, reducing the self-quenching. For the BF sample stained with safranin, the dye emission still appears, but at lower intensity, which agrees with energy transfer occurring from the fluorophores remaining in the sample to the added safranin dye. The reference Avicel sample exhibited very weak emission under the same conditions compared with that from bagasse samples.

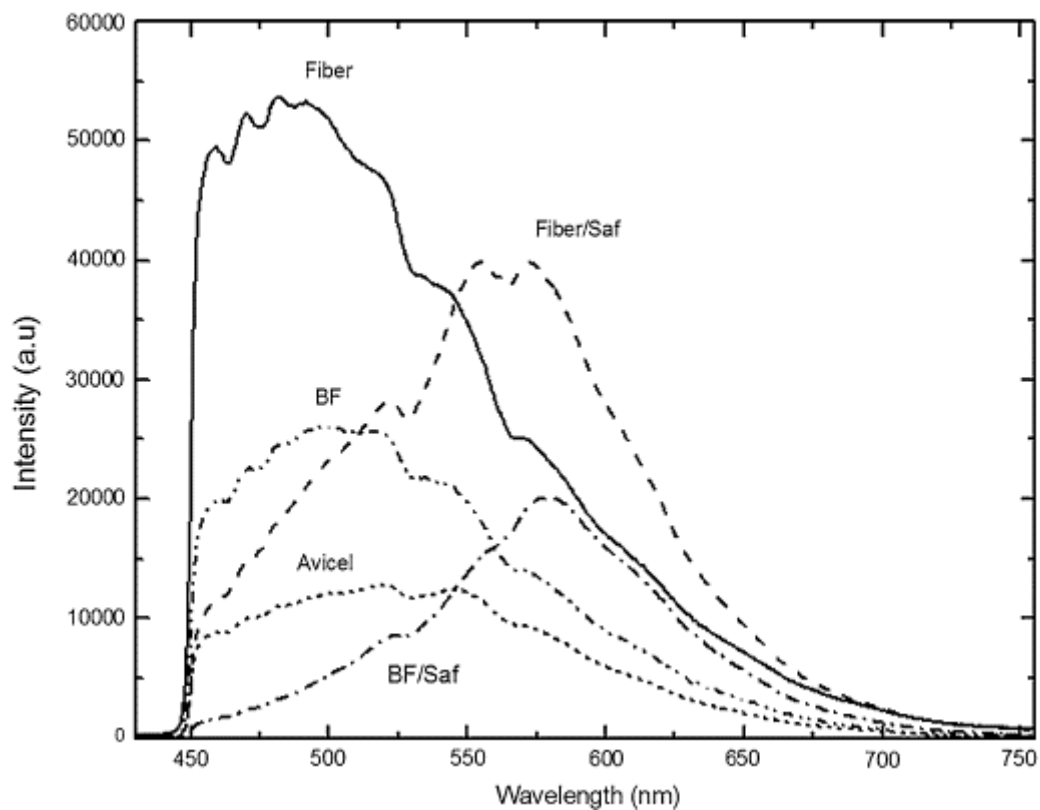


Figure 11. Fluorescence spectra from (solid curve) fibre, (long dashed curve) fibre/safranin, (two dotted dashed curve) BF, single dotted dashed curve) BF/safranin and (shorted dashed curve) Avicel. Samples were excited at 405 nm and spectral intensity was recorded using a linear CCD spectrometer fibre coupled to the binocular side port of the microscope.⁴³

4 CONCLUSIONS

It was used single and two-photon fluorescence microscopy to characterize the autofluorescence from micro-regions of sugarcane bagasse samples. Fluorescence images show that fibril packages of bagasse samples partially lose their longitudinal orientation after chemical bleaching. Extraction of lignin allows the dispersion of the remaining natural fluorophores in the sample, which reduces self-quenching process. The presence of high intensity spots after chemical bleaching indicates that fluorescent lignin derivatives remain in some regions of the lignocellulosic matrix. Our results were able to provide information related to the morphological properties and lignin distribution in sugarcane bagasse samples. In addition, it is possible to understand how the bleaching process affects these parameters. Therefore, this study provides support for future site-specific morphological analyses of the effects of different pre-treatments usage on cellulose hydrolysis, which is an important issue in second-generation bioethanol production.

CHAPTER 2

PRODUCTION AND OPTICAL MICROSCOPY CHARACTERIZATION OF NANOCRYSTALLINE CELLULOSE

ABSTRACT

Nanocrystalline cellulose (NCC) is a rigid rod-shaped fibre with one to one hundred nanometres in diameter and tens to hundreds of nanometres in length, always with a large length / diameter ratio. Due to its properties, NCC can be used for different applications such as in regenerative medicine, in optical materials, and in composites used in automotive industry. The characterization of NCC has been performed by XRD, IR spectroscopy and TEM. However, a thorough understanding about its morphology and composition is still being uncovered. Different techniques of fluorescence microscopy in combination with steady-state and time-resolved fluorescence spectroscopy represent potential tools to study NCC. In this chapter, the whole procedure of NCC obtaining via an adapted acid hydrolysis of Avicel® is described. Afterwards the material was characterized by classic electron microscopy SEM and TEM, confirming the rod-shaped morphology and the nano-sized structure. Wide field microscopy was applied as fluorescence microscopy tool to characterize the NCC when dispersed in two distinct polymeric solutions of PVA and PVP. Because of the hydrophilicity of NCC, the wide field images showed the well-dispersed NCC in the solution of PVA/water, while the solution of PVP/isopropanol showed the formation of NCC self-aggregates into the polymeric matrix. The last step of this chapter describes the characterization of NCC structures by using the super-resolution fluorescence microscopy STED (Stimulated Emission Depletion). The images obtained by STED showed NCC morphology with resolution down to 50 nm, allowing the comparison with TEM and AFM microscopy results.

1 INTRODUCTION

Nanocrystalline cellulose (NCC) is cellulosic materials with dimension in nanometre range. Those materials show distinct behaviour and different physicochemical properties when compared to larger cellulosic fibres. NCC may be obtained from two different types of sources. Plant materials are the most common ones used in the NCC obtaining. There are other cellulosic sources from which NCC has been isolated, including tunicates, bacteria and algae.⁵⁸

NCC is described as a rigid rod-like particle with widths and lengths of 5 – 70 nm and 100 – 2000 nm respectively. The particles are highly crystalline, with crystalline index between 54 and 88%.⁵⁹ The variety of thickness, lengths, morphologies and degree of crystallinity depends on the source of cellulosic material and conditions under which production is carried out as well as on the experimental technique used.³⁴ NCC isolated from tunicate has been reported to have dimension of 8 – 20 nm in thickness and lengths about 1 μm .⁶⁰⁻⁶² There are some reports related to NCC obtaining via sulfuric acid from cotton-Avicel® with thickness about 10 – 100 nm and lengths from 1 μm to 2 μm .⁶³⁻⁶⁵

The Figure 12 shows how cellulose may be found in nature, and gives details of the cellulosic fibre organization and the basic chemical structure of cellulose.

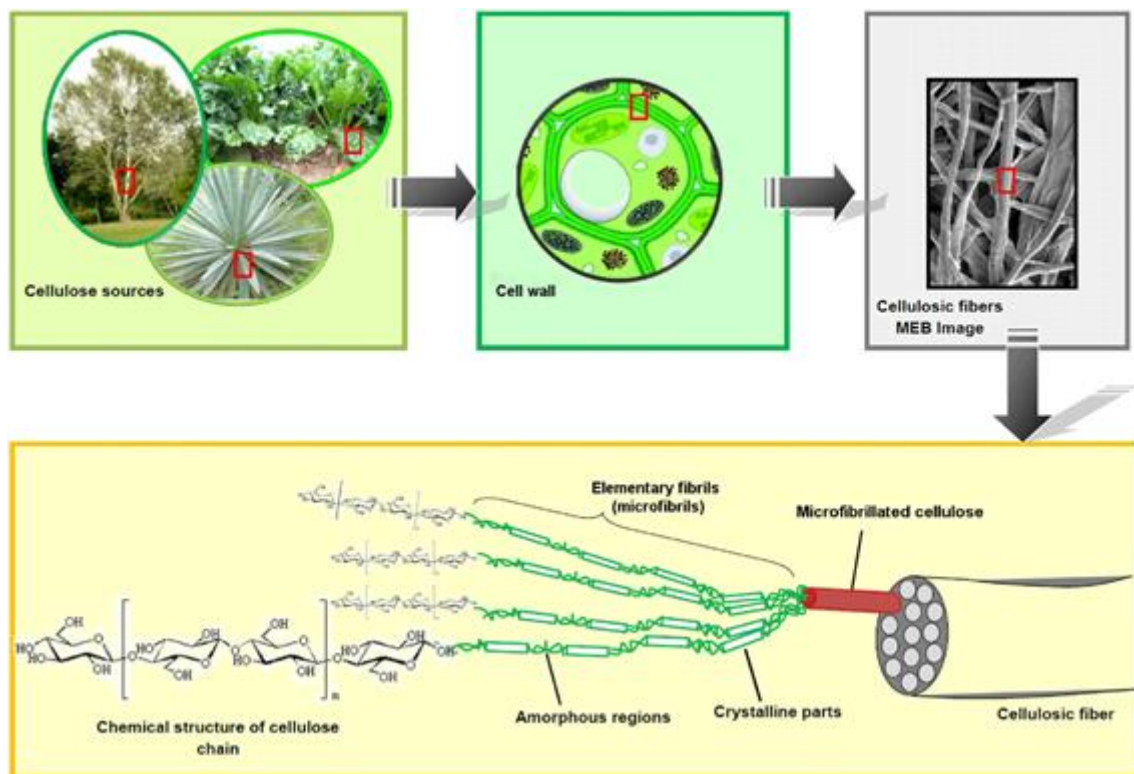


Figure 12. From the cellulose sources to the cellulose molecules: Details of the cellulosic fiber structure with emphasis on the cellulose micro fibrils.⁶⁶

The hydrolysis process occurs preferentially in amorphous domains, whereas crystalline regions are more resistant to acidic attack. Typical procedures for the production of NCC involve the following steps:

1. Strong acidic hydrolysis of cellulosic material under controlled conditions of temperature, time, stirring, concentration, and the acid/cellulose ratio;
2. Dilution with cold water to stop the reaction and repeated washing with successive centrifugation process;
3. Extensive dialysis against distilled water to fully remove free acid molecules;
4. Sonication to disperse the nanocrystals as a uniform stable suspension.

Several studies have been performed over the last decades, and they are related to the application of NCC as filler in nanocomposites for improving mechanical and barrier properties.^{7; 34; 67-75} In the last years, attention has been devoted to studies involving the application of NCC in different materials, such as foams, aerogels,⁷⁰ building block for selective membranes,⁷⁶ adhesive materials,^{70, 77} lithium battery, and in mechanical reinforcement agent for low thickness polymer electrolytes. The intermolecular hydrogen bonds of the cellulose molecules result in strong interactions between the fillers and the polymeric matrix, showing better composite properties compared to the pure polymer matrix. Another important effect of NCC is the high flexibility of the cellulose polymer that provides an entanglement effect with the polymer matrix that contributes to improve mechanical and thermal properties.⁷⁸⁻⁸¹

Different techniques have been employed to perform the characterization of nanocrystalline materials. The crystallinity index, in general, is determined by X-ray diffraction (XRD) technique.^{82; 83} The chemical composition may be determined by Raman and infrared spectroscopy.^{14; 70} Aspects related to the morphology are generally investigated by microscopy techniques, such as, transmission electron microscopy (TEM), scanning electron microscopy (SEM), and atomic force microscopy (AFM).^{84- 87} Light microscopy has been a useful technique in investigation of different lignocellulosic materials,^{15; 88; 89} and possesses the advantage of being non-invasive and non-destructive method. In that context, NCC could be characterized by light microscopy technique, such as, confocal and wide field microscopy (WFM), providing morphologic information that is not available by other techniques.

Advances in optical microscopy have been established in the last decade, generating a great impact in areas of chemistry and biology.^{90; 91} Recent progresses in optics allowed breaking the diffraction limit by the developing of the so called super resolved

microscopy techniques as, for example, the STED method.⁹²⁻⁹⁴ Methods with super-resolution assure high space sensitivity, allowing the investigation of unknown details in natural and artificial systems, up to the single molecule level.^{95; 96}

The NCC has great potential generating highly functionalised nanomaterials to different areas, such as, intelligent recovering, pharmaceutical applications, nanocomposites and electronic materials. The effectiveness of the use of nanocrystalline cellulose is related to the structural knowledge of the system. From this point of view, the application of super-resolution technique STED represents a very useful tool to investigate NCC single fibres.

2 EXPERIMENTAL

2.1 Production of nanocrystalline cellulose by acid hydrolysis

The commercial microcellulose Avicel® was purchased from Sigma-Aldrich. The methodology used to obtain nanocrystalline cellulose was adapted from Mandal and Debabrata.⁸⁶ The hydrolysis of Avicel® was carried out by the use of sulphuric acid. For each 1g of Avicel® was used 6 mL of sulphuric acid 54% (v/v). The hydrolysis was performed under stirring during 60 minutes at 50 °C. At the end of the reaction, the mixture showed a lightly brownish colour. Subsequently, the suspension was cooled down by the addition of cold distilled water. Afterwards, the washing process with Milli-Q water and centrifugation at 14,000 rpm was performed several times until the supernatant shows pH around 7. Then, the suspension was filtered using a membrane with the diameter mesh at 200 nm.

2.2 Preparation of nanocrystalline/polymer composites

Solutions of polyvinyl alcohol (PVA, MW 89,000 – 98,000) and polyvinylpyrrolidone (PVP, MW ~55,000) were prepared by their dissolution in water and isopropanol (2% w/w). The polymeric solution was kept under stirring during 20 minutes at 40 °C. Hereafter, the NCC suspension was added to the polymeric matrix (10% w/w) and kept under stirring during 30 minutes. Finally, the samples were deposited on cover slides and stored in a desiccator.

2.3 Techniques

2.3.1 X-ray diffraction

The diffractograms were obtained from diffractometer Rigaku, operating at 50 kV and 100 mA by irradiation of CuK α ($\lambda = 1.5406 \text{ \AA}$). The measurements were carried out at

room temperature (25 °C) and at angle 2θ from 5 to 40° (2°.min⁻¹). The crystallinity index was calculated from the diffractogram peaks, taking into account the Gaussian distribution function related to the amorphous and crystalline areas⁹⁷. The equation 1 was applied to obtain the crystallinity index:

$$I_c(\%) = \left(1 - \frac{A_a}{A_t}\right) \times 100$$

Equation 1

Where A_a is the corresponding area under the amorphous curve and A_t is the total area of all peaks, including the amorphous curve.

2.3.2 Transmission electron microscopy

NCC was measured in a Tecnai™ G2 F20 microscope, operating in STEM mode, in bright field and dark field. Before measuring, the samples were sonicated for 10 minutes and the suspension was dropped on a grid and stored in a desiccator for 24 h.

2.3.3 Scanning electron microscopy

The methodology used to obtain scanning electron microscopy images of NCC was previously described in section 2.3.1 of Chapter 1.

2.3.4 Confocal fluorescence microscopy

The confocal microscopy and steady-state emission measurements of NCC were implemented by using a Cube Coherent diode laser line at 405 nm operating with adjustable output power from 1 to 40 mW. Details of methodology and instrumentation used were described in section 2.3.2 of Chapter 1.

2.3.5 Wide field microscopy

The wide field fluorescence images were obtained by using an inverted IX71 microscope and an objective model UPlanFLN Olympus, with magnifying of 100X and numerical aperture of 1.3 in oil. The laser Cobolt Blue operating at 473 nm with average power of 50 mW was used as the light source. Details of methodology and instrumentation were described in section 2.3.3 of Chapter 1.

2.3.6 Super-resolution microscopy by stimulated emission depletion (STED)

The samples used in STED microscopy were prepared in aqueous solution and labelled by the dye ATTO-647N-COOH (ATTO-TEC) at concentration of $1 \cdot 10^{-5}$ mol.L⁻¹, under stirring for 24 h. Subsequently, they were washed 5 times for 10 minutes with distilled water at the temperature of 40 °C and finally spin-coated (1500 rpm, 90 s) onto the surface of cover slide of 22 x 22 mm.

STED super-resolution images were obtained in an inverted IX71–Olympus microscope, using a piezoelectric controller, E-710.3CD–PI, to perform the nanometric scanning. A mode-locked Picoquant laser operating at 635 nm and 80 MHz of pulsed frequency was used for sample excitation while depletion was provided by a laser line at 750 nm. The excitation and depletion beams were collimated by dichroic mirror before focused by an immersed oil 100x objective of numerical aperture of 1.3 (UPLSAPO 100XO/PSF, Olympus). The fluorescence emission signal from the sample was collected by the objective and separated from the laser line by using dichroic lenses (FF01 -740- DI01 and FF662-FDi01, Semrock). Communication and interfacing between the instruments were made by a software programming in C# developed in the Laboratory for Photochemistry and Spectroscopy of KU Leuven.

3 RESULTS AND DISCUSSION

3.1 Characterization of Avicel® NCC by electron microscopy and X-ray diffraction

Samples of NCC were obtained from micro-particles of cellulose Avicel®. The hydrolysis of cellulose under controlled conditions generates nanocrystals, which are composed of well-defined fibrils of cellulose chains, showing a hard linear arrangement. Figure 13 shows scanning electron microscopy images of microcrystalline cellulose Avicel®, which are small particles aggregated with irregular shape.

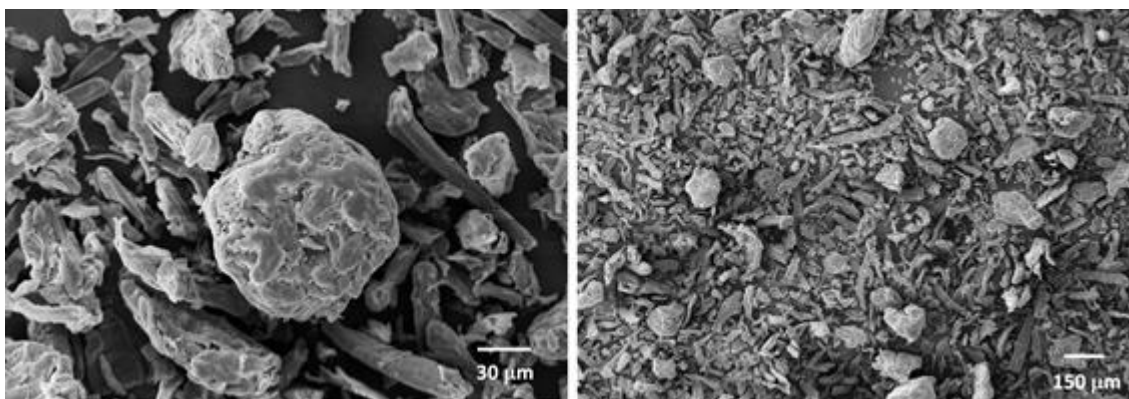


Figure 13. SEM images of Avicel® samples. Morphologic details of microcellulose particles.

Figure 14 shows the transmission electron microscopy of NCC obtained by sulfuric acid hydrolysis. The morphology of the particles is nearly flat and their average length is in between 100 – 200 nm, while the distribution of their diameter is from 10 – 40 nm. This special shape of NCC is due to the action of sulfuric acid in amorphous areas of the cellulose, keeping the crystalline one practically undamaged.

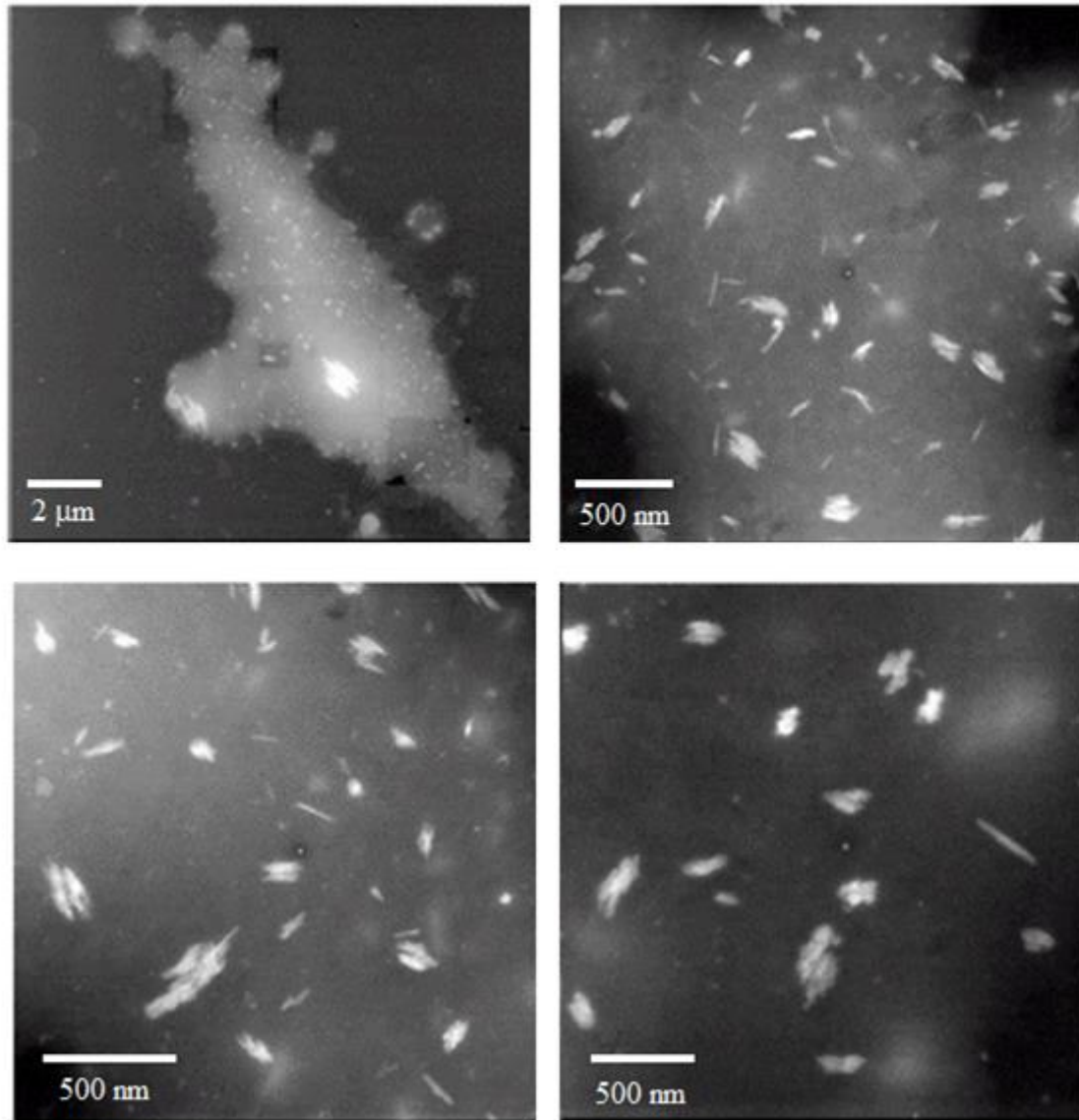


Figure 14. TEM images of nanocrystalline cellulose, obtained from sulphuric acid hydrolysis.

The properties related to morphology and structure of NCC may be determined by its origin and extraction conditions.⁶⁰ Crystals of cellulose are generated from the synthesis of different biomass species. The origin of the structure of cellulose nanocrystals is associated to the formation of micro fibrils, during the deposit in layers on the cellular walls. The number of micro fibrils sideways attached to each other changes according to

the specific cellular wall. Therefore, after the acidic hydrolysis process, it is possible to obtain NCC with a range of particle sizes.

Figure 15 shows the X-ray diffractogram of Avicel® and NCC. Both of them have three peaks related to the cellulose at $2\theta = 14.7^\circ$; 16.4° e 22.6° .⁹⁸ The peak at 22.6° is sharper after the hydrolysis process, representing a well-defined structure of the crystalline lattice at plane (2 0 0). The determination of the index of crystallinity was obtained by the method reported by Segal *et al*,⁹⁹ using the intensity of the crystalline and amorphous values as comparison parameter. The crystallinity index for Avicel® and NCC were 57% and 70%, respectively. The increase of the crystallinity index after the hydrolysis is attributed to the removal of amorphous regions of the cellulosic matrix.

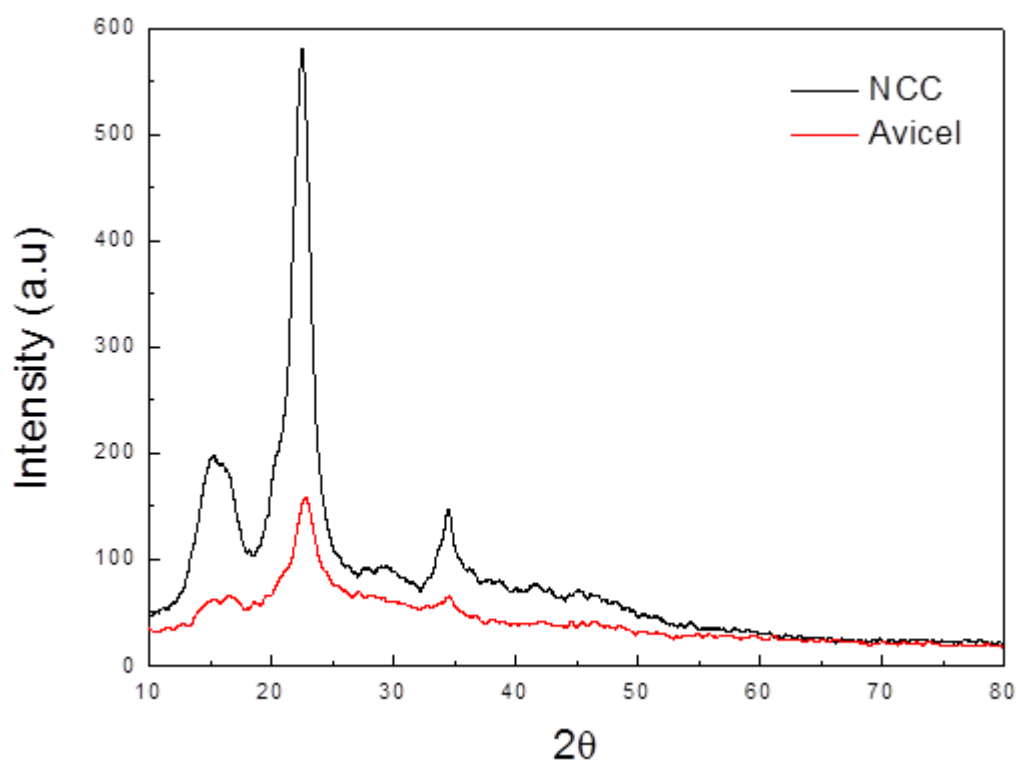


Figure 15. Diffratograms of Avicel® and NCC. The values of crystallinity index calculated from method Segal *et al* were 57% to Avicel® and 70% to NCC.

3.2 Characterization of Avicel® NCC by wide field microscopy

Images of autofluorescence of Avicel® and NCC are shown in Figure 16. Cellulosic materials have a broad absorption spectral region, even after delignification process. In Figure 16 (a and b) it is shown the morphologic characteristics of Avicel®, exhibiting irregular rod-shaped particles with diameter ranging from 30 μm to 60 μm . This result may be compared with particles illustrated in Figure 13 (SEM images). The images in Figure 16 (c and d) are related to samples of NCC. After the hydrolysis, a significant decrease of length and diameter of the nanoparticles occurs. The recorded images of NCC by wide field microscopy (vide infra) were limited due to the high scattering and low fluorescence intensity of the material precluding resolution of the nanoparticles.

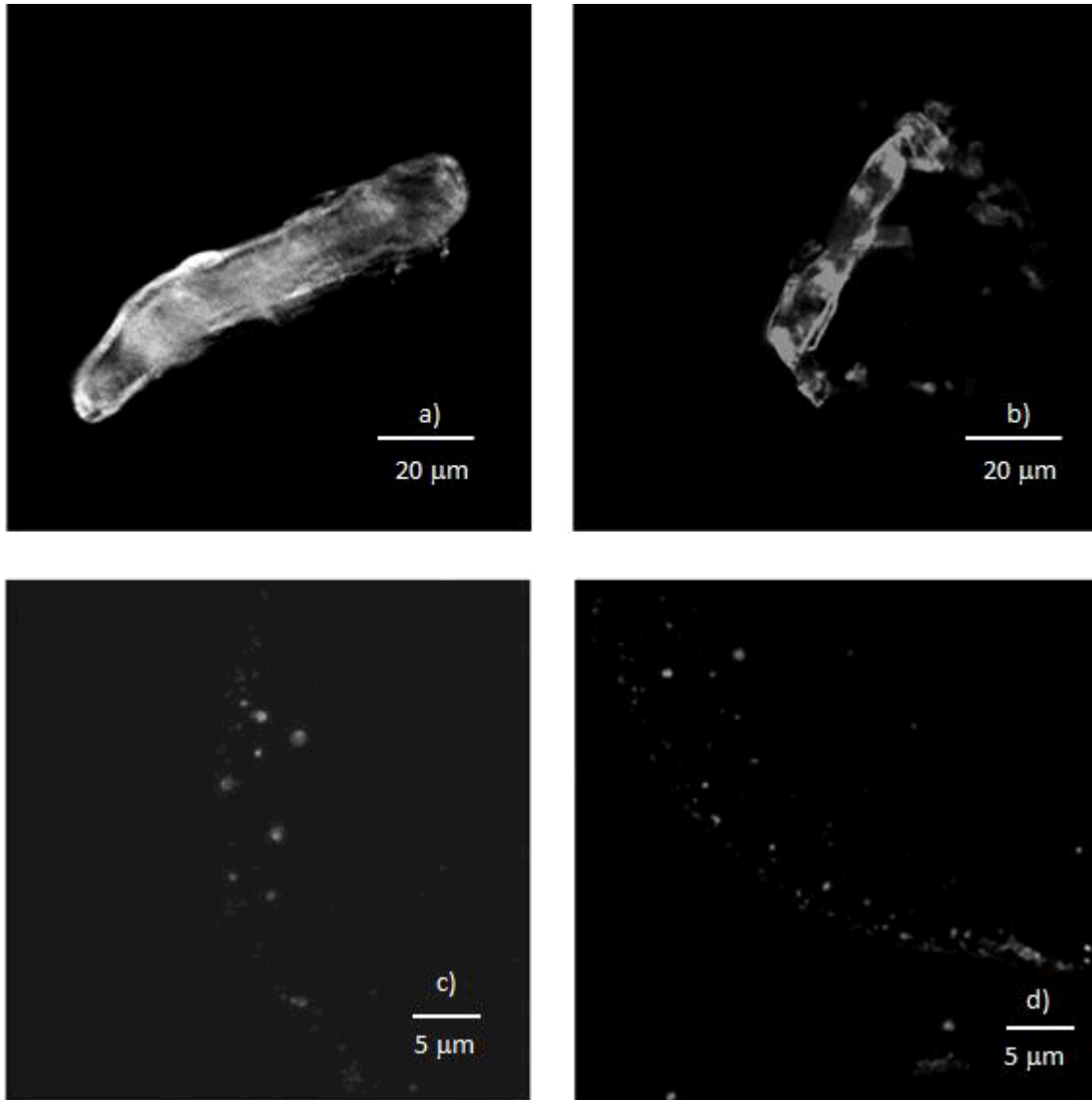


Figure 16. WFM images of Avicel® (a and b) and NCC (c and d).

3.3 Characterization of Avicel® NCC by steady-state and time-resolved fluorescence spectroscopy

Emission spectra of Avicel® and NCC showed in Figure 17 were obtained via measurements using the same confocal microscopy setup, and the source of light used was a laser with wavelength at 405 nm. The Avicel® fluorescence spectrum shows a maximum emission band at 540 nm. Whereas the emission band of NCC occurs in a high-energy region band below 440 nm (the cut off filter used precludes the

determination of the emission maximum). Nevertheless, an emission blue shift after hydrolysis process is achieved.

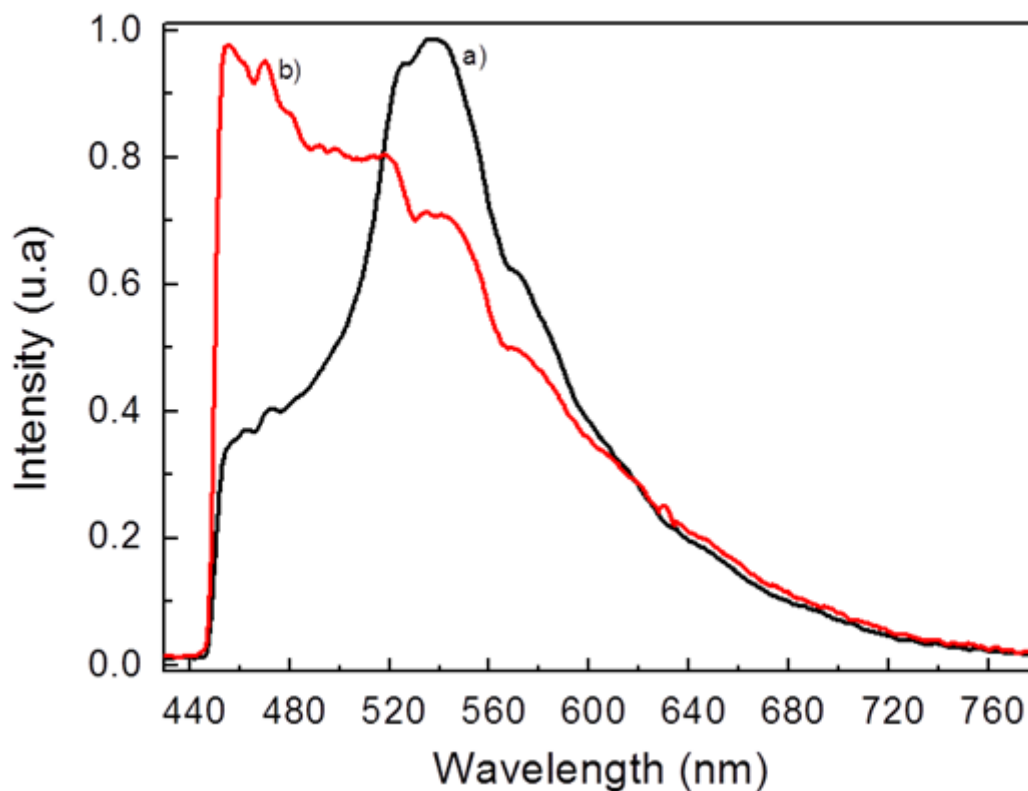


Figure 17. Fluorescence spectra of a) Avicel® and b) NCC obtained by excitation at 405 nm.

Fluorescence decay traces measurements were obtained via 2-photon excitation, using a pulsed laser at 800 nm. Decay analyses were performed by FAST software (Edinburgh Instruments), fitted with multiexponential function without deconvolution. The decays of Avicel® and NCC are shown in Figure 18.

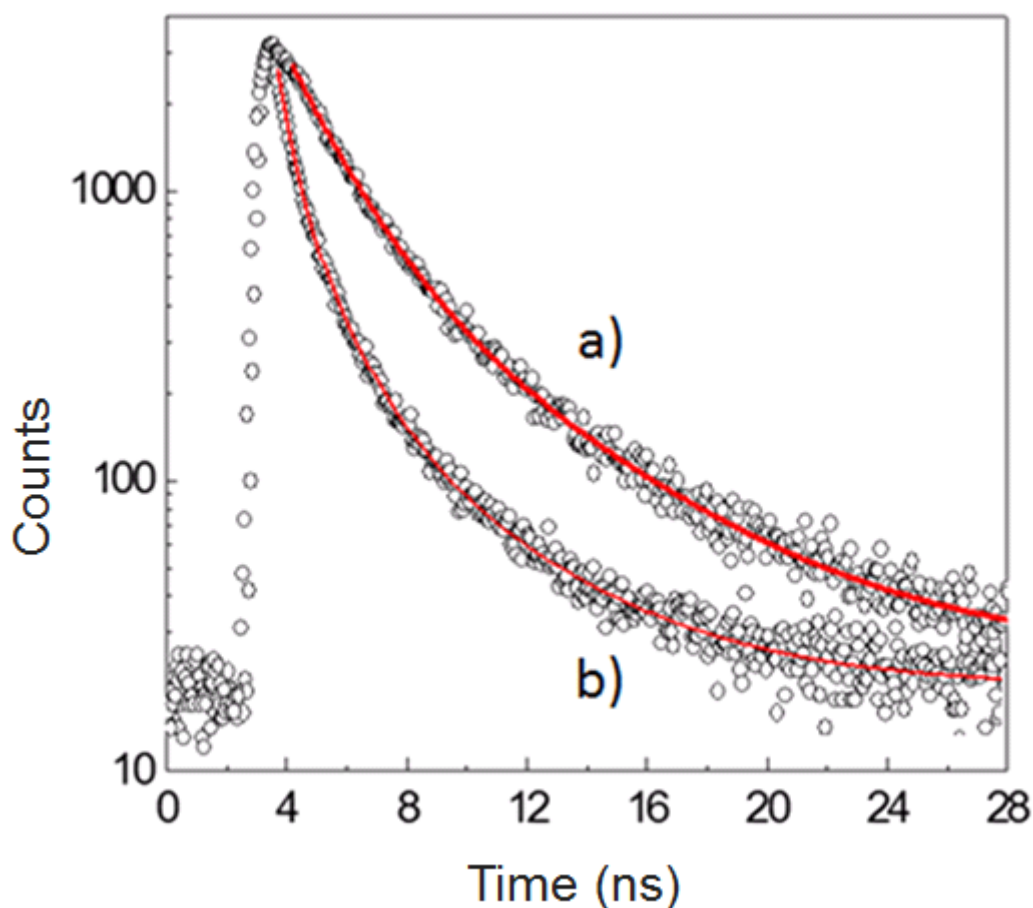


Figure 18. Fluorescence decays of a) Avicel® and b) NCC obtained by two-photon excitation at 800 nm.

A biexponential function was applied to fit the fluorescence decay of Avicel®, while the decays of NCC were only fitted with three exponential components. The decay times obtained are shown in Table 2. For Avicel®, the values were 1.74 e 5.5 ns. For NCC, the decay times recovered were 0.46; 1.32 and 4.35 ns.

After sulfuric acid hydrolysis of Avicel® to obtain NCC fibres the two longer fluorescence decay times decreased and a third and faster component appeared. These features may be related to the polysaccharide depolymerization forming reactive products. The acid hydrolysis may generate fractions of xyloses, acetic acid, furfural

and hydroxymethylfurfural (HMF).^{100; 101} Some of these aldehydes can condensate, producing oligomers with new fluorescence properties.

Table 2. Decay times and normalized amplitude related to Avicel® and NCC.

Sample	τ_1 (ns)	τ_2 (ns)	τ_3 (ns)	*a ₁	*a ₂	*a ₃	$\langle\tau\rangle$	τ^2
Avicel	1.7	5.5		0.75	0.25		3.7	1.07
NCC	0.5	1.3	4.3	0.54	0.37	0.09	2.1	1.07

* weighted average amplitude of lifetime

3.4 Dispersion of NCC in polymers

Factors as mechanical strength, high superficial area and optical properties make the application of nanocrystalline cellulose in several materials a prominent area of investigation. The use of nanocrystalline cellulose as a reinforcement in polymeric matrices has been highlighted over the last years.^{7; 102; 103} In this scenario, fluorescence microscopy techniques have been an useful tool for the study of parameters involved in the production of nanocrystalline/polymeric composites. The images of wide field microscopy of the composites produced from dispersion of NCC in polyvinylpyrrolidone (PVP) in isopropanol solution and polyvinyl alcohol (PVA) in water solution are shown in Figure 19.

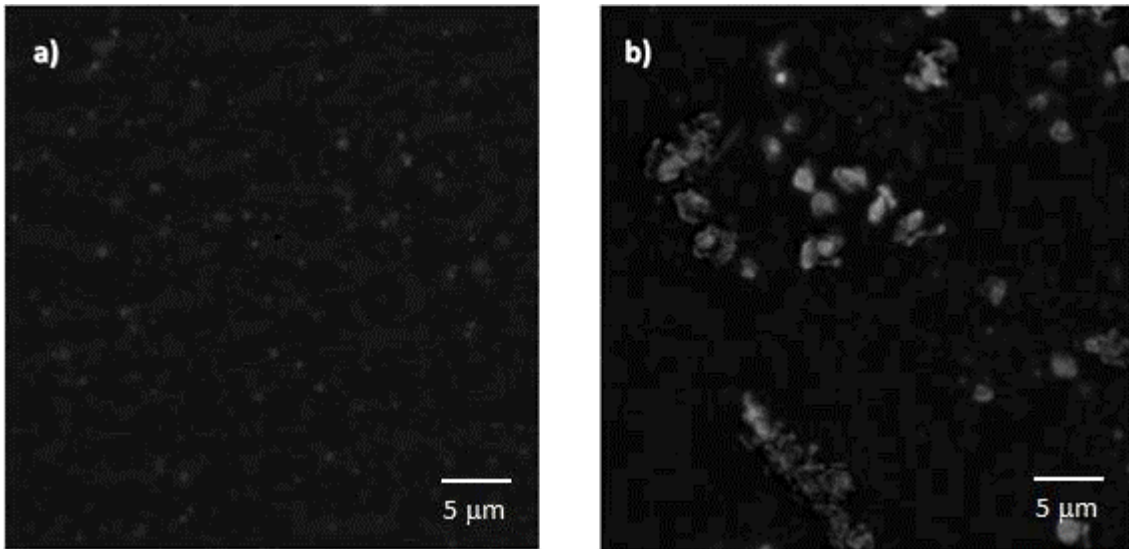


Figure 19. Wide field fluorescence images of a) solution of PVA-water/NCC and b) PVP-isopropanol/NCC.

Polyvinyl alcohol (PVA) may be used in a large range of applications because of its specific properties as dielectric strength, elasticity, hydrophilic character, and the possibility to produce good films via solution casting.^{104; 105} On the other hand, Polyvinylpyrrolidone (PVP) has been used for the production of nanofibers by electrospinning process because of its biocompatibility, harmless and stabilizer characteristics.^{106; 107} PVA/NCC/water solution and PVP/NCC/isopropanol solution demonstrate the relation between the hydrophilicity of medium and degree of NCC dispersion.

Figure 19-a shows the image of PVA-water/NCC, in which the cellulosic material is completely dispersed in the polymeric matrix. This behaviour occurs because of the hydrophilic property of the NCC, allowing the fibre percolation in the aqueous system of PVA. The strength to the shearing and other properties may be related to the degree of dispersion in the polymeric matrices. Figure 19-b clearly indicates the formation of

some self-aggregates in the PVP-isopropanol/NCC composite, without complete dispersion. The aggregation process occurred due to incompatibility of isopropanol used in the PVP solution with cellulose-based materials.

3.5 Super-resolution optical microscopy of Avicel® and NCC

The NCC was labelled *via* electrostatic adsorption using the dye ATTO-647N (ATTO-TEC). Figure 20-a shows an image obtained by a conventional confocal microscopy and the Figure 20-b shows an image obtained by STED microscopy at same area.

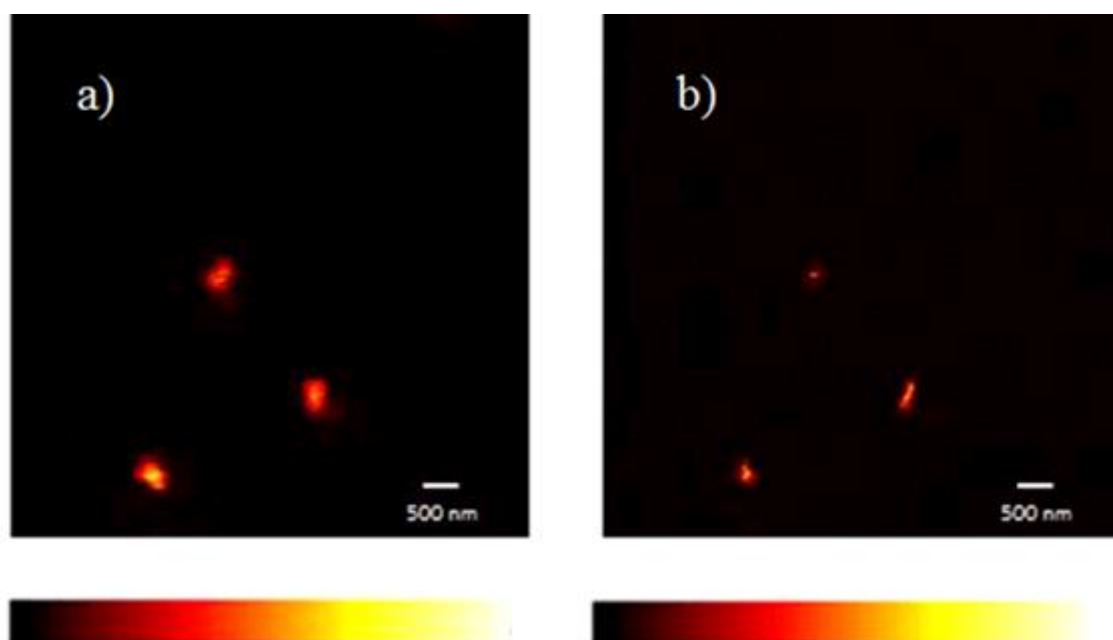


Figure 20. Images of NCC obtained via sulphuric acid hydrolysis. a) Confocal: $\lambda_{exc} = 635$ nm, power = 28.5 mW, size = 400x400p (10x10mm), dwell time = 0.4 ms and b) STED: $\lambda_{exc} = 750$ nm, power = 4.4 mW (20mW), size = 400x400p (10x10mm), dwell time = 0.4 ms.

In Figure 21 is showed an estimation of the confocal and STED resolution (in XY plane). The full width at half maximum (FWHM) of the Gaussian fit from the distribution of the count in function of the position is 306 nm when confocal

microscopy is used. The corresponding value determined by STED microscopy fitted by Lorentzian distribution is 50 nm, 6 times smaller than confocal microscopy result.

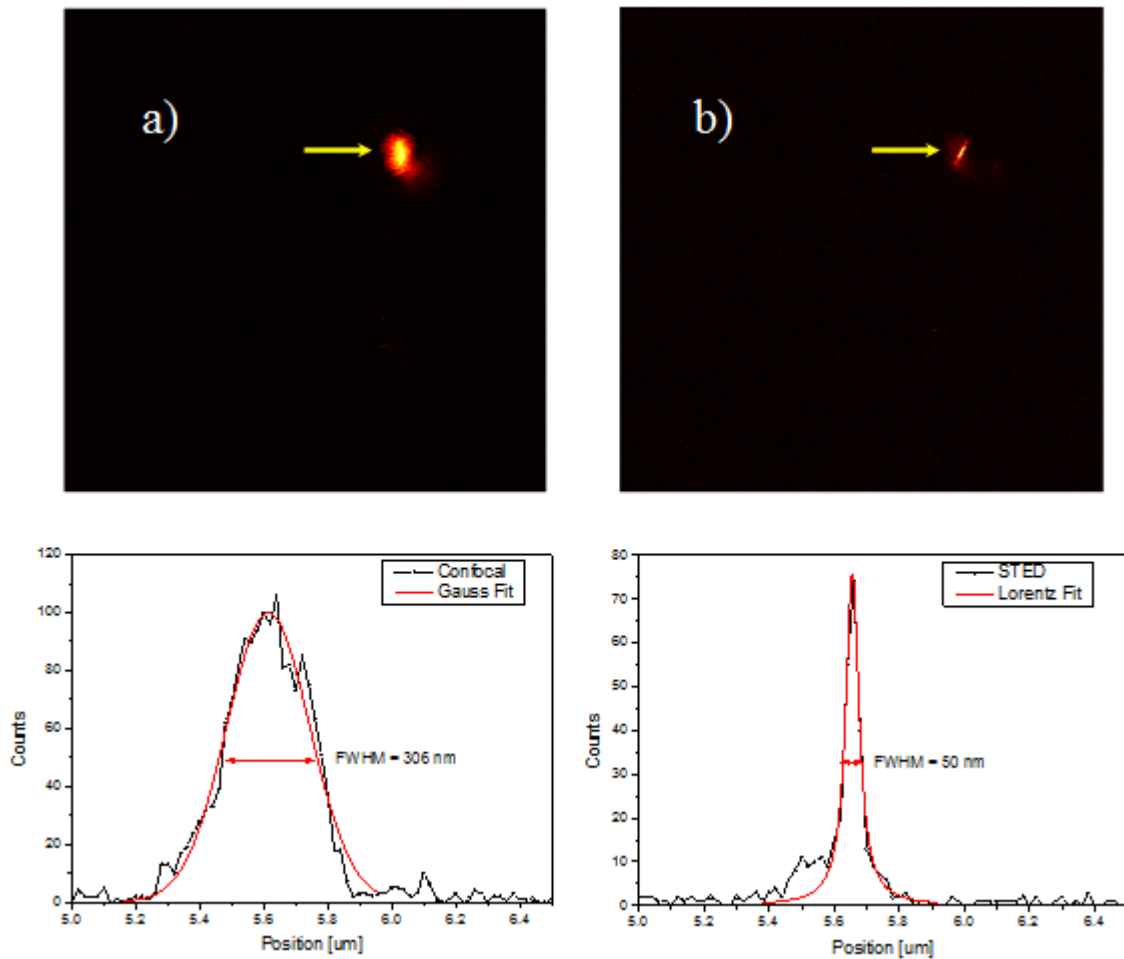


Figure 21. a) Confocal and b) STED microscopy images and the respective profile of the spot pointed from the yellow arrow.

The knowledge about morphological, structural and chemical composition through fluorescence images with resolution below the diffraction limit represents a major step in understanding how different processes relate to cellulose processing. Different publications have reached STED images with resolution in the range of 30–80 nm.^{94; 108;}
¹⁰⁹ The images acquired in our work, by STED microscopy show that the super-resolution microscopy provides images with more details, overcoming the diffraction limit, with resolution of about 50 nm.

4 CONCLUSIONS

Regarding the study of samples of nanocrystalline cellulose, using conventional techniques, such as, electron microscopy (SEM and TEM), fluorescence microscopy (wide field and confocal), and stationary fluorescence spectroscopy were carried out and allowed the obtaining of important information about the NCC. The material maintained its fluorescent properties after the hydrolysis process. Due to acid attack, new fluorophores were generated and adsorbed onto the NCC surface, therefore, generating a third decay component. Fluorescence microscopy techniques also have shown to be useful for the evaluation of nanocrystalline cellulose dispersion in polymeric matrices. Hydrophilicity of the polymer solution, in which the NCC is immersed, influences its degree of dispersion and can be detected by wide field microscopy.

CHAPTER 3

FLUORESCENT LABELLING OF NANOCRYSTALLINE CELLULOSE

ABSTRACT

The use of NCC as a reinforcement agent in polymer composites has been successfully applied in the improving of resilience and toughness. Thus, the obtained material offers a distinctive combination of desirable physical properties with environmental benefits. The attaching of fluorescent molecules to the cellulose backbone is one of the most useful ways to study properties of NCC. Several studies have been performed to chemically modify the surface of nanocrystalline cellulose. In that context, click chemistry reactions have been applied to the fluorophore coupling at the functionalized surface. However, further studies to characterize dynamic properties of NCC in polymeric solutions are necessary. In this chapter, the results about NCC covalently labelled by click chemistry reaction using the dye ATTO-532-alkyne are discussed. The diffusion coefficient of NCC in water was determined at single molecule level by fluorescence correlation spectroscopy (FCS) method. Additionally, NCC was also placed into different concentrations of polyethyleneglycol (PEG) solutions, containing varied polymer amounts. The properties of the aqueous suspension of NCC and the polymeric solutions based on NCC/PEG/water, NCC/PEG/methanol and NCC/PEG/acetonitrile were evaluated using FCS and WFM techniques. Because of H-bonding interaction between PEG and OH groups on the NCC surface, the diffusion of NCC fibre in polymeric solution became slower upon addition of PEG, independently of the solvent used, obstructing the free diffusion of the particle.

1 INTRODUCTION

Nanocrystalline cellulose shows properties related to non-toxicity, biocompatibility, biodegradability and robust physical properties, such as, large surface area and mechanical strength. The possibility of surface modification expands even more the usefulness of NCC in many products.^{110; 111}

Due to a large quantity of hydroxyl groups on the surface of NCC, different chemical modifications have been attempted, including esterification, etherification, oxidation, silylation, polymer grafting, etc.¹¹²⁻¹¹⁴ All functionalization methodologies have been mainly conducted aiming at introducing negative or positive charges on the surface of NCC. The main challenge for the chemical functionalization of NCC is performing the modification only onto the surface, so that the original morphology is preserved, any polymorphic conversion is avoided, and the integrity of the crystal is maintained.^{113; 115}

The chemical modification of NCC has been extensively studied pointing toward the improvement of the compatibility with hydrophobic polymer matrices to afford nanocomposites with unique mechanical properties.^{1; 116; 117} Figure 22 shows different chemical processes that can be used to modify the NCC surface.

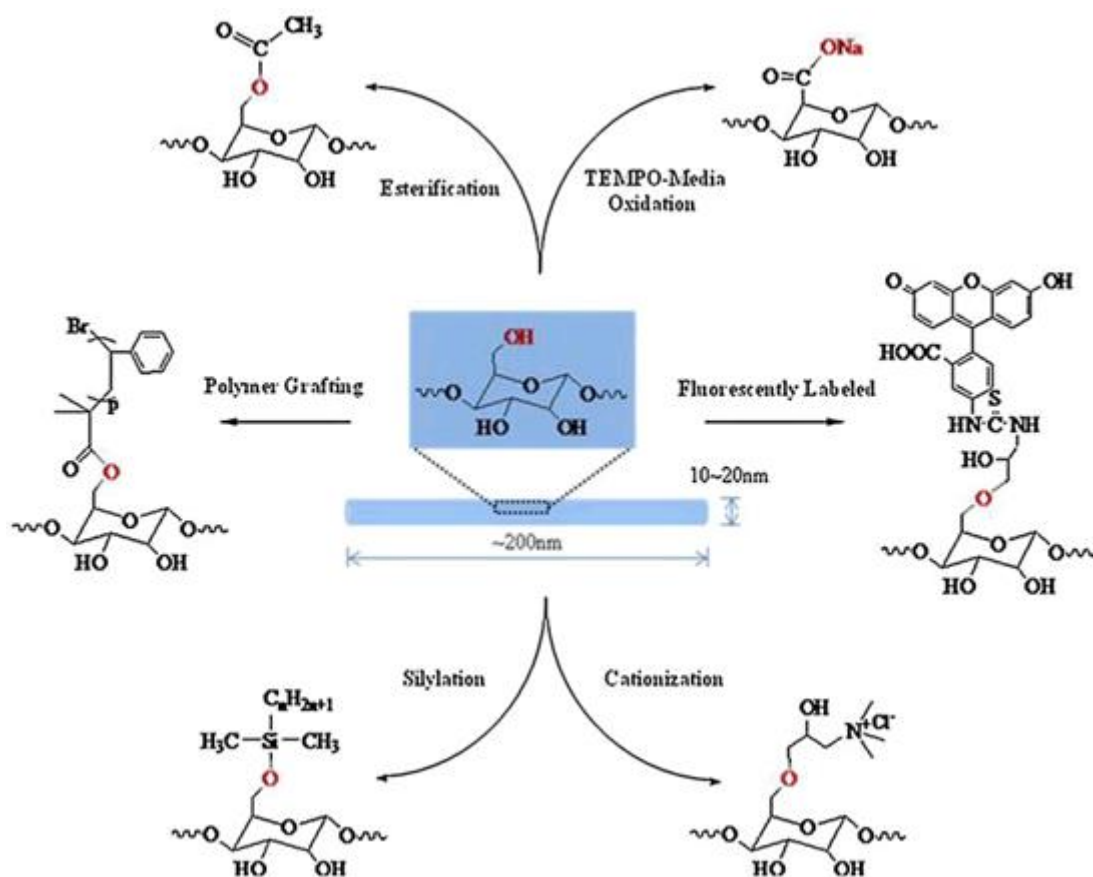


Figure 22. Schematic diagram illustrating the various types of chemical modifications on NCC surface.³⁵

Fluorescent functionalization of NCC is an important achievement for applications in sensor, in cell uptake, and in cell viability. The fluorescent labelling of NCC surface has been performed by different methodologies.^{88; 118; 119} Among them, the click chemistry reaction is one of the most promising methods for fluorescent labelling of the cellulose surface. The step of introduction of functional groups, which are azide or alkyne, onto the surface, in combination with the step of fluorophore coupling via click chemistry represent a pivotal role for the development of a versatile labelling method. This kind of reaction enables the coupling of several dyes or different types of probes.^{118; 120-123}

By definition, click chemistry reactions are characterized by high yield, fast reaction, selectivity, and inoffensive by-products.^{124; 125} The azide alkyne cycloaddition using a

copper catalyst at room temperature is a typical example of click chemistry reaction.¹²⁴ Labelling polymer with different classes of dyes, which are related to specific functions or diverse colours, is of great interest for biological application, for instance, multimodality molecular imaging^{126; 127} or for studies of electronic energy transfer¹²⁸.

The objective of the research described in this chapter was the fluorescent labelling of NCC and the investigation of diffusion properties. For the labelling process, firstly, azide groups were attached onto the backbone of nanocrystalline cellulose, acting in aqueous reaction media, by the subsequent coupling of ATTO-532-alkyne by copper-catalysed azide-alkyne cycloaddition (CuAAC).

Fluorescence correlation spectroscopy (FCS) is a single-molecule technique applied to determine local concentrations, mobility coefficients or characteristic rate constants of inter or intramolecular reactions of fluorescently labeled biomolecules in nanomolar concentrations.^{129; 130} FCS measures and correlates fluctuations in fluorescence intensity within a very small detection volume. These fluctuations are obtained from diffusion of fluorescent molecules into or out of a confocal volume defined by a focused laser. These signal fluctuations may be analysed by correlation functions.^{129; 131-134}

The diffusion properties were determined from autocorrelation curves obtained *via* FCS measurements. The nanocrystalline cellulose was dispersed in different concentrations of polyethylene glycol (PEG) in water, methanol and acetonitrile. All those systems were investigated by single molecule techniques FCS and WFM/TIRF measurements.

2 EXPERIMENTAL

2.1 Obtaining NCC

NCC was obtained from sulfuric acid hydrolysis of Avicel® according to the process described in Section 2.1 of Chapter 2.

2.2 Preparation of 1-azide-2,3-epoxypropane

Epichlorohydrin was the compound responsible to start the synthesis of 1-azido-2,3-epoxypropane. The ring-opening reaction of the epoxide with azide-ion was performed according to a modified method of Fringuelli¹³⁵ and Pahimanolis¹³⁶. The first step was the mix of isopropanol (10.9 mL) and acetic acid (0.72 mL, 12.58 mmol) with a solution of NaN₃ (0.8177 g, 12.58 mmol) in 7.40 mL of water. Epichlorohydrin (0.66 mL, 8.42 mmol) was then added under stirring and the reaction was continued at 30 °C for 24 h, under light protection. Subsequently, a water solution of NaNO₂ (11.5 mL, 41.6 mmol) was added, followed by the dropwise addition of HNO₃ (0.576 mL, 8.38 mmol) for the elimination of any excess of azide-ions. The obtained solution of 1-azide-3-chloropropanol was stored in dark at room temperature and used without further purification.

The conversion of 1-azide-3-chloropropanol to 1-azido-2,3-epoxypropane was possible due to the addition of 26.3 mL of 5 M NaOH to the pre-prepared solution of 1-azido-3-chloropropane. The reaction was kept under stirring for 30 min. The obtained solution was immediately used for the azide-functionalization of NCC.

2.3 Introducing azide groups to the surface of NCC

The azide functionalization of NCC was performed following a slightly modified method reported by Pahimanolis and co-authors.¹³⁶ 11.0 mL of 5 M NaOH solution was added to a water suspension of never dried nanocrystalline cellulose (1,000 g, 16.6 g of solid content) and the mixture was stirred for 60 min at 30 °C. The fresh prepared solution of 1-azido-2,3-epoxypropane (197 mL, 84.2 mmol) was then added and the reaction was continued for 24 h at 30 °C (pH = 12). The suspension was then purified with deionized water by several centrifugation (16.000 rpm for 20 min, at 10 °C) and re-dispersion steps until the pH of the suspension became neutral. The azide functionalized NCC was stored under light protection at 4°C temperature for further use.

2.4 Fluorescent labelling of azide functionalized NCC with ATTO-532-alkyne dye

1 mg of ATTO-532-alkyne was dissolved in DMSO at a final concentration of 20 mM. For the fluorescent labelling of azido-NCC, 10 µL of 20 mM ATTO-532-alkyne were added to the suspension containing the azido-NCC. Afterwards, a freshly prepared aqueous solution of CuSO₄·5H₂O (0.017 g, 0.068 mmol) and of ascorbic acid (AAc) (0.030 g, 0.17 mmol) were added. The system was incubated at room temperature for 1 h in dark. Subsequently, an EDTA solution at a concentration 10 fold higher than the CuSO₄ concentration was added to the complexation of the copper ions in excess.

2.5 FCS measurements

The fluorescence correlation spectroscopy (FCS) measurements were carried out in a classical confocal microscope Olympus IX71 setup (Figure 3, Chapter 1). A laser beam (Verdi – 10 mW) was employed as excitation source at 532 nm. A beam expander was placed to overfill the back aperture of the microscope. An oil immersion objective

(100x), with numerical aperture of 1.3 was used to focus the laser beam into the sample. The emission from the fluorophores was collected by the same objective, and passed by a dichroic mirror, pinhole (50 μm) and notch filter before reach onto the single photon counting avalanche photodiode (Perkin Elmer, SPCM-AQR-14). The correlator Flex99-12C was used to generate a real time autocorrelation data from the fluorescence signal. The calibration of the confocal volume were determined using rhodamine 6G as standard.¹³⁷ All the measurements were performed at room temperature.

The spontaneous fluctuations in the fluorescence intensity during the measuring time $F(t)$ of three minutes were detected. The fluctuations are caused by different mechanisms, occurring at single molecule level. From autocorrelation curve is possible to obtain information about fluorophore concentration, translational motion, properties about dark time of the triplet state and its respective population. The autocorrelation function $G(t)$ represents the probability to register later fluorescence signals from the first emitted signal.

$$G(\tau) = \frac{\langle \delta F(t) \cdot \delta F(t + \tau) \rangle}{\langle F(t) \rangle^2}$$

Equation 2

Where $\delta F(t) = F(t) - \langle F(t) \rangle$ and $\langle \rangle$ indicates the time average.

For the determination of diffusion coefficient from autocorrelation curve, it is necessary to define the mean residence time of a fluorophore in the confocal volume. By using a standard fluorophore, with a well-known diffusion coefficient, it is possible to determine the confocal volume size. Knowing the shape of the confocal volume, the diffusion coefficients of different species may be determined. The main responsible by the fluorescence fluctuations during a measuring time is the translational motion of

fluorophore species in and out of the confocal volume. However, most of fluorophore molecules have a significant part of their population that reach the excited state follow to the dark triplet state, which adds another exponential term in the autocorrelation curve as given below.

$$G(t) = \frac{1}{N} \frac{1}{1 + (t/\tau_D)} \frac{1}{\sqrt{\left(1 + t/(w_{xy}^2 \tau_D)\right)}} \left(\frac{1 - T + T e^{-t/\tau_T}}{1 - T} \right)$$

Equation 3

Here, N is the average number of fluorescent species in the observation volume and w_{xy} is the ratio of axial to radial dimensions of the confocal volume. In addition, T is related to the amplitude of the population of fluorophores in the dark state and τ_T is the triplet lifetime of the rhodamine 6G. It is assumed that the dark triplet dynamics is faster than the diffusion time of the dye. From the diffusion time, τ_D , and the radius w_{yz} , it is possible to calculate the diffusion constant, D_i , as:

$$D = \frac{w_{xy}^2}{4\tau_D}$$

Equation 4

For the measurements, coverslips (0.16 mm, 22 x 22 mm, Menzel-Gläser) were cleaned by rinsing Milli-Q water, dried with argon gas and stored in a muffle at 450 °C for 10 h. Afterwards, the coverslips were stored overnight in a chamber under UV-light exposure (354 nm).

Data analysis. All FCS measurements were performed for NCC fibres with length smaller than the diameter of the confocal volume (200–250 nm). The experiments were analysed by calculating the intensity of autocorrelation curves $G(t)$. To determine whether autocorrelation curve should be fitted by a single-component or two-

component, a statistical F-test was performed.¹³³ The diffusion coefficients were evaluated from the average value of three or four measurements. Standard deviations were used as indicator of the data error.

2.6 Wide Field Measurements

The fluorescence wide field images were obtained by using an inverted IX71 microscope and an objective model UPlanFLN Olympus, with magnifying of 100X and numerical aperture of 1.3 in oil. The laser Cobolt Blues at 473 nm with average power of 50 mW was used as the light source. Details of methodology and instrumentation were already described in section 2.3.3 of Chapter 1.

Data analysis. Wide field single particle tracking was performed on wide field images using a home-written routine in IGOR®. The position of the molecules was determined with 2D Gaussian fitting of the fluorescence spots. An integration time of 38 ms per frame, (26 Hz) was used for all reported WFM experiments. Each movie used a total number of 1000 frames. The step length distributions for different time lags were obtained by calculating the step length distribution for each single-molecule, summation of all these normalized single-molecule distributions and its division by the number of observed spots. This procedure evenly weighted small and long tracks. The step length distributions were fitted by the equation 5:

$$P(r, t_{lag}) = \sum_i \frac{2}{4D_i t_{lag}} \cdot r \cdot \exp\left(-\frac{r^2}{4D_i t_{lag}}\right)$$

Equation 5

According to literature, from the analysis of these distributions it is possible to plot the mean square displacement (MSD) versus different time lags t_{lag} .^{138; 139} The MSD was obtained by using the equation 6.

$$MSD(\Delta t) = \langle (x_{i+n} - x_i)^2 + (y_{i+n})^2 \rangle$$

Equation 6

Where x_i and y_i are the positions of the molecule in the image frame i ($i = 1, 2, 3 \dots$) determined by the 2D Gaussian fitting, and n denotes the frame number with time lapse Δt from frame i . For calculation of the diffusion coefficient D for a 2D trajectory, the MSD was calculated by averaging over independent pairs. Then, $MSD(\Delta t) = 4D\Delta t$. The diffusion coefficient D was determined by the first set of data point in the MSD plot (i.e. initial slope only).

3 RESULTS AND DISCUSSION

3.1 Determination of diffusion coefficient of NCC dispersions

In Chapter 2, NCC was characterized according to their crystallinity index and morphology. As reported, NCC presented a needle-shaped profile and high crystallinity index (70%). The TEM and STED (Figures 14 and 20 from Chapter 2) images confirmed the nanometric size of the NCC fibres.

The type of acid used for hydrolysis can also influence the diffusion properties of NCC suspensions. NCC obtained via sulphuric acidic hydrolysis shows some shear thinning, while NCC obtained via hydrochloric acid hydrolysis shows higher shear thinning behavior.¹⁴⁰

The determination of dynamic properties of NCC was investigated by FCS measurements. The autocorrelation curves provide direct information about the diffusional motion of NCC in aqueous medium. Figure 23 shows the normalized correlation functions of the rhodamine 6G, ATTO-532 and the NCC/ATTO-532. The autocorrelation curves of the reference dye rhodamine 6G and ATTO-532 in aqueous solution showed well-correlated profiles. Both of them presented only one component and the values of corresponding diffusion coefficients are of the same order of magnitude. On the other hand, the aqueous suspension of NCC/ATTO-532 showed two components from the fitting of its autocorrelation curve. The faster component of the NCC/ATTO-532 suspension may be ascribed to the diffusion of the free ATTO-532, which remains in the medium even after the processes of centrifugation and dialysis. The ATTO-532 has a hydrodynamic radius at same magnitude as that of rhodamine 6G, the FCS standard with value of 4.14×10^{-10} (m².s⁻¹). Therefore, the faster diffusion

coefficient of $3.89 \times 10^{-10} \text{ (m}^2 \cdot \text{s}^{-1}\text{)}$ obtained in labelled NCC (see table 2) is related to the free ATTO-532 dye.

On the other hand, the slowest component showed a diffusion coefficient of $2.77 \times 10^{-12} \text{ (m}^2 \cdot \text{s}^{-1}\text{)}$ (see Table 2), which can be attributed to the diffusion of the NCC covalently labelled with ATTO-532.

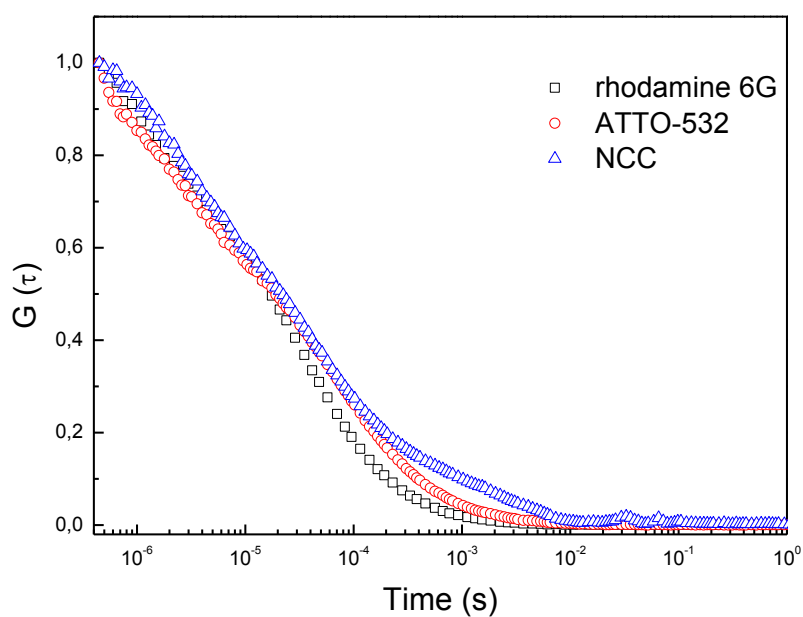


Figure 23. Autocorrelation curves of rhodamine 6G, ATTO-532 and NCC/ATTO-532.

The Table 3 shows the values of diffusion coefficients Dt_1 and Dt_2 of rhodamine 6G, ATTO-532 and NCC/ATTO-532 suspension.

Table 3. Diffusion coefficients Dt_1 and Dt_2 of rhodamine 6G, ATTO-532 and NCC.

Sample	$Dt_1 \times 10^{-10} (\text{m}^2 \cdot \text{s}^{-1})$	$Dt_2 \times 10^{-12} (\text{m}^2 \cdot \text{s}^{-1})$
rhodamine 6G	4.14	
ATTO-532	3.89	
NCC suspension	3.40	2.77

It is possible to determine the diffusion coefficient from the translational motion of a particle in a given solution. The Stokes-Einstein equation is used when the particle is spherical.^{141; 142}

$$D = \frac{k_B T}{6\pi\eta r_h}$$

Equation 7

Where η is the viscosity of the solvent, k_B is the Boltzmann constant, T the temperature in Kelvin and r_h is the hydrodynamic radius.

However, the shape of nanocrystalline cellulose (NCC) is considered a prolate. Figure 24 illustrates a prolate particle shape.¹⁴³

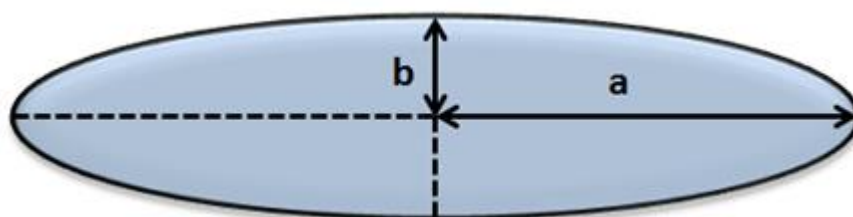


Figure 24. Prolate particle shape, in which b is the semi-minor axis of the structural unit and a is the semi-major axis of the structural unit.

In this case, the Stokes-Einstein equation is modified with the inclusion of the parameter f_s , which is related to the shape of the structural unit. Moreover, the

hydrodynamic radius r_h is replaced by the semi-minor axis of the prolate structure, b .^{144;}

145

$$D = \frac{k_B T f_s}{6\pi\eta b}$$

Equation 8

The shape factor related to the prolate structure is expressed by the following equation.¹⁴⁶

$$f_s = \frac{\ln(\rho + \sqrt{\rho^2 - 1})}{\rho^2 - 1}$$

Equation 9

From eqs. 7 and 8, the ratio of the diffusion coefficients of the dye Atto 532 and NCC particle can be expressed as:

$$\frac{D_{ATTO532}}{D_{NCC}} = \frac{k_B T}{6\pi\eta r_{ATTO532}} \cdot \frac{6\pi\eta b}{k_B T f_s}$$

$$\frac{D_{ATTO532}}{D_{NCC}} = \frac{b}{f_s r_{ATTO532}}$$

Equation 10

The values of $D_{ATTO532}$ and D_{NCC} , previously evaluated by FCS, were 3.40×10^{-10} ($\text{m}^2 \cdot \text{s}^{-1}$) and 2.77×10^{-12} ($\text{m}^2 \cdot \text{s}^{-1}$), respectively. The hydrodynamic radius of the dye ATTO532 obtained from the autocorrelation curve was 4.9×10^{-10} m. Assuming the eq. 9, the value of the parameter f_s corresponds to 0.46 when $\rho^2 \gg 1$, a condition appropriate for NCC particles. When these values are replaced into the eq. 10, we obtain the value of b , which represents the semi-minor axis of a typical NCC fibre.

$$\frac{3.40 \times 10^{-10}}{2.77 \times 10^{-12}} = \frac{b}{0.46 \times 4.9 \times 10^{-10}}$$

$$b = 28 \times 10^{-9} \text{ m} = 28 \text{ nm}$$

Equation 11

This value for the semi-minor axis of the NCC is in agreement with the value of the half cross section of the NCC particle estimated by the STED measurement (see Fig. 21b), in which the diameter was about 50 nm.

3.2 Study of dynamic properties of different composites based on the interaction of NCC/polymer

Rheological parameters of NCC are related to properties such as liquid crystallinity, ordering, and gelation. In diluted suspensions NCC presents shear thinning behaviour, showing concentration dependence at low rates.¹⁴⁷

PEG is an important polymer used in different areas including bio-targeting applications. Moreover, the addition of NCC into polymeric systems could change transport properties such as self-diffusion coefficient and viscosity, thus, revealing important information about how the matrix containing NCC fibres is arranged.

The diffusion features of NCC embedded in different PEG solutions was followed by FCS and WFM measurements. The nanoparticle mobility in solutions of NCC/PEG/water, NCC/PEG/methanol and NCC/PEG/acetonitrile at PEG concentrations of 2%, 5%, 10% and 20% (w/V) were followed by fluorescence correlation spectroscopy (FCS). Figure 25 shows the typical autocorrelation curves of NCC embedded in different PEG/solvent solutions.

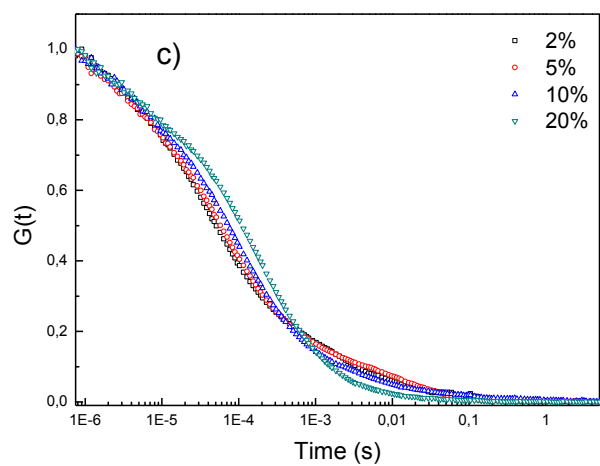
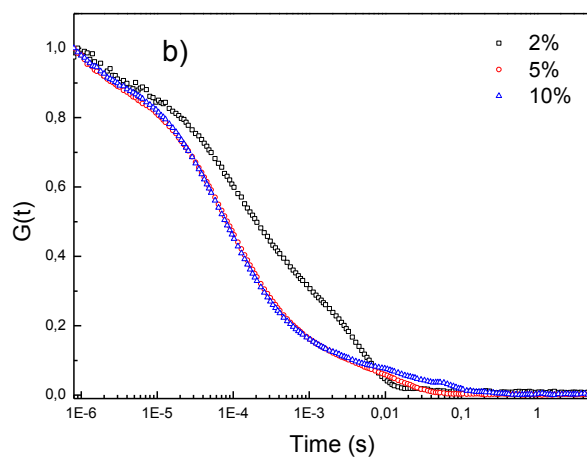
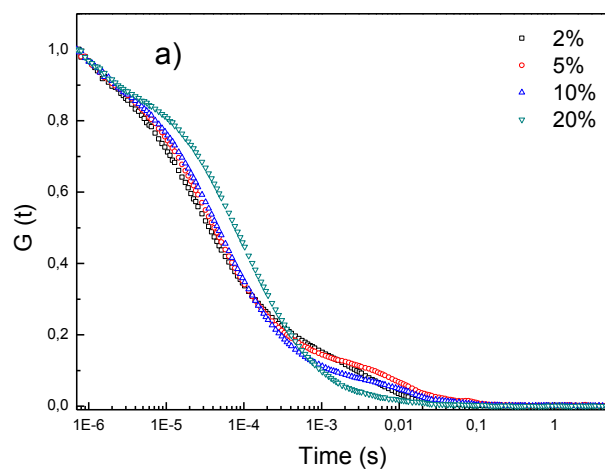


Figure 25. Autocorrelation curves of a) NCC/PEG/water, b) NCC/PEG/methanol and c) NCC/PEG/acetonitrile at the PEG concentration of 2%, 5%, 10% and 20%.

All polymer solutions showed a shift in autocorrelation curves upon increasing the amount of PEG, which represents a decrease of the diffusion of NCC/ATTO-532 and free ATTO-532, regardless of the solvent used. From the autocorrelation curves is also possible to extract the contribution of each diffusion component. Figure 26 shows the changes of the fraction and diffusion coefficient of the NCC/ ATTO-532 and free ATTO-532 in function of PEG content. The fraction of the NCC and ATTO-532 components are respectively 0.517 and 0.483. The increase of PEG concentration reduces the contribution attributed to NCC diffusion and, consequently, amplifies the fraction of ATTO-532 in the diffusion. This behaviour may be ascribed to the decrease in Dt of NCC to slower values, indicating that mobility of the fibre is hindered by the PEG long-range interactions.

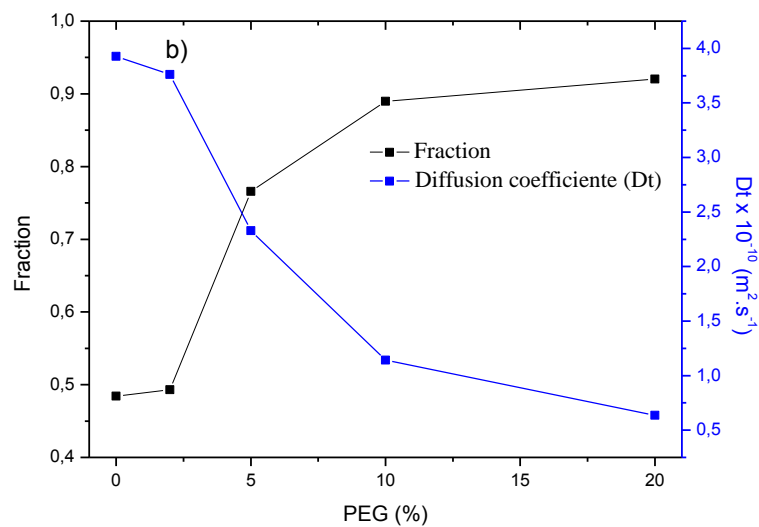
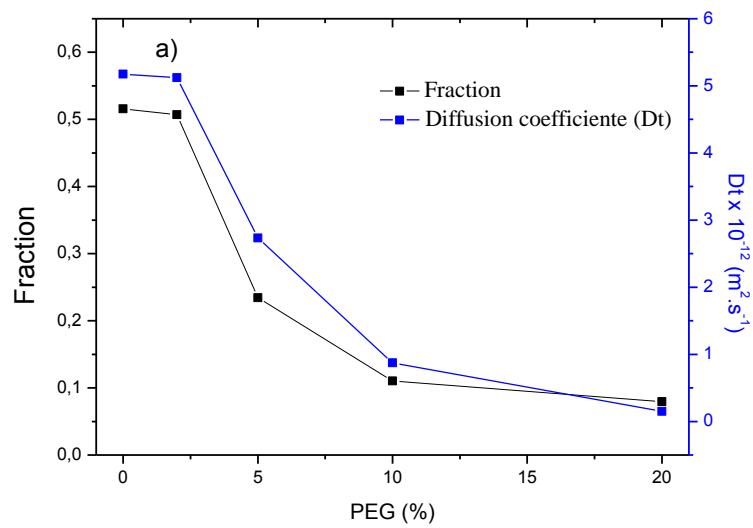


Figure 26. a) NCC fraction and diffusion coefficient (Dt) in function of PEG content. b) ATTO-532 fraction and diffusion coefficient (Dt) in function of PEG content.

The monitoring of dynamic properties of NCC/PEG/water, NCC/PEG/methanol and NCC/PEG/acetonitrile at the PEG concentration of 50% and 70% was performed by WFM measurements. Diffusion coefficients of single particle were determined by step length analysis, and the distributions plotted and fitted by log-Gaussian functions with

their maximum defined as the average diffusion coefficient. In Figure 27 are shown the step-length distributions and the covered trajectories of the water, methanol and acetonitrile NCC/PEG based systems.

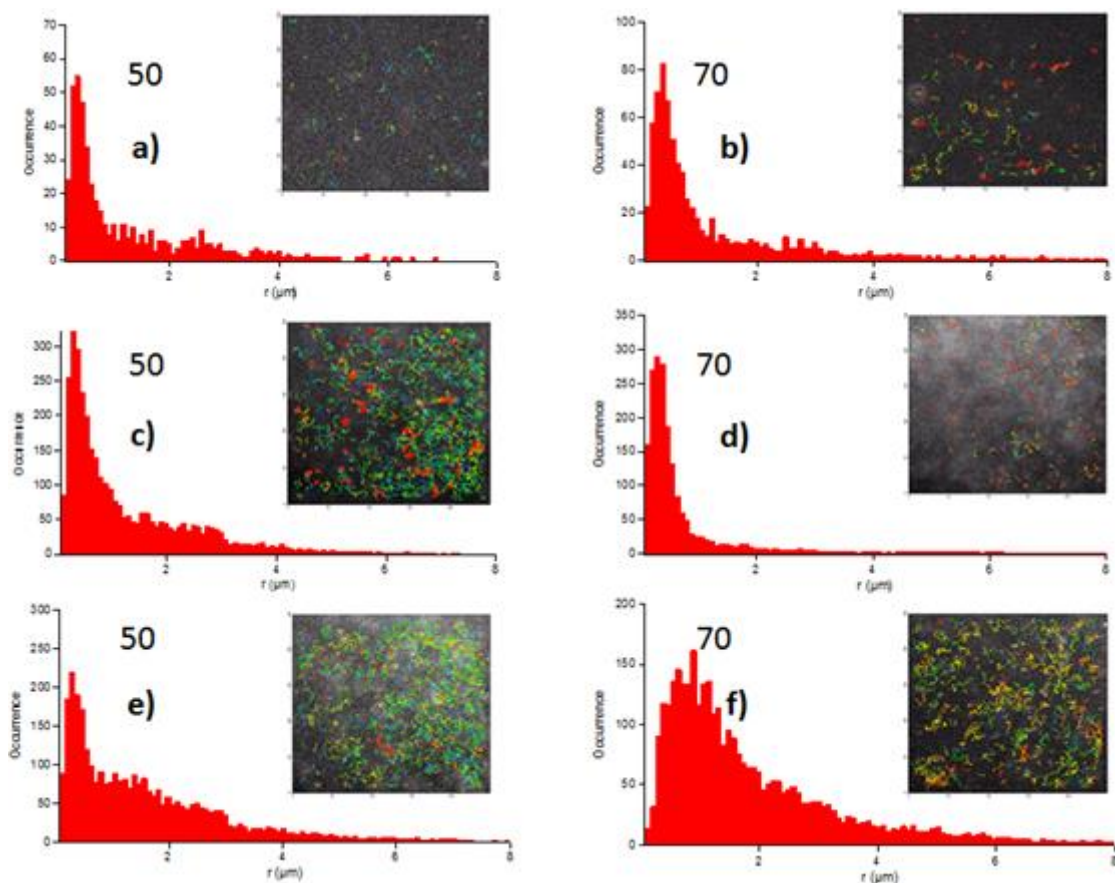


Figure 27. Step-length distribution for a) NCC/PEG (50%)/water; b) NCC/PEG (70%)/water; c) NCC/PEG (50%)/methanol; d) NCC/PEG (70%)/methanol; e) NCC/PEG (50%)/acetonitrile and f) NCC/PEG (70%)/acetonitrile. Single particle trajectories in a representative area are shown in the insets.

Heterogeneities in the translational motion of polymer matrices are observed when molecules or particles have different velocities. Moreover, the motion of a single molecule can be dynamically heterogeneous when, for instance, there is a change in its surroundings, which significantly fluctuates the velocity over the time.¹⁴⁸ Analysing all the three systems one can note the existence of at least two Gaussian distribution curves

related to the solutions containing 50% of PEG, independently of the solvent used. In the measurements of translational diffusion, spatial heterogeneities attributed to two different components could be detected, within our observation time. However, for most molecules no significant dynamic heterogeneities could be observed. The first peak (NCC/PEG(50%)/water, NCC/PEG(50%)/methanol) and NCC/PEG(50%)/acetonitrile) is related to the occurrence of translational movement that covers a small area for a certain period of time. Generally, large particles moving in a viscous polymeric matrix shows such behaviour. Furthermore, this peak has a narrow distribution and high number of occurrence, indicating large particle motion concentrated in small areas. Because of all of these features, the first peak is ascribed to the NCC fibre movements into the polymeric matrices with some degree of hindering. The second peak (NCC/PEG(50%)/water, NCC/PEG(50%)/methanol) and NCC/PEG(50%)/acetonitrile) is attributed to the free ATTO-532 and has broad distribution and lower number of occurrence. Systems with 70% of PEG based on water and methanol showed the occurrence of a narrow distribution related to the NCC movement, while the number of occurrences related to free ATTO-532 decreases to smaller values, nearly disappearing. The system NCC/PEG (70%)/Acetonitrile showed a broadening of the distribution curve related to the NCC movement and decreasing the number of the occurrence. Whereas, the curve distribution attributed to the free ATTO-532 diffusion, virtually disappeared.

For the purpose of evaluation of the changes in translational diffusion motion of the polymer and the NCC, the mean square displacements were plotted as a function of time lag, for all the systems. Figure 28 shows the data of MSD obtained using WFM measurements.

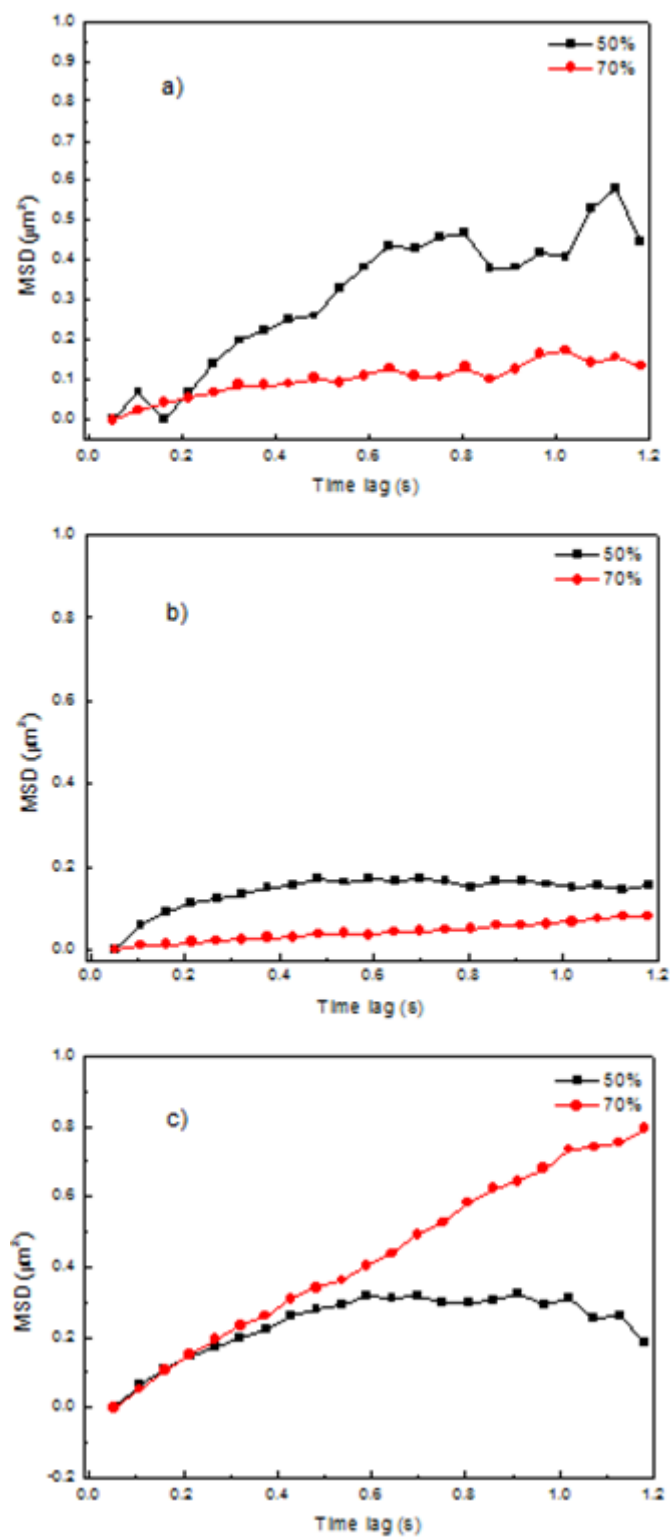


Figure 28. Mean square displacement (MSD) for a) NCC/PEG/water; b) NCC/PEG/methanol and c) NCC/PEG/acetonitrile.

Each system showed a different MSD behaviour as a function of the PEG amount. The system based on NCC/PEG/water presented a decrease in the evolution of the MSD values to 70% of PEG when compared to the system containing 50% of PEG. The system based on NCC/PEG/methanol also presented a decrease in the evolution of the MSD to 70% of PEG. However, the values exhibited were considerably lower, when compared to the system composed by water. On the other hand, the system based on NCC/PEG/acetonitrile showed a different behaviour. The evolution of the MSD showed values higher to the system containing 70% of PEG than the system containing 50% of PEG. The value of the MSD of NCC/PEG (70%)/acetonitrile at 1.18 s was $0.79 \mu\text{m}^2$ while at the same point the system NCC/PEG (50%)/acetonitrile showed the value of $0.19 \mu\text{m}^2$. The diffusion coefficients as a function of PEG amount, obtained from FCS and WFM measurements are shown in Figure 29. As PEG is added, the diffusion coefficient becomes slower, independently of the solvent. Such feature may be related to the fact that the intrinsic viscosity and inter particle interactions mediated by PEG association have the predominant role in the determination of the translational movement. However, the NCC/PEG/acetonitrile showed a slightly different behaviour, in which the change of the diffusion coefficient as a function of PEG amount does not follow a regular pattern. This sort of behaviour can be correlated to how NCC fibres, which have more affinity for hydrophilic solvents to disperse, diffuse in an environment containing acetonitrile, which is a solvent with polar aprotic character differing from water and methanol able to form H-bonding with PEG and OH groups of NCC fibre.

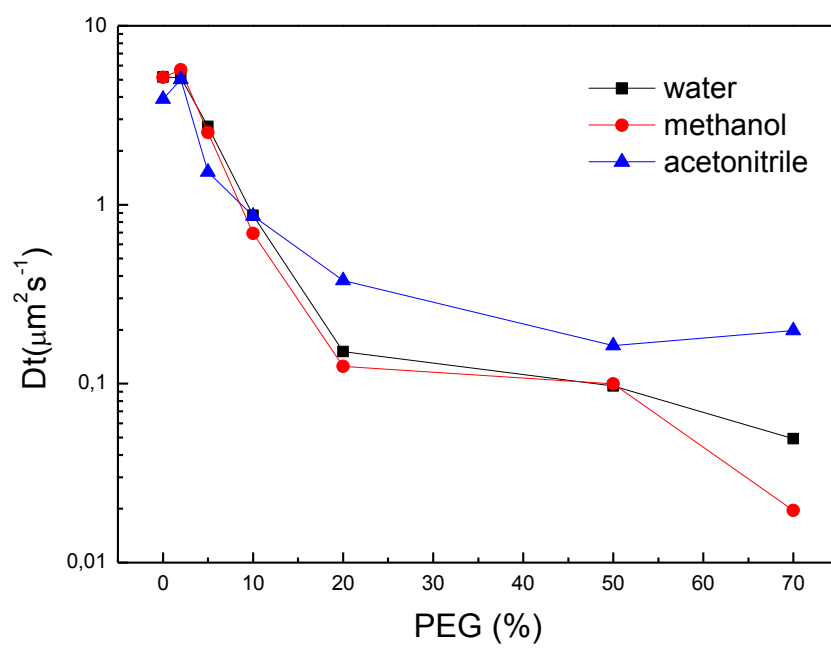


Figure 29. Diffusion coefficient of NCC as a function of PEG content (%).

4 CONCLUSIONS

Aiming at the covalent labelling of the surface of NCC, an aqueous phase click chemistry reaction was applied to perform the fluorophore coupling onto an azide functionalized NCC surface. Dynamic properties of NCC were investigated by FCS measurements. The autocorrelation curves provided direct information about the diffusional motion of NCC in aqueous medium. The aqueous suspension of NCC/ATTO-532 showed 2 components from the fitting of its autocorrelation curve. The faster component of the NCC/ATTO-532 suspension is ascribed to the diffusion of the free ATTO-532, that remained in the solvent even after sample purification by centrifugation and dialysis. The free ATTO-532 in solution has a faster diffusion coefficient of $3.89 \times 10^{-10} \text{ (m}^2\cdot\text{s}^{-1}\text{)}$ similar to the value observed for rhodamine 6G of $4.14 \times 10^{-10} \text{ (m}^2\cdot\text{s}^{-1}\text{)}$. The slowest component registered in the autocorrelation plot indicated a diffusion coefficient of $2.77 \times 10^{-12} \text{ (m}^2\cdot\text{s}^{-1}\text{)}$ that is attributed to the diffusion of the NCC labelled with ATTO-532. The properties related to dynamic properties of NCC/PEG/water, NCC/PEG/methanol and NCC/PEG/acetonitrile were evaluated by FCS and WFM. The diffusion of NCC fibre in solution becomes slower upon addition of PEG, independently of the solvent used. This fact may be related to H-bonding interaction mediated by PEG and the OH groups in the NCC surface obstructing somewhat the free diffusion of the particle.

CHAPTER 4

POLYMERIZATION OF STYRENE

ABSTRACT

Investigation of diffusion properties of polymer systems plays a crucial role in the understanding of rheological parameters, and consequently in polymer processing and assembly of plastics, films, and fibres. In recent years, several groups have studied polymerization processes at the single molecule level using fluorescent molecules as probes. However, this method is an indirect way to monitor diffusion during polymeric formation. Here we used FCS and WFM to follow changes in the diffusion coefficients of growing polymer chains during a controlled radical polymerization process. Linear and star-shaped polystyrene were grown via nitroxide-mediated polymerization (NMP) from alkoxyamine-based initiators already containing a highly fluorescent perylene diimide moiety covalently attached, which was the key improvement of this work. FCS and WFM methods enabled us to demonstrate the development of heterogeneities in the chain movement. The polymerization mediated by monofunctional initiator showed slower monomer conversion as compared to the formation of star-shaped polymers from a tetrafunctional initiator. Whereas the formation of star-shaped polystyrene shows a narrow step-length distribution and low mean square displacement (MSD) values ($0.055 \mu\text{m}^2$ at 0.8 s) after 180 minutes of reaction, contrasting with linear polystyrene where a broad step-length distribution, similar monomer conversion and MSD values were observed. Therefore, variation of viscosity during the polymerization represents the major effect for the evaluation of diffusion parameters. This study demonstrates that direct investigation of heterogeneity emerging during a controlled radical polymerization process by means of fluorescence of single-molecule chain initiator allows unravelling information about the growing polymer chain.

1 INTRODUCTION

Free uncontrolled radical polymerization is one of the most used processes for obtaining of vinyl polymers. The capacity of the radical species to interact with different functional groups of the monomer together with the possibility of carrying out the reaction in protic solvents account for widespread application of the method. However, there are key restrictions involving the occurrence of irreversible bimolecular reaction among propagating radicals, which make impossible the generation of well-defined polymers. In order to overcome this substantial limitation, it was developed the controlled radical polymerization (CRP), which involves species able to deactivate radical chains and consequently decrease the irreversible termination reactions.¹⁴⁹⁻¹⁶¹ The obtained equilibrium related to the controlled radical polymerization is shown in Figure 30. The synthesis of polymers with controlled molecular weight, narrow molecular weight distribution and different topologies was possible due to fact of a most part of “dormant” chains are in equilibrium with a small amount of active ones. Among the most studied CRP techniques are nitroxide-mediated radical polymerization (NMP),^{151; 159; 162; 163} atom transfer radical polymerization (ATRP),^{160; 164} radical addition-fragmentation chain transfer (RAFT),¹⁶⁵⁻⁶⁷ degenerative chain transfer polymerization (DCTP)^{168; 169} and organometallic-mediated radical polymerization (OMRP).¹⁷⁰⁻¹⁷² NMP is based on equilibrium between a propagating radicals and nitroxide species, which are considered as control agent, yielding alkoxyamine as preponderant species.

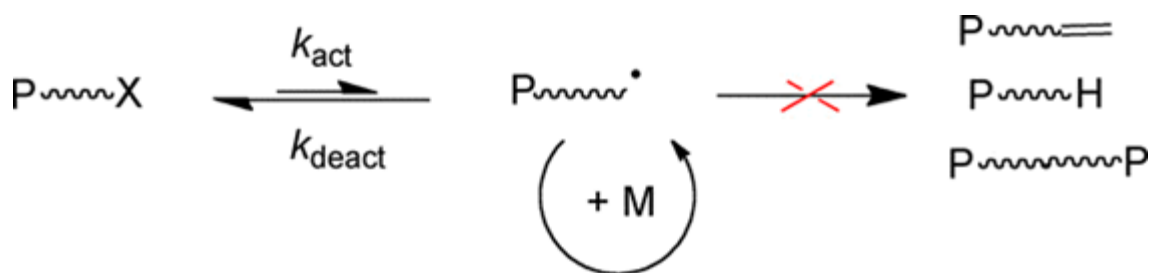


Figure 30. General concept of controlled/living radical polymerization (CRP).¹⁶³

By the use of a dormant species, it is possible to generate back propagating radical and the nitroxide upon temperature increase. The equilibrium involving dormant and active species is known as activation-deactivation process, shown in Figure 31. This equilibrium only depends on the temperature, thus, neither catalyst nor bimolecular exchange are prerequisites. The polymerization kinetics is ruled by both activation–deactivation equilibrium ($K = k_d/k_c$, the activation–deactivation equilibrium constant) and the persistent radical effect (PRE).¹⁷³ The $[\text{nitroxide}]_0/[\text{initiator}]_0$ ratio is very important because the kinetics of the polymerization is controlled by the amount of nitroxide present after the initiation step. When there is excess of free nitroxide the activation–deactivation equilibrium is shifted toward the formation of dormant species, decreasing the polymerization rate. The efficiency of thermal initiators is compromised by the cage effect and induced decomposition besides occurrence of rearrangement or fragmentation reactions.

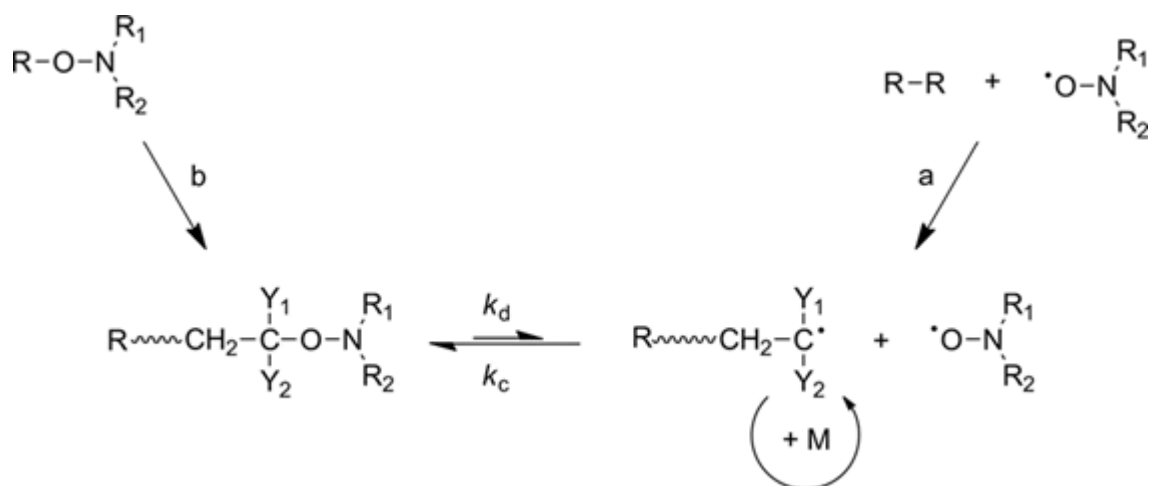


Figure 31. Activation–deactivation equilibrium in nitroxide-mediated polymerization. Bicomponent initiating system (a) and monocomponent initiating system (b).¹⁶³

The use of NMP has received significant attention in the production of both linear and star-shaped polymer. Polymers with star structures have desirable properties, which are related to its arrangements. Star-shaped polymer show a more compact structure comparing to its analogous linear structures because of high segment density, which extremely affects crystalline, mechanical, and viscoelastic properties.

Diffusion properties have an important role in questions related to the characteristics of the polymeric systems. Molecular mass distribution, polydispersity index and gel effect (Trommsdorff effect) are parameters related to the quality of the polymer and connected to kinetic processes.¹⁷⁴⁻¹⁷⁶ Different conventional techniques have been employed to investigate polymeric structures along the years, among which may highlight electron paramagnetic resonance spectroscopy,¹⁷⁷ gel permeation chromatography and mass spectrometry,¹⁷⁸ as well as NMR¹⁷⁹ and fluorescence spectroscopy.^{180; 181}

2 EXPERIMENTAL

2.1 Polymerization of styrene

Styrene (1) and the monofunctional, non-fluorescent initiator *N*-tert-butyl-*N*-(2-methyl-1-phenylpropyl)-*O*-(1-phenylethyl) hydroxylamine (2) were purchased from Sigma-Aldrich. Styrene was distilled under reduced pressure before use, and its purity was checked by H-NMR. The synthesis of monofunctional fluorescent initiator (3), tetrafunctional fluorescent initiator (4) and the tetrafunctional non-fluorescent initiator (5) (Figure 27) were performed by Daniel Jäsch from Max Planck Institute for Polymer Research – Germany. The structures are shown in Figure 32.

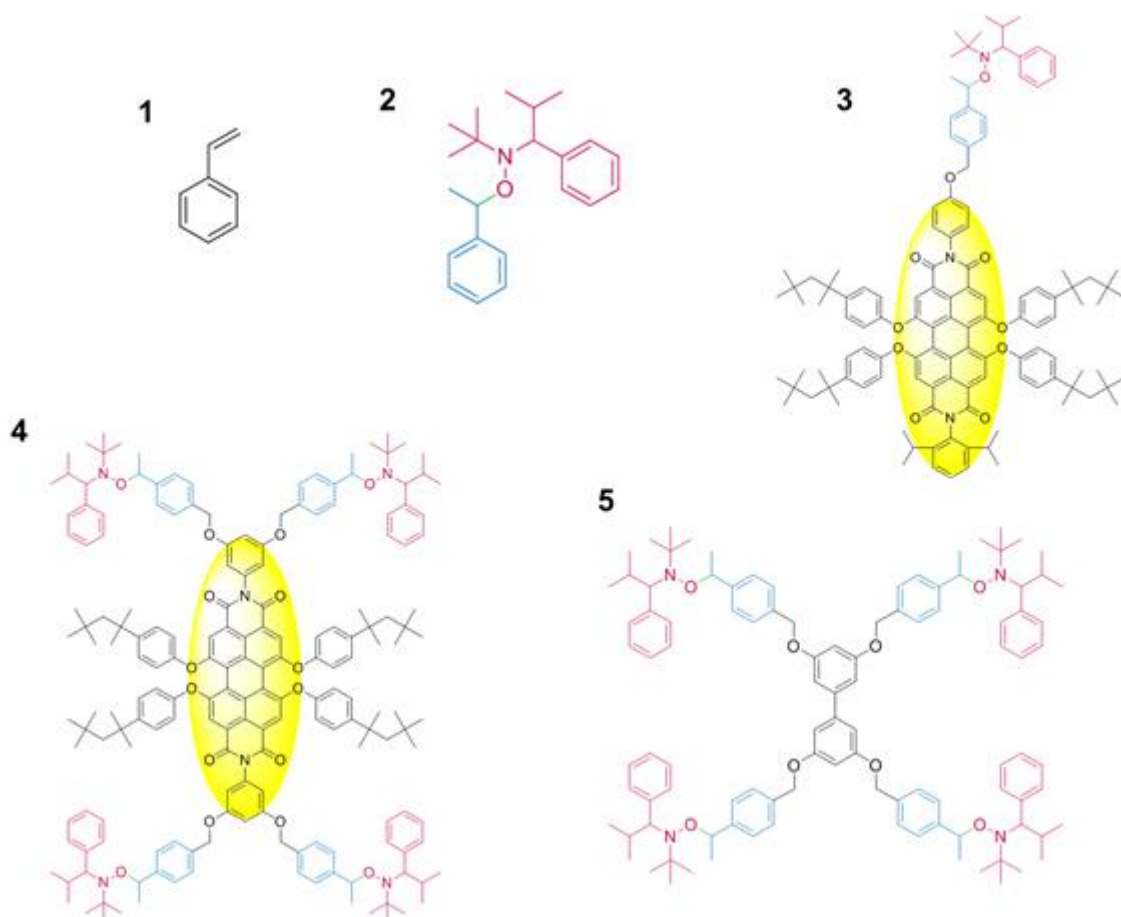


Figure 32. Structures of styrene (1) and of the alkoxyamine-based NMP initiators used in this work (2 and 5: non-fluorescent initiators; 3 and 4: fluorescent initiators).

2.2 Polymerization process

After the reaction mixture is prepared by the direct dissolution of the initiators in the styrene, it was kept in the sample holder under argon flow for 20 minutes, aiming at the obtaining of an inert atmosphere. Afterwards, the process of increase of the temperature started. All polymerizations were carried out at 128°C under an inert atmosphere of argon, in a sealed sample holder (Figure 33). The styrene/initiator ratio was 80/1 for polymerizations initiated with monofunctional 2 and 3, and 240/1 for polymerizations mediated by tetra functional 4 and 5. To enable the single-molecule study of the polymerizing mixtures by FCS and WFM, a minimal amount of fluorescent initiator (10^{-9} mol / L) was dissolved in an appropriate amount of styrene, together with non-fluorescent initiator. Monomer conversion was monitored by Raman spectroscopy. By autocorrelation analysis obtained from FCS and single-particle tracking (SPT) from WFM enabled us to directly obtain values of dynamic parameters as a function of growth of the polymeric chains.

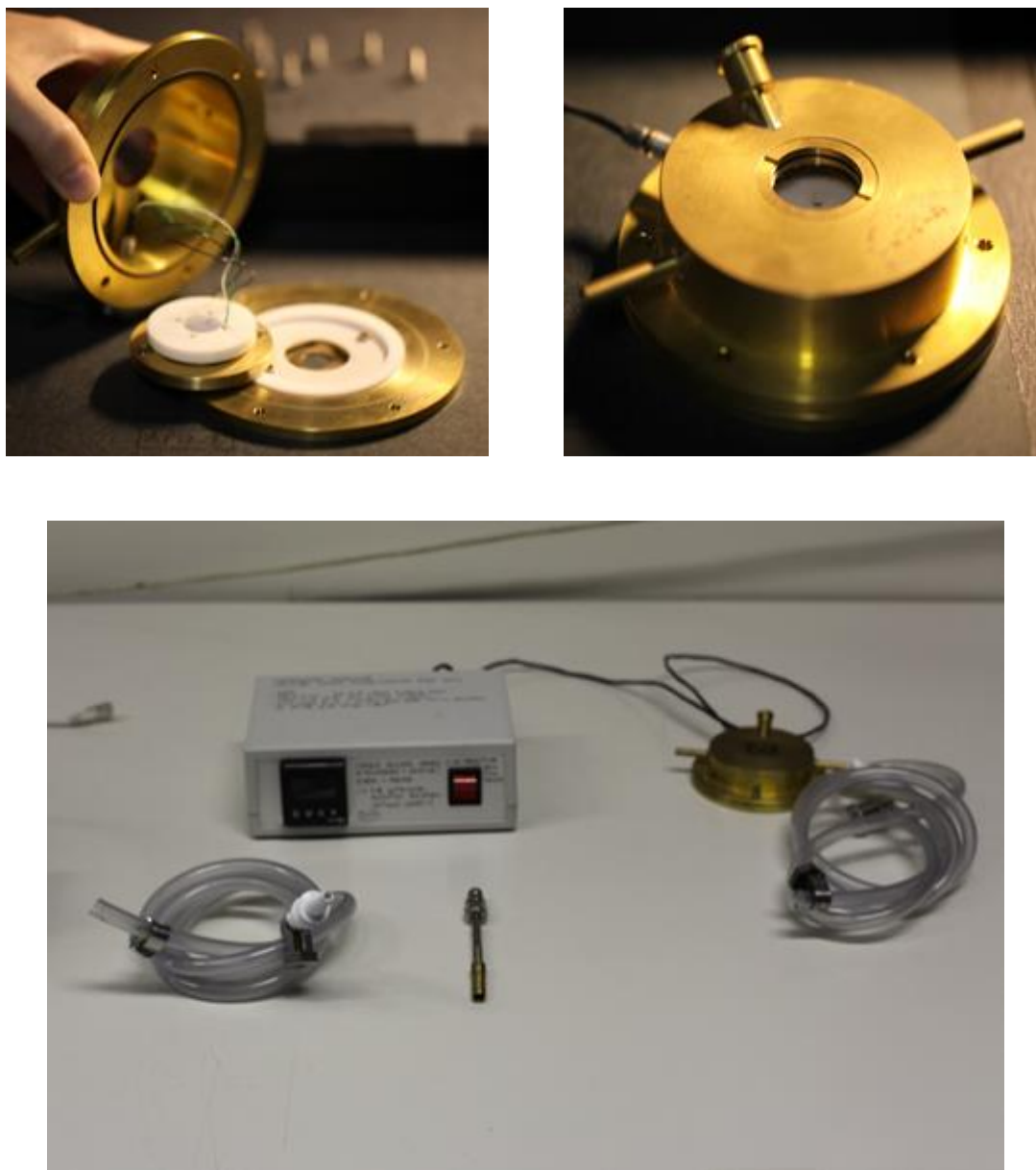


Figure 33. Sample holder device.

Three different sets of polymerization experiments were performed:

- System 1: styrene (1) + initiator (2: linear) + fluorescent initiator (3: linear);
- System 2: styrene (1) + initiator (5: star) + fluorescent initiator (4: star);
- System 3: styrene (1) + initiator (2: linear) + fluorescent initiator (4: star).

In order to perform FCS, WFM and Raman measurements, the reaction was paused after 0, 30, 60, 120, 180 and 240 minutes. To stop the polymerization, the sample holder containing the reaction mixture was cooled down to 25 °C. The sample holder was designed specifically to perform the polymerization as well as the measurements under an inert argon atmosphere, without exposure to air. Around 30 minutes were spent to perform the FCS/WFM and Raman measurements, and then re-initiate the polymerization process. The same methodology was followed for all steps of the polymerization, including the three systems investigated.

2.3 Measurements

FCS and WFM measurements related to the investigation of styrene polymerization were performed in the Laboratory for Photochemistry and Spectroscopy of KU Leuven, Belgium. The schematic setup of the FCS and WFM is illustrated in Figure 34.

2.3.1 GPC

Gel permeation chromatography (GPC) was performed with a Shimadzu apparatus (UV and RI detection) with a PLgel D column (Polymer Laboratories) and dichloromethane as the eluent at 30 °C calibrated with linear polystyrene standards. UV-vis absorption spectra were recorded on a Perkin Elmer Lambda 40 UV-vis spectrophotometer.

2.3.2 Raman

In order to track *on-line* the evolution of conversion during suspension polymerization reactions, Raman spectra were collected in a FRA 106/S FT-Raman accessory coupled to a Bruker IFS 28/N spectrometer, equipped with a quartz beam splitter. The spectral range comprises equally spaced measurements from 100 to 4000 cm^{-1} with a resolution of 8 cm^{-1} and the laser wavelength and power were 1064 nm and 450 mW, respectively.

During styrene suspension polymerization reactions, spectra were collected with 32 scans

2.3.3 FCS

A Spectra-Physics CW Excelsior 532 nm laser (with an output power of 500 mW) was used to generate a laser beam with an approximately Gaussian shape. The source light passed through a sequence of lenses and filters, attenuating its power to 150 μ W. Afterwards the laser beam passed into an optical microscope (Olympus IX71) equipped with a 100 \times oil-immersion objective (N.A. 1.30). The laser light was focused 7 μ m above surface of the glass slide that made up the bottom part of the sample holder. The fluorescence signal was collected by the same objective and passed through a 50 μ m pinhole. The scattered excitation light was removed by a dichroic mirror (z532rdc, Chroma) localized in front of the pinhole. An avalanche photodiode detector (APD – PicoQuant τ -SPAD) was used to collect the fluorescence signal. For each measurement, photons were collected for about 3 minutes. Each photon event was recorded using a time stamp with picosecond precision using a HydraHarp 400 (PicoQuant, Berlin) in T2 mode. Autocorrelation events were calculated by the SymPhoTime software (PicoQuant). The shape and size of the confocal volume was estimated using an aqueous solution of Rhodamine 6G, which has a known diffusion coefficient of $4.14 \times 10^{-10} \text{ m}^2 \text{ s}^{-1}$ in water at 25 $^{\circ}\text{C}$.

2.3.4 WFM

For the WFM measurements the same Spectra-Physics CW Excelsior 532 nm laser was used as for the FCS measurements. The light was passed through $\lambda/2$ and $\lambda/4$ wave plates to obtain a circularly polarized beam. Afterwards, it was expanded and passed through a pre-focus ('wide-field') lens. Then, the light was guided into the 100 \times oil-

immersion objective (NA. 1.30). The fluorescence light was collected by the same objective, separated from the excitation light by a dichroic mirror (z532rdc), further magnified by a projection lens and then projected onto the active area of a Roper Scientific Cascade 512B EM-CCD camera. The images had a resolution of 48.08 nm per pixel. For each measurement 800 frames were recorded.

Details of methodology of the analysis data related to MSD and step-length distribution is already described in section 2.6 of Chapter 3.

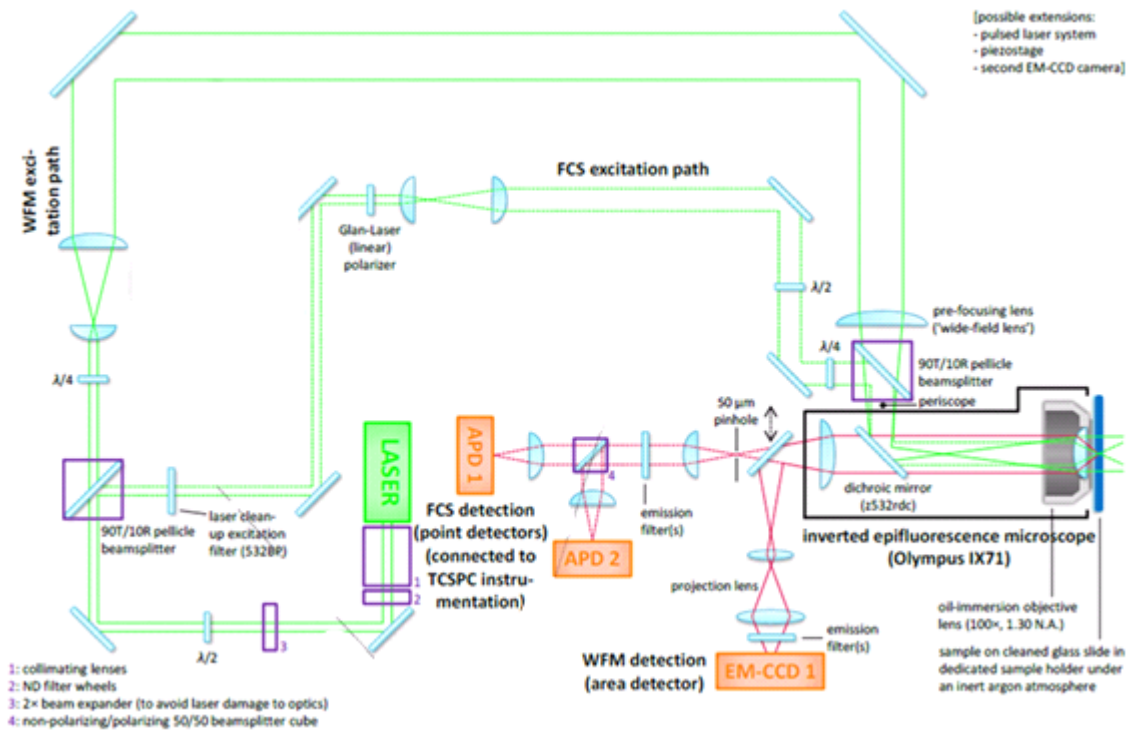


Figure 34. Schematic setup of the FCS and WFM (KU Leuven).

3 RESULTS AND DISCUSSION

3.1 Styrene nitroxide mediated polymerization

Previous studies carried out in the Molecular Imaging and Photonics – Departement Chemie KU Leuven by Wöll and co-authors presented a way to follow radical polymerization of styrene over an extensive conversion range. The method was based on the detection of the diffusion of single free dye molecules and the fact that their mobility changes during the polymerization. Due to the formation of network occurred during the increase of the polymer chains heterogeneities in the motion were verified.¹⁷⁴ In the work presented in this chapter the investigation of the linear and star-shaped polymerization systems was possible by following heterogeneities in molecular motion in which an infinitesimal amount of the initiator used in the polymerization process contained a dye (perylene diimide) attached to its chain. Thus, the diffusion movement monitored was intricately linked to the polymeric chains.

The structure of polymeric systems 1 and 3 were based on matrices generated using polymerization mediated by the linear nitroxide initiator. Whereas system 1 shows its fluorescent fraction of polymerization promoted by the initiator 3, system 2 shows its fluorescent fraction composed by the star-shaped initiator 4. On the other hand, the matrix of the polymeric system 2 has been obtained using polymerization mediated by the star-shaped nitroxide initiator and its fluorescent fraction is composed by the star-shaped initiator 4.

Raman spectroscopy is a proper method to monitor polymerizations of vinyl monomers, by measuring the strong Raman band corresponding to the C=C double bond, which disappears during the polymerization reaction, as shown in Figure 35. Monomer-to-polymer conversions were calculated by the ratio of intensities between the C=C-

stretching vibration at 1600 cm^{-1} and a ring vibrational mode at ca. 950 cm^{-1} . For that, a calibration curve from solutions of well-known concentration was used.

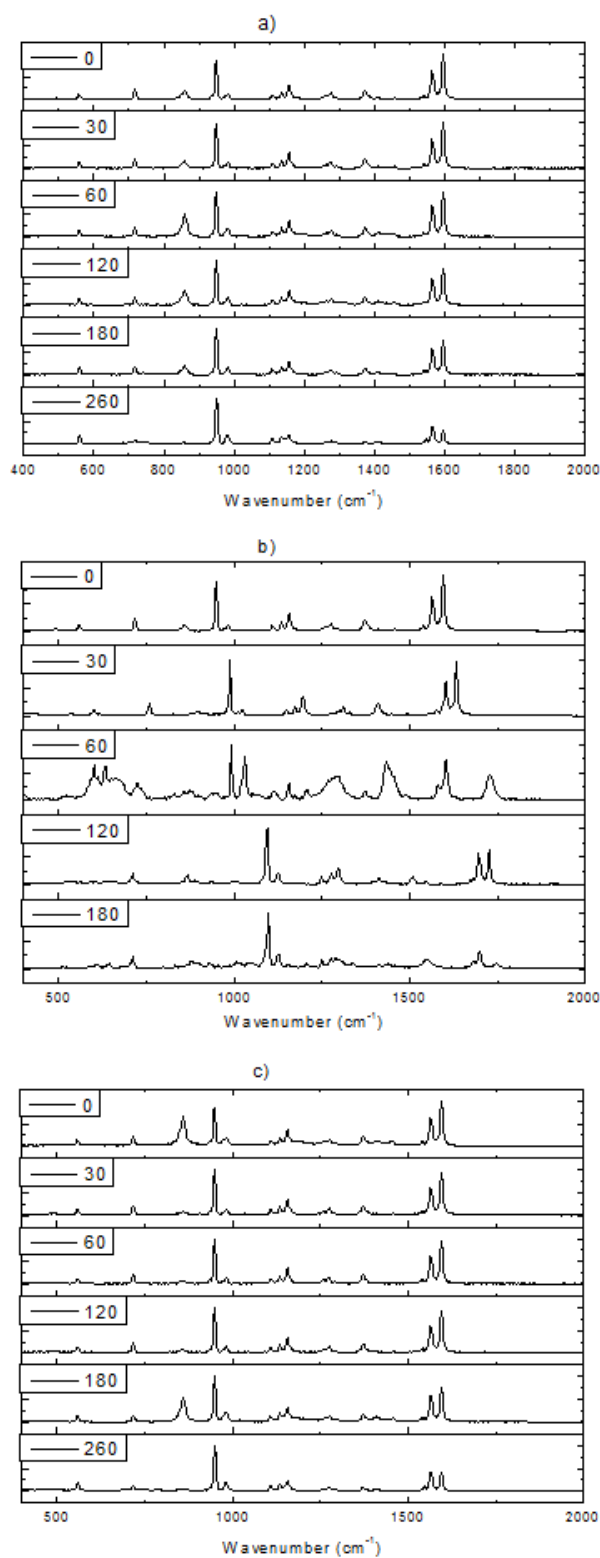


Figure 35. Raman spectra for the polymerization of styrene, mediated by a) System 1, b) System 2 and c) System 3.

Due to the high viscosity of the polymeric reaction medium and therefore the impossibility of continuing the polymerization process, the sample holder containing polystyrene was opened and an aliquot was taken and immediately placed in THF. Then, measurements in GPC were conducted to determine the polydispersity index (PDI) of the samples. Figure 36 shows the GPC trace for the systems 1, 2 and 3, The PDI values for the resulting polymer at each configuration were 1.180; 1.141 and 1.055, respectively.

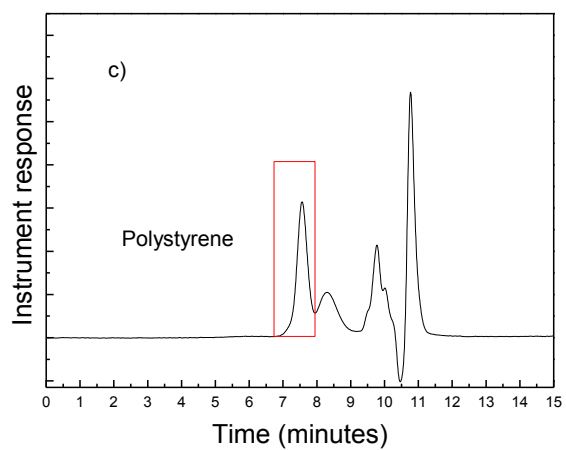
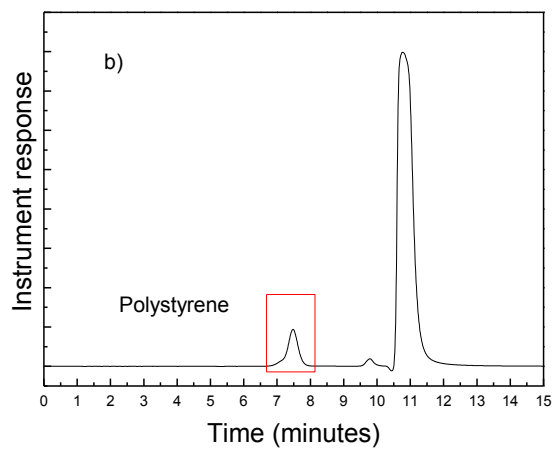
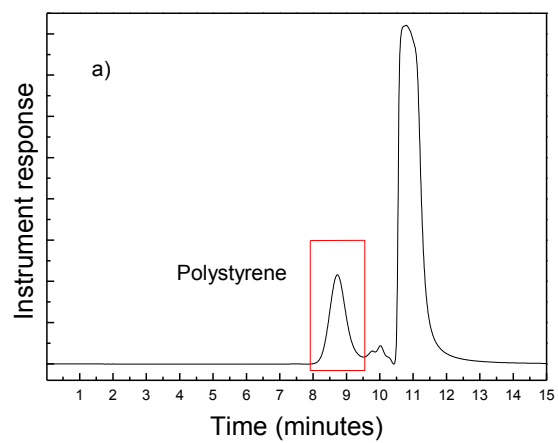


Figure 36. GPC traces of the polystyrene obtained via NMP for the a) System 1, b) System 2 and c) System 3.

The Table 4 shows the values of weight average molecular weight (Mw), number average molecular weight (Mn) and polydispersity index (PDI) for the three different polymerization systems.

Table 4. Weight Average Molecular Weight (Mw), Number Average Molecular Weight (Mn) and Polydispersity index (PDI), related to the system 1, system 2 and system 3.

System	Mw (g.mol ⁻¹)	Mn (g.mol ⁻¹)	PDI
System 1	8,518	7,368	1.156
System 2	18,642	16,662	1.119
System 3	3,490	3,059	1.141

Dynamic properties related to polymerization of styrene by linear and star-shaped initiators were studied by changes in diffusion coefficient during the growth of fluorescent polymeric chain inside the non-fluorescent polymeric chain. Initially, fluorescent correlation spectroscopy (FCS) was the technique used to follow the formation of the polymer. When the polymer diffusion coefficient became slower than $10^{-12} \text{ m}^2\text{s}^{-1}$ the polymer diffusion was too slow to be followed by FCS. Therefore, the measurements were replaced by wide field microscopy (WFM) imaging. By using WFM, it was possible to monitor closely the single polymer chain and, consequently, to track its translational diffusion in the sample. Figure 37 shows the normalized correlation functions related to the System 1, System 2 and System 3.

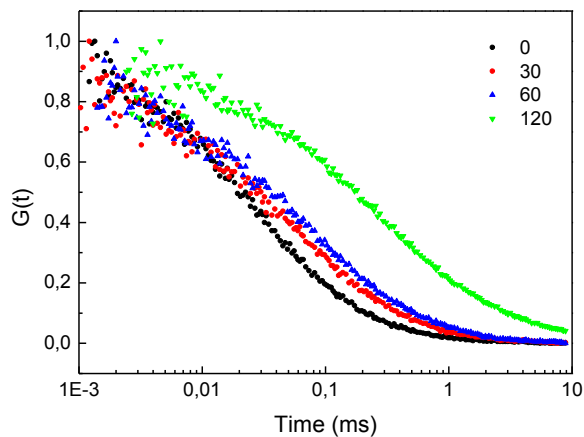
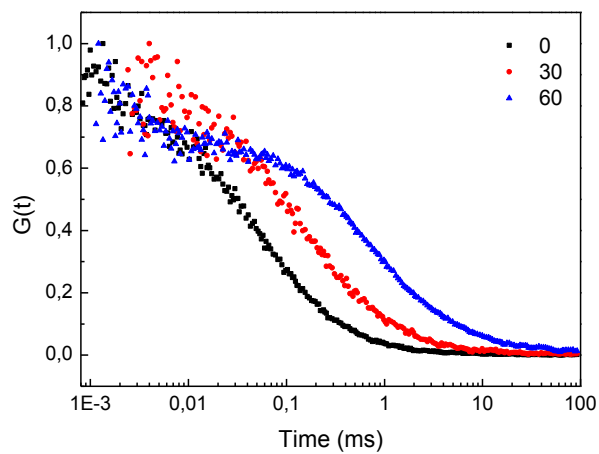
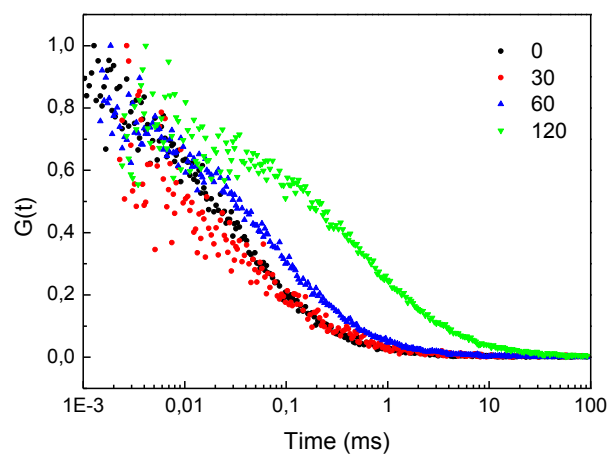


Figure 37. Normalized FCS autocorrelation curves for the polymerization of styrene, mediated by a) System 1, b) System 2 and c) System 3 at different reaction time.

The progress of the monomer conversion as a function of the reaction time for the three systems is shown in Figure 38a). The presence of the respective fluorescent initiators does not have influence on the result, due to the negligible amount used. Therefore, by the evolution of the conversion it is clear that polymerization mediated by star-shaped initiator (system 2) shows the highest conversion rate when compared to the systems 1 and 3. Systems 1 and 2 have very similar behaviour concerning polymer conversion as illustrated in Figure 38a. The highest conversion obtained using star-shaped initiator may be a result of more initiator centres of nitroxide in the locus of polymerization, although styrene/initiator ratio used have been 80/1 for polymerization mediated by monofunctional initiator and 240/1 for polymerizations mediated by tetra functional initiator.

The diffusion coefficients as a function of the reaction time are shown in Figure 38b. System 2 has the lowest initial value for diffusion coefficient, $153.3 \mu\text{m}^2\text{s}^{-1}$, while the values for systems 1 and 3 are respectively $266.2 \mu\text{m}^2\text{s}^{-1}$ and $217.8 \mu\text{m}^2\text{s}^{-1}$. As the polymer conversion is carried out, systems 1 and 3 show similar trend related to the decrease of the polymer diffusion coefficients, whereas system 2, containing star-shaped initiator, demonstrates a faster decrease in its diffusion coefficient.

In Figure 38a is showed the monomer conversion, obtained from GPC measurements, plotted in function of the polymerization time. The diffusion coefficients as a function of styrene conversion, obtained from FCS and WFM measurements are shown in Figure 38b.

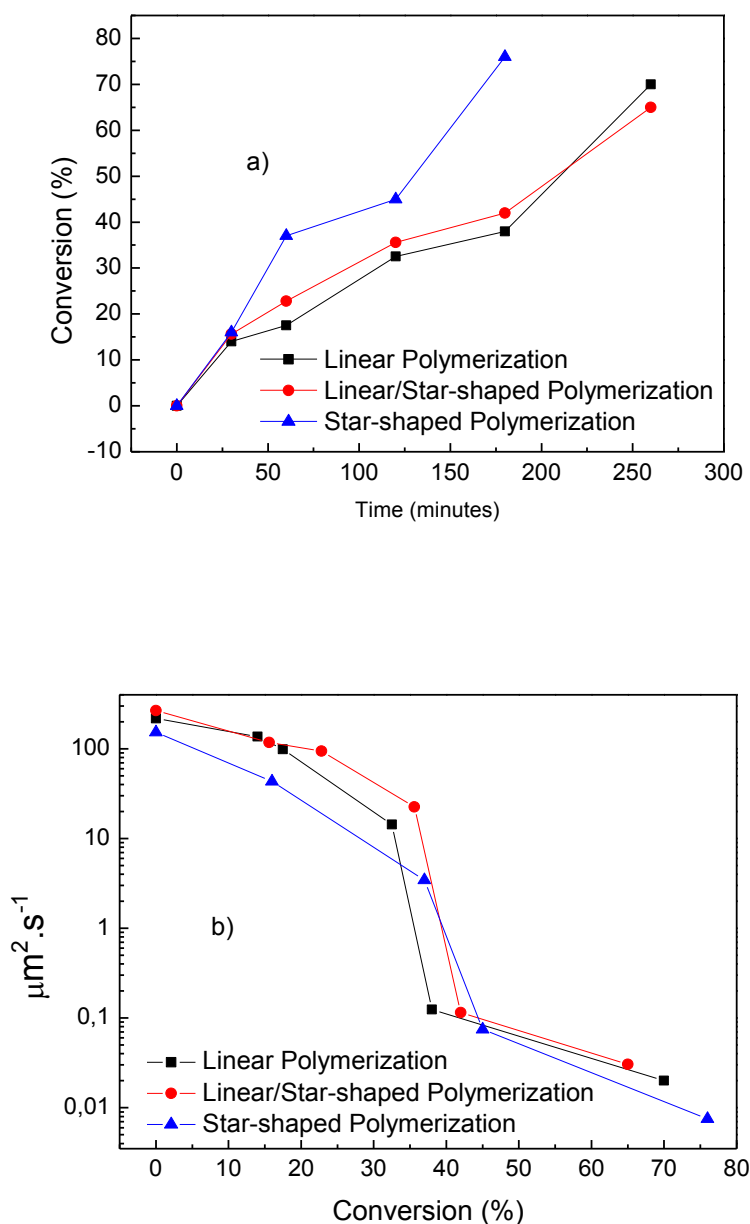


Figure 38. a) Monomer conversion in function of polymerization time. B) Diffusion coefficients plotted versus styrene conversion. Square symbols represent diffusion coefficients related to polymerization mediated by linear initiator (system 1), round symbols represent diffusion coefficients related to polymerization mediated by linear initiator, containing fluorescent star-shaped initiator (system 3), and triangle symbols represent diffusion coefficients related to polymerization mediated by star-shaped initiator system 2).

At early stages of polymerization, the FCS technique was very efficient to follow changes in diffusion coefficient of the polymer systems investigated. However, the

NMP allows polymer chain growing with monomer conversion, reducing the polymer mobility. Thus, FCS was able to study mobility up to diffusion coefficient of $10^{-13} \text{ m}^2 \cdot \text{s}^{-1}$. In slower diffusion coefficients WFM was the technique applied to investigate dynamic properties related to the three different polymerization systems. The positions of polymer chains were determined by two-dimensional Gaussian fitting. The molecules had their location tracked when moving at the focal plane. As mentioned previously, one of the advantages of FCS and WFM is the ability to detect dynamics with spatial resolution, near to the molecular scale without averaging or the necessity of complex models to extract data of interest. For that reason, direct observation of the movement of labelled polymeric chains is obtained, allowing track their mobility and quantify potential heterogeneities related to different pattern of translational diffusion. Nevertheless, the projection and mapping in 2D of a real motion in 3D should provide diffusion constants lightly lower.

In order to analyse the area covered by the diffusion, the step-length distributions of the motion of single polymeric chains were obtained. In Figure 39 are shown histograms and single polymer chain trajectories (in the insets), related to the three polymeric systems, after 180 minutes of reaction. Systems 1 and 3 show close values of conversion, 38% and 42% respectively, which are intimately correlated to range of step-length distribution. Both systems present broad Gaussian spreading, extending from $0.0537 \mu\text{m}$ to $4.215 \mu\text{m}$ for both systems, with peak values at similar positions, $0.590 \mu\text{m}$ to system 1 and $0.674 \mu\text{m}$ to system 3. On the other hand, system 2 shows conversion monomer (76%) and step-length distribution distinct when compared to systems 1 and 3. The polymers formed at this stage show an advanced step of conversion, where star-shaped chain entanglement is almost immobilized, slowing down translation

movements of the labelled polymers. The occurrence number has its Gaussian distribution limited to the narrow range of 3 μm , with the peak located at 0.337 μm .

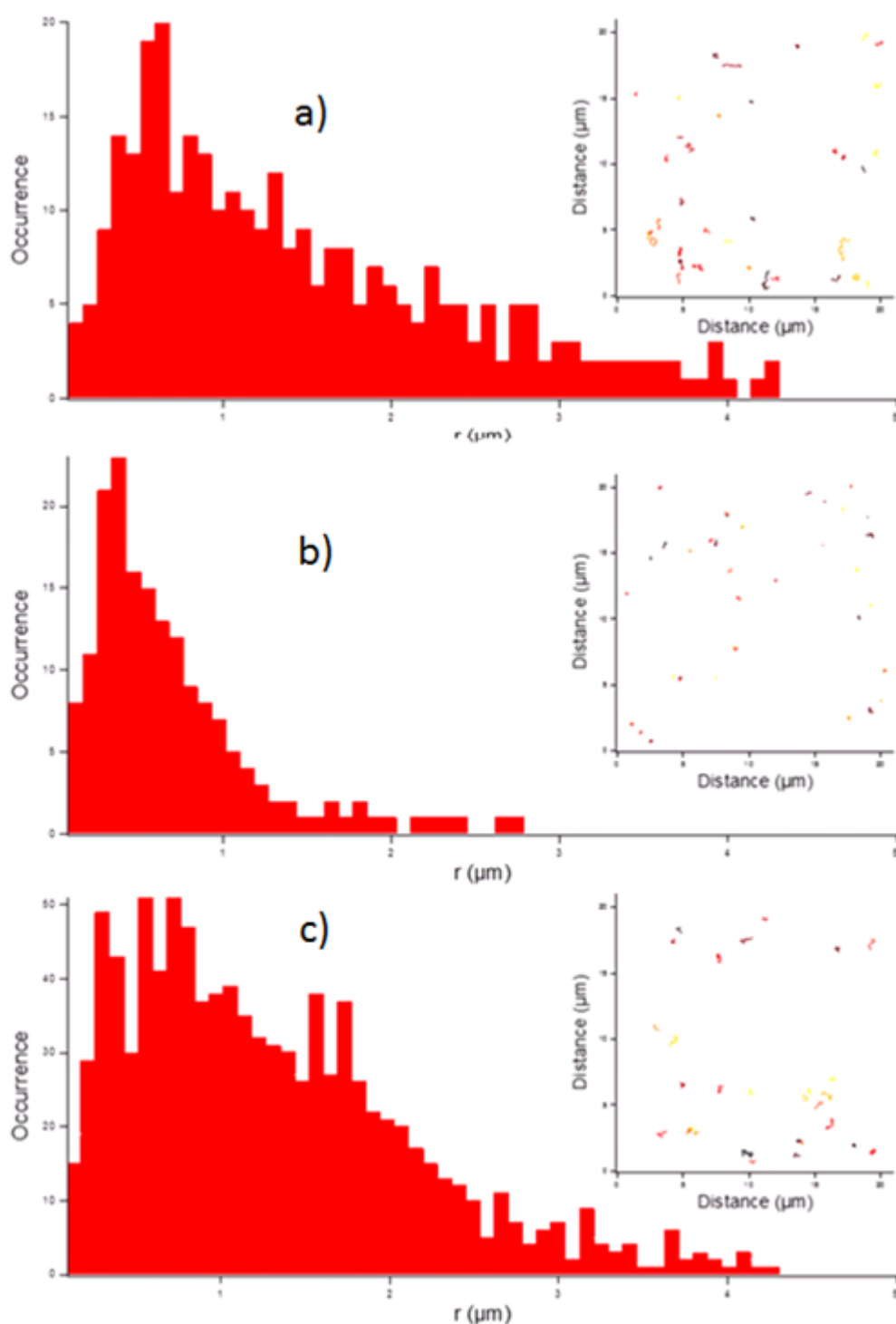


Figure 39. Step-length distribution for a) system 1, b) system 2 and c) system 3. The distributions exhibited are related to polymeric systems after 180 minutes of reaction. Single molecule trajectories in a representative area are shown in the insets.

In order to show the influence of growing network in translational diffusion, the mean square displacements (MSD) were plotted as a function of or against time lag, for all the systems. Figure 40 shows the data of MSD related to the two last steps of polymerization, measured by WFM. The results confirm features previously discussed. Systems 1 and 3 present equivalent evolution of the MSD values, for both steps, 180 and 260 min. While the evolution of the MSD for the System 2 presents low values even at 120 min. For the measurement performed at 180 min, the last one before total immobilization of the polymeric chains shows values close to zero, during all the time lag, wherein after 0.8 s is only $0.055 \mu\text{m}^2$.

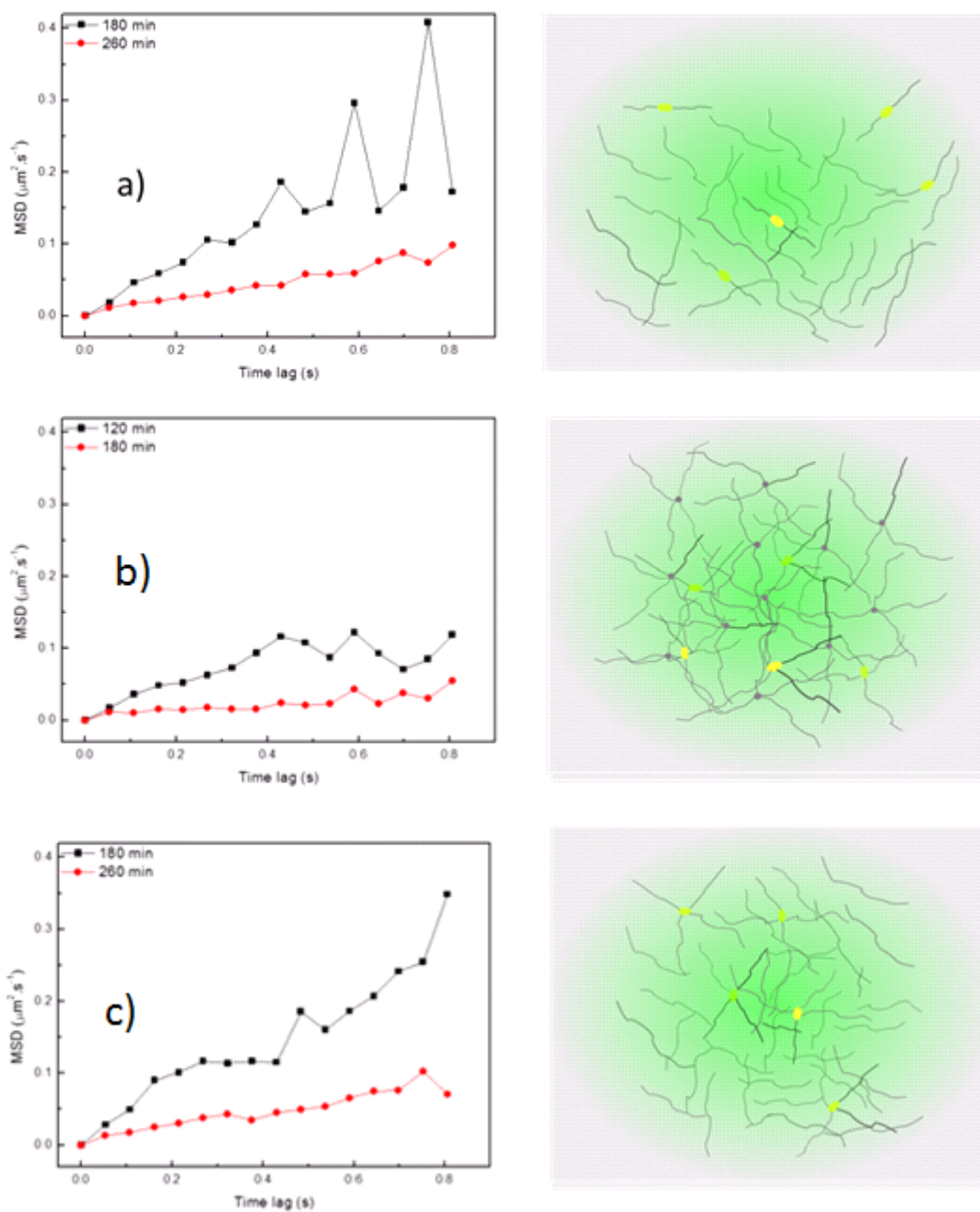


Figure 40. Mean square displacement (MSD) for system 1 (a), system 2 (b) and for system 3 (c). Below of MSD graphs is shown the schematic representation of labelled chain in their surroundings of respective system. Yellow circles shown in some chains represent th the labelling by perylene diimide (PDI*).

4 CONCLUSIONS

In this study, we present a direct method to investigate diffusion parameters of polymerization of styrene mediated by linear and star-shaped nitroxide-based initiators. Our methodology is based on the use of labelled initiators, which produce fluorescent polymers. The growth of probed polymer chains occurs with polymerization at bulk level. The results presented here provide direct measurements of molecular diffusion within a polymeric matrix during their polymerization processes. Systems 1 and 3 show similar development of the diffusion properties. Whereas system 2 shows narrow step-length distribution and low values of MSD ($0.055 \mu\text{m}^2$ after 0.8 s) after 180 min, systems 1 and 3 present close values for all parameters investigated, including broad range of step-length distribution, similar values for conversion evolution and MSD. Systems 1 and 3 were based in bulk polymerization mediated by linear initiator. Whereas System 1 was probed by fluorescent linear initiator 3, System 3 was probed by fluorescent star-shaped initiator 4. On the other hand, the bulk polymerization of System 2 was obtained by star-shaped initiator and probed by star-shaped initiators. Therefore, during the polymerization progress, viscosity seems to have the predominant role in the determination of the translational diffusion of polymer chains, which explains the similarities of dynamic properties of Systems 1 and 2, while System 3 proceeds in a different way.

REFERENCES

- 1 SIRO, I.; PLACKETT, D. Microfibrillated cellulose and new nanocomposite materials: a review. **Cellulose**, v. 17, n. 3, p. 459-494, 2010.
- 2 WU, C.-N. SAITO, T, F.; SHUJI, F, H.; AKIRA, I. Ultrastrong and high gas-barrier nanocellulose/clay-layered composites. **Biomacromolecules**, v. 13, n. 6, p. 1927-1932, 2012.
- 3 XIE, K.; YU, Y.; SHI, Y. Synthesis and characterization of cellulose/silica hybrid materials with chemical crosslinking. **Carbohydrate Polymers**, v. 78, n. 4, p. 799-805, 2009.
- 4 SAKA, S.; GORING, D. A. I. The distribution of lignin in white birch wood as determined by bromination with tem-edxa. **Holzforschung**, v. 42, n. 3, p. 149-153, 1988.
- 5 SUN, Y.; CHENG, J. Y. Hydrolysis of lignocellulosic materials for ethanol production: a review. **Bioresource Technology**, v. 83, n. 1, p. 1-11, 2002.
- 6 MOSIER, W, C.; DALE, B.; ELANDER, R.; LEE, Y, Y.; HOLTZAPPLE, M.; LADISCH, M. Features of promising technologies for pretreatment of lignocellulosic biomass. **Bioresource Technology**, v. 96, n. 6, p. 673-686, 2005.
- 7 KLEMM, D.; HEUBLEIN, B.; FINK, H, P.; BOHN, A. Cellulose: fascinating biopolymer and sustainable raw material. **Angewandte Chemie-International Edition**, v. 44, n. 22, p. 3358-3393, 2005.
- 8 DEMIRBAS, A. Biodiesel production from vegetable oils via catalytic and non-catalytic supercritical methanol transesterification methods. **Progress in Energy and Combustion Science**, v. 31, n. 5-6, p. 466-487, 2005.
- 9 DEMIRBAS, A. Progress and recent trends in biofuels. **Progress in Energy and Combustion Science**, v. 33, n. 1, p. 1-18, 2007.
- 10 SANTOS, F. A.; DE QUEIROZ, J, H.; COLODETTE, J, L.; FERNANDES, S. A.; GUIMARAES, V. M.; REZENDE, S. T. Potential of sugarcane straw for ethanol production. **Quimica Nova**, v. 35, n. 5, p. 1004-1010, 2012.
- 11 OLSSON, L.; HAHNHAGERDAL, B. Fermentation of lignocellulosic hydrolysates for ethanol production. **Enzyme and Microbial Technology**, v. 18, n. 5, p. 312-331, 1996.
- 12 LI, H.-Y.; SUN, S-N.; WANG, C-Z.; SUNA, R-C. Structural and dynamic changes of lignin in Eucalyptus cell walls during successive alkaline ethanol treatments. **Industrial Crops and Products**, v. 74, p. 200-208, 2015.
- 13 KANBAYASHI, T.; MIYAFUJI, H. Topochemical and morphological characterization of wood cell wall treated with the ionic liquid, 1-ethylpyridinium bromide. **Planta**, v. 242, n. 3, p. 509-518, 2015.

- 14 LI, H.-Y.; SUN, S.-N.; ZHOU, X.; PENG, F.; SUN, R.-C. Structural characterization of hemicelluloses and topochemical changes in Eucalyptus cell wall during alkali ethanol treatment. **Carbohydrate Polymers**, v. 123, p. 17-26, 5 2015.
- 15 COLETTA, V. C.; REZENDE, C. .; DA CONCEICAO, F. R.; POLIKARPOV, I.; GONTIJO GUIMARAES, F. E. Mapping the lignin distribution in pretreated sugarcane bagasse by confocal and fluorescence lifetime imaging microscopy. **Biotechnology for Biofuels**, v. 6, 2013.
- 16 CALLIS, P. R. On the theory of 2-photon induced fluorescence anisotropy with application to indoles. **Journal of Chemical Physics**, v. 99, n. 1, p. 27-37, 1993.
- 17 CLAPP, A. R.; PONS, T.; MEDINTZ, I. L.; DELEHANTY, J. B.; MELINGER, J. S.; TIEFENBRUNN, T.; DAWSON, P. E.; FISHER, B. R.; O'ROURKE, B.; MATTOUSSI, H. Two-photon excitation of quantum-dot-based fluorescence resonance energy transfer and its applications. **Advanced Materials**, v. 19, n. 15, p. 1921, 2007.
- 18 DENK, W.; STRICKLER, J. H.; WEBB, W. W. 2-photon laser scanning fluorescence microscopy. **Science**, v. 248, n. 4951, p. 73-76, 1990.
- 19 HELMCHEN, F.; DENK, W. Deep tissue two-photon microscopy. **Nature Methods**, v. 2, n. 12, p. 932-940, 2005.
- 20 KONIG, K. Multiphoton microscopy in life sciences. **Journal of Microscopy-Oxford**, v. 200, p. 83-104, 2000.
- 21 VAZQUEZ-COOZ, I.; MEYER, R. W. A differential staining method to identify lignified and unlignified tissues. **Biotechnic & Histochemistry**, v. 77, n. 5-6, p. 277-282, 2002.
- 22 HOROBIN, R. **Conn's Biological Stains: A handbook of dyes, stains and fluorochromes for use in biology and medicine.** Oxford: Taylor and Francis, 2002. p.125-148.
- 23 BOND, J.; DONALDSON, L. Safranin fluorescent staining of wood cell walls. **Biotechnic & Histochemistry**, v. 83, n. 3-4, p. 161-171, 2008.
- 24 GRAY, K. A. Cellulosic ethanol - state of the technology. **International Sugar Journal**, v. 109, n. 1299, p. 145, 2007.
- 25 OLMSTEAD, J. A.; GRAY, D. G. Fluorescence emission from mechanical pulp sheets. **Journal of Photochemistry and Photobiology a-Chemistry**, v. 73, n. 1, p. 59-65, 1993.
- 26 OLMSTEAD, J. A.; GRAY, D. G. Fluorescence spectroscopy of cellulose, lignin and mechanical pulps: A review. **Journal of Pulp and Paper Science**, v. 23, n. 12, p. J571-J581, 1997.
- 27 HAUSTEIN, E.; SCHWILLE, P. Fluorescence correlation spectroscopy: Novel variations of an established technique. **Annual Review of Biophysics and Biomolecular Structure**, v. 36, p. 151-169, 2007.
- 28 SINGH, A. P.; SCHMITT, U.; MOLLER, R.; DAWSON, B. S. W.; KOCH, G. Ray tracheids in pinus radiata are more highly resistant to soft rot as compared to axial tracheids: relationship to lignin concentration. **Wood Science and Technology**, v. 40, n. 1, p. 16-25, 2006.

- 29 SPERANZA, G. A.; DEL RIO, J. C.; BETTUCCI, L.; MARTINEZ, A. T.; MARTINEZ, M. J. Sterols and lignin in eucalyptus globulus Labill. wood: spatial distribution and fungal removal as revealed by microscopy and chemical analyses. **Holzforschung**, v. 63, n. 3, p. 362-370, 2009.
- 30 CHUNDAWAT, S. P. S.; DONOHOE, B. S.; SOUSA, L. C.; ELDER, T.; AGARWAL, U. P.; LU, F.; RALPH, J.; HIMMEL, M. E.; BALAN, V.; DALE, B. E. Multi-scale visualization and characterization of lignocellulosic plant cell wall deconstruction during thermochemical pretreatment. **Energy & Environmental Science**, v. 4, n. 3, p. 973-984, 2011.
- 31 LU, P.; HSIEH, Y.-L. Preparation and properties of cellulose nanocrystals: Rods, spheres, and network. **Carbohydrate Polymers**, v. 82, n. 2, p. 329-336, 2010.
- 32 CHARREAU, H.; FORESTI, M. L.; VAZQUEZ, A. Nanocellulose patents trends: a comprehensive review on patents on cellulose nanocrystals, microfibrillated and bacterial cellulose. **Recent Patents on Nanotechnology**, v. 7, n. 1, p. 56-80, 2013.
- 33 SAMIR, M.; ALLOIN, F.; DUFRESNE, A. Review of recent research into cellulosic whiskers, their properties and their application in nanocomposite field. **Biomacromolecules**, v. 6, n. 2, p. 612-626, 2005.
- 34 HABIBI, Y.; LUCIA, L. A.; ROJAS, O. J. Cellulose nanocrystals: chemistry, self-assembly, and applications. **Chemical Reviews**, v. 110, n. 6, p. 3479-3500, 2010.
- 35 PENG, B. L.; DHAR, N.; LIU, H. L.; TAM, K. C. Chemistry and applications of nanocrystalline cellulose and its derivatives: a nanotechnology perspective. **Canadian Journal of Chemical Engineering**, v. 89, n. 5, p. 1191-1206, 2011.
- 36 YE, D. Preparation of nanocellulose. **Progress in Chemistry**, v. 19, n. 10, p. 1568-1575, 2007.
- 37 GARDNER, D. J.; OPORTO, G. S.; MILLS, R.; SAMIR, M. A. S. A. Adhesion and surface issues in cellulose and nanocellulose. **Journal of Adhesion Science and Technology**, v. 22, n. 5-6, p. 545-567, 2008.
- 38 SANDQUIST, D. New horizons for microfibrillated cellulose. **Appita Journal**, v. 66, n. 2, p. 156-162, 2013.
- 39 BROWNING, B. L. **Methods on wood chemistry**. New York: Interscience, 1967.p. 75-269.
- 40 LENCIONE, D. **Grupo de Fluorescência Molecular**. 2016. Disponível em: <<http://gfm.iqsc.usp.br/pesquisa/equipamentos/>>. Acesso em: 15 fev. 2016.
- 41 LENCIONE, D.; GEHLEN, M. H.; TRUJILLO, L. N.; LEITAO, R. C. F.; ALBUQUERQUE, R. Q. The spatial distribution of the photostability of thionine in zeolite L nanochannels investigated by Photobleaching Lifetime Imaging Microscopy. **Photochemical & Photobiological Sciences**, v. 15, n. 3, p. 398-404, 2016.

- 42 NOVAES, R. C.; TEIXEIRA, F. M.; PERRONE, C.C.; SANT'ANNA, C.; DE SOUZA, W.; ABUD, Y.; DA SILVA BON, E. P. FERREIRA-LEITAO, V. Structural evaluation of sugar cane bagasse steam pretreated in the presence of CO₂ and SO₂. **Biotechnology for Biofuels**, v. 5, 2012.
- 43 CHIMENEZ, T. A.; GEHLEN, M. H.; MARABEZI, K.; CURVELO, A. A. S. Characterization of sugarcane bagasse by autofluorescence microscopy. **Cellulose**, v. 21, n. 1, p. 653-664, 2014.
- 44 HARTER, K.; MEIXNER, A. J.; SCHLEIFENBAUM, F. Spectro-microscopy of living plant cells. **Molecular Plant**, v. 5, n. 1, p. 14-26, 2012.
- 45 CHENG, P. C.; KAO, F. J.; SUN, C. K.; LIN, B. L.; LIU, T. M.; WANG, Y. S.; HUANG, M. K. WANG, Y. M.; CHEN, J. C.; JOHNSON, I. Multiphoton excited fluorescence spectra of common bio-probes. **Scanning**, v. 22, n. 3, p. 187-188, 2000.
- 46 BENEDIKTYOVA, Z.; NEDBAL, L. Imaging of multi-color fluorescence emission from leaf tissues. **Photosynthesis Research**, v. 102, n. 2-3, p. 169-175, 2009.
- 47 CHENG, P. C.; PAN, S. J.; SHIH, A.; KIM, K. S.; LIOU, W. S.; PARK, M. S.. Highly efficient upconverters for multiphoton fluorescence microscopy. **Journal of Microscopy-Oxford**, v. 189, p. 199-212, 1998.
- 48 CHENG, P. C.; LIN, B. L.; KAO, F. J.; SUN, C. K.; WANG, Y. S.; LIU, T. M.; WAN, Y. M.; CHEN, J. C.; HUANG, M. K.; JOHNSON, I. Multi-photon fluorescence spectroscopy of fluorescent bio-probes and bio-molecules. In: ALFANO, R. R; HO, P. P.; CHIOU, A. E. T. (Ed). **Optical Sensing, Imaging, and Manipulation for Biological and Biomedical Applications**, 2000. p. 26-91. (Proceedings of SPIE, 4082).
- 49 ULRICH, V.; FISCHER, P.; RIEMANN, I.; KONIG, K. Compact multiphoton/single photon laser scanning microscope for spectral imaging and fluorescence lifetime imaging. **Scanning**, v. 26, n. 5, p. 217-225, 2004.
- 50 HESKES, A. M.; LINCOLN, C. N.; GOODGER, J. Q. D.; WOODROW, I. E.; SMITH, T. A. Multiphoton fluorescence lifetime imaging shows spatial segregation of secondary metabolites in Eucalyptus secretory cavities. **Journal of Microscopy**, v. 247, n. 1, p. 33-42, 2012.
- 51 CASTELLAN, A.; DAVIDSON, R. S. Steady-state and dynamic fluorescence emission from abies wood. **Journal of Photochemistry and Photobiology a-Chemistry**, v. 78, n. 3, 1994.
- 52 SCHWILLE, P.; HAUPTS, U.; MAITI, S.; WEBB, W. W. Molecular dynamics in living cells observed by fluorescence correlation spectroscopy with one- and two-photon excitation. **Biophysical Journal**, v. 77, n. 4, p. 2251-2265, 1999.
- 53 ALBINSSON, B.; LI, S. M.; LUNDQUIST, K.; STOMBERG, R. The origin of lignin fluorescence. **Journal of Molecular Structure**, v. 508, n. 1-3, p. 19-27, 1999.
- 54 BILLINTON, N.; KNIGHT, A. W. Seeing the wood through the trees: A review of techniques for distinguishing green fluorescent protein from endogenous autofluorescence. **Analytical Biochemistry**, v. 291, n. 2, p. 175-197, 2001.

- 55 HAFREN, J.; OOSTERVELD-HUT, H. M. J. Fluorescence lifetime imaging microscopy study of wood fibers. **Journal of Wood Science**, v. 55, n. 3, p. 236-239, 2009.
- 56 CASTELLAN, A.; RUGGIERO, R.; FROLLINI, E.; RAMOS, L. A.; CHIRAT, C. Studies on fluorescence of cellulose. **Holzforschung**, v. 61, n. 5, p. 504-508, 2007.
- 57 DONALDSON, L.; RADOTIC, K.; KALAUZI, A.; DJIKANOVIC, D.; JEREMIC, M. Quantification of compression wood severity in tracheids of *Pinus radiata* D. Don using confocal fluorescence imaging and spectral deconvolution. **Journal of Structural Biology**, v. 169, n. 1, p. 106-115, 2010.
- 58 JONOBI, M.; OLADI, R.; DAVOUDPOUR, Y.; OKSMAN, K.; DUFRESNE, A.; HAMZEH, Y.; DAVOODI, R. Different preparation methods and properties of nanostructured cellulose from various natural resources and residues: a review. **Cellulose**, v. 22, n. 2, p. 935-969, 2015.
- 59 MOON, S.-J.; EOM, IN-YONG.; KIM, J.-Y.; KIM, T.-S.; LEE, S. M.; CHOI, I.-G. CHOI, JOON WEON. Characterization of lignin-rich residues remaining after continuous super-critical water hydrolysis of poplar wood (*Populus alba*) for conversion to fermentable sugars. **Bioresource Technology**, v. 102, n. 10, p. 5912-5916, 2011.
- 60 ELAZZOUI-HAFRAOUI, S.; NISHIYAMA, Y.; PUTAUX, J. L.; HEUX, L.; DUBREUIL, F.; ROCHAS, C. The shape and size distribution of crystalline nanoparticles prepared by acid hydrolysis of native cellulose. **Biomacromolecules**, v. 9, n. 1, p. 57-65, 2008.
- 61 WANG, N.; DING, E.; CHENG, R. Preparation and 'liquid crystalline properties of spherical cellulose nanocrystals. **Langmuir**, v. 24, n. 1, p. 5-8, 2008.
- 62 GOELZER, F. D. E.; FARIA-TISCHER, P. C. S.; VITORINO, J. C.; SIERAKOWSKI, MARIA-R.; TISCHER, C. A. Production and characterization of nanospheres of bacterial cellulose from *Acetobacter xylinum* from processed rice bark. **Materials Science & Engineering C-Biomimetic and Supramolecular Systems**, v. 29, n. 2, p. 546-551, 2009.
- 63 FILSON, P. B.; DAWSON-ANDOH, B. E. Characterization of sugars from model and enzyme-mediated pulp hydrolyzates using high-performance liquid chromatography coupled to evaporative light scattering detection. **Bioresource Technology**, v. 100, n. 24, p. 6661-6664, 2009.
- 64 FILSON, P. B.; DAWSON-ANDOH, B. E. Sono-chemical preparation of cellulose nanocrystals from lignocellulose derived materials. **Bioresource Technology**, v. 100, n. 7, p. 2259-2264, 2009.
- 65 PANDEY, J. K.; KIM, CHUNG-SOO, C.; WON-SHIK, LEE.; CAROLINE, S. JANG.; DONG-YOUNG, A.; SUNG, HOON. Evaluation of morphological architecture of cellulose chains in grass during conversion from macro to nano dimensions. **E-Polymers**, 2009.
- 66 LAVOINE, N.; DESLOGES, I.; DUFRESNE, A.; BRAS, J. Microfibrillated cellulose - Its barrier properties and applications in cellulosic materials: A review. **Carbohydrate Polymers**, v. 90, n. 2, p. 735-764, 2012.
- 67 DUFRESNE, A. CELL 62-Cellulose whiskers reinforced polyvinyl alcohol copolymers nanocomposites. **Abstracts of Papers of the American Chemical Society**, v. 235, p. 25, 2008.

- 68 DUFRESNE, A. Processing of polymer nanocomposites reinforced with polysaccharide nanocrystals. **Molecules**, v. 15, n. 6, p. 4111-4128, 2010.
- 69 DURAN, N.; LEMES, A. P.; SEABRA, A. B. Review of cellulose nanocrystals patents: preparation, composites and general applications. **Recent Patents on Nanotechnology**, v. 6, n. 1, p. 16-28, 2012.
- 70 EICHHORN, S. J.; DUFRESNE, A.; ARANGUREN, M.; MARCOVICH, N. E.; CAPADONA, J. R.; ROWAN, S. J.; WEDER, C.; THIELEMANS, W.; ROMAN, M.; RENNECKAR, S.; GINDL, W.; VEIGEL, S.; KECKES, J.; YANO, H.; ABE, K.; NOGI, M.; NAKAGAITO, A. N.; MANGALAM, A. SIMONSEN, J.; BENIGHT, A. S.; BISMARCK, A.; BERGLUND, L. A.; PEIJS, T. Review: current international research into cellulose nanofibres and nanocomposites. **Journal of Materials Science**, v. 45, n. 1, p. 1-33, 2010.
- 71 HUBBE, M. A.; ROJAS, O. J. Colloidal stability and aggregation of lignocellulosic materials in aqueous suspension: a review. **Bioresources**, v. 3, n. 4, p. 1419-1491, 2008.
- 72 KLEMM, D.; KRAMER, F.; MORITZ, S.; LINDSTROM, T.; ANKERFORS, M.; GRAY, D.; DORRIS, A. Nanocelluloses: a new family of nature-based materials. **Angewandte Chemie-International Edition**, v. 50, n. 24, p. 5438-5466, 2011.
- 73 SAIN, M.; OKSMAN, K. Introduction to cellulose nanocomposites. **Cellulose Nanocomposites: Processing, Characterization, and Properties**, v. 938, p. 2-8, 2006.
- 74 SIQUEIRA, G.; BRAS, J.; DUFRESNE, A. Cellulosic bionanocomposites: a review of preparation, properties and applications. **Polymers**, v. 2, n. 4, p. 728-765, 2010.
- 75 VISAKH, P. M.; THOMAS, S. Preparation of bionanomaterials and their polymer nanocomposites from waste and biomass. **Waste and Biomass Valorization**, v. 1, n. 1, p. 121-134, 2010.
- 76 THIELEMANS, W.; WARBEY, C. R.; WALSH, D. A. Permselective nanostructured membranes based on cellulose nanowhiskers. **Green Chemistry**, v. 11, n. 4, p. 531-537, 2009.
- 77 JIANG, Z.; BERRY, R.; BOUCHARD, J.; AUDET, A. **Method of bonding comprises applying a nanocrystalline cellulose suspension between first and second surfaces, bringing the surfaces into contact with the suspension between them, and drying the suspension: Fpinnovations**. US n. 20110293932 A1, 1 dec. 2011.
- 78 SAMIR, M.; ALLOIN, F. SANCHEZ, J. Y.; DUFRESNE, A. Cellulose nanocrystals reinforced poly(oxyethylene). **Polymer**, v. 45, n. 12, p. 4149-4157, 2004.
- 79 SAMIR, M. A. S. A.; ALLOIN, F.; DUFRESNE, A. High performance nanocomposite polymer electrolytes. **Composite Interfaces**, v. 13, n. 4-6, p. 545-559, 2006.
- 80 SCHROERS, M.; KOKIL, A.; WEDER, C. Solid polymer electrolytes based on nanocomposites of ethylene oxide-epichlorohydrin copolymers and cellulose whiskers. **Journal of Applied Polymer Science**, v. 93, n. 6, p. 2883-2888, 2004.

81 FLEMING, K.; GRAY, D.; PRASANNAN, S.; MATTHEWS, S. Cellulose crystallites: A new and robust liquid crystalline medium for the measurement of residual dipolar couplings. **Journal of the American Chemical Society**, v. 122, n. 21, p. 5224-5225, 2000.

82 BEN DOUISSA, N.; BERGAOUI, L.; MANSOURI, S.; KHIARI, R.; MHENNI, M. F. Macroscopic and microscopic studies of methylene blue sorption onto extracted celluloses from *Posidonia oceanica*. **Industrial Crops and Products**, v. 45, p. 106-113, 2013.

83 CARREIRA, P.; MENDES, JOANA A. S.; TROVATTI, E.; SERAFIM, L. S.; FREIRE, C. S. R.; SILVESTRE, A. J. D. PASCOAL NETO, C. Utilization of residues from agro-forest industries in the production of high value bacterial cellulose. **Bioresource Technology**, v. 102, n. 15, p. 7354-7360, 2011.

84 MORAN, J. I.; ALVAREZ, V. A.; CYRAS, V. P.; VAZQUEZ, A. Extraction of cellulose and preparation of nanocellulose from sisal fibers. **Cellulose**, v. 15, n. 1, p. 149-159, 2008.

85 CHERIAN, B. M.; LEO, A. L.; DE SOUZA, S. F.; THOMAS, S.; POTHAN, L. A.; KOTTAISAMY, M. Isolation of nanocellulose from pineapple leaf fibres by steam explosion. **Carbohydrate Polymers**, v. 81, n. 3, p. 720-725, 2010.

86 MANDAL, A.; CHAKRABARTY, D. Isolation of nanocellulose from waste sugarcane bagasse (SCB) and its characterization. **Carbohydrate Polymers**, v. 86, n. 3, p. 1291-1299, 2011.

87 KAUSHIK, A.; SINGH, M. Isolation and characterization of cellulose nanofibrils from wheat straw using steam explosion coupled with high shear homogenization. **Carbohydrate Research**, v. 346, n. 1, p. 76-85, 2011.

88 ABITBOL, T.; PALERMO, A.; MORAN-MIRABAL, J. M.; CRANSTON, EMILY D. Fluorescent labeling and characterization of cellulose nanocrystals with varying charge contents. **Biomacromolecules**, v. 14, n. 9, p. 3278-3284, 2013.

89 GIERLINGER, N.; SCHWANNINGER, M. The potential of Raman microscopy and Raman imaging in plant research. **Spectroscopy-an International Journal**, v. 21, n. 2, p. 69-89, 2007.

90 HERMAN, B. Applications of fluorescence microscopy. **Microscopy handbooks**; fluorescence microscopy. 2. ed. United Kingdom: Bios Scientific Publishers, 1998. v. 40, p. 47-68.

91 VAN MUNSTER, E. B.; GADELLA, T. W. J. Fluorescence Lifetime Imaging Microscopy (FLIM). **Review. Adv Biochem Eng Biotechnology**. v. 95, p. 143-175 p. 2005.

92 HARKE, B.; KELLER, J.; ULLAL, C. K.; WESTPHAL, V.; SCHOENLE, A.; HELL, S. W. Resolution scaling in STED microscopy. **Optics Express**, v. 16, n. 6, p. 4154-4162, 2008. ISSN 1094-4087.

93 HOTTA, J.-I.; Fron, E.; DEDECKER, P.; JANSSEN, K. P. F.; LI, C.; MUELLEN, K.; HARKE, B.; BUECKERS, J.; HELL, S. W.; HOFKENS, J. Spectroscopic rationale for efficient stimulated-emission depletion microscopy fluorophores. **Journal of the American Chemical Society**, v. 132, n. 14, p. 5021, 2010.

- 94 WILLIG, K. I.; HARKE, B.; MEDDA, R.; HELL, S. W. STED microscopy with continuous wave beams. **Nature Methods**, v. 4, n. 11, p. 915-918, 2007.
- 95 MIN, W.; ENGLISH, B. P.; LUO, G. B.; CHERAYIL, B. J.; KOU, S. C.; XIE, X. S. Fluctuating enzymes: Lessons from single-molecule studies. **Accounts of Chemical Research**, v. 38, n. 12, p. 923-931, 2005.
- 96 MIZUNO, H.; ABE, M.; DEDECKER, P.; MAKINO, A.; ROCHA, S.; OHNO-IWASHITA, Y.; HOFKENS, J.; KOBAYASHI, T.; MIYAWAKI, A. Fluorescent probes for superresolution imaging of lipid domains on the plasma membrane. **Chemical Science**, v. 2, n. 8, p. 1548-1553, 2011.
- 97 CHEN, H. Z. Temperature cycling to improve the ethanol production with solid state simultaneous saccharification and fermentation. **Applied Biochemistry and microbiology**, v. 43, n.1, p. 57-60, 2007.
- 98 WADA, M.; HEUX, L.; SUGIYAMA, J. Polymorphism of cellulose I family: Reinvestigation of cellulose IV. **Biomacromolecules**, v. 5, n. 4, p. 1385-1391, 2004.
- 99 SEGAL, L.; CREELY, J.J.; MARTIN, A.E.; CONRAD, C. M. An empirical method for estimating the degree of crystallinity of native cellulose using the X-ray diffractometer. **Textile Research Journal**, v. 29, n. 10, p. 786-794, 1959.
- 100 PALMQVIST, E.; HAHN-HAGERDAL, B. Fermentation of lignocellulosic hydrolysates. II: inhibitors and mechanisms of inhibition. **Bioresource Technology**, v. 74, n. 1, p. 25-33, 2000.
- 101 GOUVEIA, E. R.; NASCIMENTO, R. T.; SOUTO-MAIOR, A. M. Validação de metodologia para a caracterização química de bagaço de cana-de-açúcar. **Química Nova**. Brazil. v. 32, 1500-1503 p, 2009.
- 102 PEPONI, L.; PUGLIA, D.; TORRE, L.; VALENTINI, L.; KENNY, J. M. Processing of nanostructured polymers and advanced polymeric based nanocomposites. **Materials Science & Engineering R-Reports**, v. 85, p. 1-46, 2014.
- 103 OJIJO, V.; RAY, S. S. Processing strategies in bionanocomposites. **Progress in Polymer Science**, v. 38, n. 10-11, p. 1543-1589, 2013.
- 104 LI, W. WU, Q.; ZHAO, X.; HUANG, Z.; CAO, J.; LI, J.; LIU, S. Enhanced thermal and mechanical properties of PVA composites formed with filamentous nanocellulose fibrils. **Carbohydrate Polymers**, v. 113, p. 403-410, 2014.
- 105 PARALIKARA, S. A.; SIMONSEN, J.; LOMBARDI, J. Poly(vinyl alcohol)/cellulose nanocrystal barrier membranes. **Journal of Membrane Science**, v. 320, n. 1-2, p. 248-258, 2008.
- 106 MONTAZER, M.; SHAMEI, A.; ALIMOHAMMADI, F. Synthesizing and stabilizing silver nanoparticles on polyamide fabric using silver-ammonia/PVP/UVC. **Progress in Organic Coatings**, v. 75, n. 4, p. 379-385, 2012.
- 107 XU, S.; SHI, Y. Low temperature high sensor response nano gas sensor using ITO nanofibers. **Sensors and Actuators B-Chemical**, v. 143, n. 1, p. 71-75, 2009.

- 108 SCHERMELLEH, L.; HEINTZMANN, R.; LEONHARDT, H. A guide to super-resolution fluorescence microscopy. **Journal of Cell Biology**, v. 190, n. 2, p. 165-175, 2010.
- 109 NAEGERL, U. V.; WILLIG, K. I.; HEIN, B.; HELL, S. W.; BONHOEFFER, T. Live-cell imaging of dendritic spines by STED microscopy. **Proceedings of the National Academy of Sciences of the United States of America**, v. 105, n. 48, p. 18982-18987, 2008.
- 110 AKHLAGHI, S. P.; ZAMAN, M.; MOHAMMED, N.; BRINATTI, C.; BATMAZ, R.; BERRY, R.; LOH, W.; TAM, K. C. Synthesis of amine functionalized cellulose nanocrystals: optimization and characterization. **Carbohydrate Research**, v. 409, p. 48-55, 2015.
- 111 LIMA, M. M. D.; BORSALI, R. Rodlike cellulose microcrystals: Structure, properties, and applications. **Macromolecular Rapid Communications**, v. 25, n. 7, p. 771-787, 2004.
- 112 ROSILO, H.; MCKEE, J. R.; KONTTURI, E.; KOHO, T.; HYTONEN, V. P.; IKKALA, O.; KOSTIAINEN, M. A. Cationic polymer brush-modified cellulose nanocrystals for high-affinity virus binding. **Nanoscale**, v. 6, n. 20, p. 11871-11881, 2014.
- 113 HABIBI, Y.; CHANZY, H.; VIGNON, M. R. TEMPO-mediated surface oxidation of cellulose whiskers. **Cellulose**, v. 13, n. 6, p. 679-687, 2006.
- 114 GOUSSE, C. CHANZY, H.; EXCOFFIER, G.; SOUBEYRAND, L.; FLEURY, E. Stable suspensions of partially silylated cellulose whiskers dispersed in organic solvents. **Polymer**, v. 43, n. 9, p. 2645-2651, 2002.
- 115 ELBIALY, N.; ABDELHAMID, M.; YOUSSEF, T. Low power argon laser-induced thermal therapy for subcutaneous ehrlich carcinoma in mice using spherical gold nanoparticles. **Journal of Biomedical Nanotechnology**, v. 6, n. 6, p. 687-693, 2010.
- 116 LU, J.; ASKELAND, P.; DRZAL, L. T. Surface modification of microfibrillated cellulose for epoxy composite applications. **Polymer**, v. 49, n. 5, p. 1285-1296, 2008.
- 117 WANG, W.-J.; WANG, W.-W.; SHAO, Z.-Q. Surface modification of cellulose nanowhiskers for application in thermosetting epoxy polymers. **Cellulose**, v. 21, n. 4, p. 2529-2538, 2014.
- 118 DONG, S.; ROMAN, M. Fluorescently labeled cellulose nanocrystals for bioimaging applications. **Journal of the American Chemical Society**, v. 129, n. 45, p. 13810, 2007.
- 119 GORGIEVA, S.; VOGRINCIC, R.; KOKOL, V. Polydispersity and assembling phenomena of native and reactive dye-labelled nanocellulose. **Cellulose**, v. 22, n. 6, p. 3541-3558, 2015.
- 120 NAVARRO, J. R. G.; CONZATTI, G.; YU, Y.; FALL, A. B.; MATHEW, R.; EDEN, M.; BERGSTROM, L. Multicolor fluorescent labeling of cellulose nanofibrils by click chemistry. **Biomacromolecules**, v. 16, n. 4, p. 1293-1300, 2015.
- 121 EDWARDS, J. V.; PREVOST, N.; SETHUMADHAVAN, K.; ULLAH, A.; CONDON, B. Peptide conjugated cellulose nanocrystals with sensitive human neutrophil elastase sensor activity. **Cellulose**, v. 20, n. 3, p. 1223-1235, 2013.

- 122 SCHYRR, B.; PASCHE, S.; VOIRIN, G.; WEDER, C.; SIMON, Y. C.; FOSTER, E. J. Biosensors Based on Porous Cellulose Nanocrystal-Poly(vinyl Alcohol) Scaffolds. **Acs Applied Materials & Interfaces**, v. 6, n. 15, p. 12674-12683, 2014.
- 123 NAVARRO, J. R. G.; BERGSTROM, L. Labelling of N-hydroxysuccinimide-modified rhodamine B on cellulose nanofibrils by the amidation reaction. **Rsc Advances**, v. 4, n. 105, p. 60757-60761, 2014.
- 124 KOLB, H. C.; FINN, M. G.; SHARPLESS, K. B. Click chemistry: Diverse chemical function from a few good reactions. **Angewandte Chemie-International Edition**, v. 40, n. 11, p. 2004, 2001.
- 125 NEBHANI, L.; BARNER-KOWOLLIK, C. Orthogonal Transformations on Solid Substrates: Efficient Avenues to Surface Modification. **Advanced Materials**, v. 21, n. 34, p. 3442-3468, 2009.
- 126 JENNINGS, L. E.; LONG, N. J. 'Two is better than one'-probes for dual-modality molecular imaging. **Chemical Communications**, n. 24, p. 3511-3524, 2009.
- 127 HUBER, M. M. Staubli, A. B.; KUSTEDJO, K.; GRAY, M. H. B.; SHIH, J.; FRASER, S. E.; JACOBS, R. E.; MEADE, T. J. Fluorescently detectable magnetic resonance imaging agents. **Bioconjugate Chemistry**, v. 9, n. 2, p. 242-249, 1998.
- 128 BODUNOV, E. N.; BERBERAN-SANTOS, M. N.; MARTINHO, J. M. G. Electronic energy transfer in linear polymers randomly labelled with chromophores. **Chemical Physics**, v. 274, n. 2-3, p. 243-253, 2001.
- 129 KRICHEVSKY, O.; BONNET, G. Fluorescence correlation spectroscopy: the technique and its applications. **Reports on Progress in Physics**, v. 65, n. 2, p. 251-297, 2002.
- 130 SCHWILLE, P. Fluorescence correlation spectroscopy and its potential for intracellular applications. **Cell Biochemistry and Biophysics**, v. 34, n. 3, p. 383-408, 2001.
- 131 LUSCHTINETZ, F.; DOSCHE, C. Determination of micelle diffusion coefficients with fluorescence correlation spectroscopy (FCS). **Journal of Colloid and Interface Science**, v. 338, n. 1, p. 312-315, 1 2009.
- 132 MAGDE, D.; WEBB, W. W.; ELSON, E. Thermodynamic fluctuations in a reacting system - measurement by fluorescence correlation spectroscopy. **Physical Review Letters**, v. 29, n. 11, p. 705-8, 1972.
- 133 MESETH, U.; WOHLAND, T.; RIGLER, R.; VOGEL, H. Resolution of fluorescence correlation measurements. **Biophysical Journal**, v. 76, n. 3, p. 1619-1631, 1999.
- 134 SAFFARIAN, S.; ELSON, E. L. Statistical analysis of fluorescence correlation spectroscopy: The standard deviation and bias. **Biophysical Journal**, v. 84, n. 3, p. 2030-2042, 2003.
- 135 FRINGUELLI, F.; PIERMATTI, O.; PIZZO, F.; VACCARO, L. Ring opening of epoxides with sodium azide in water. A regioselective pH-controlled reaction. **Journal of Organic Chemistry**, v. 64, n. 16, p. 6094-6096, 1999.

136 PAHIMANOLIS, N.; VESTERINEN, A-H.; RICH, J.; SEPPALA, J. Modification of dextran using click-chemistry approach in aqueous media. **Carbohydrate Polymers**, v. 82, n. 1, p. 78-82, 2010.

137 MUELLER, C. B.; LOMAN, A.; PACHECO, V.; KOBERLING, F.; WILLBOLD, D.; RICHTERING, W.; ENDERLEIN, J. Precise measurement of diffusion by multi-color dual-focus fluorescence correlation spectroscopy. **Epl**, v. 83, n. 4, p. 1-2, 2008.

138 ANDERSON, C. M.; GEORGIU, G. N.; MORRISON, I. E. G.; STEVENSON, G. V. W.; CHERRY, R. J. Tracking of cell-surface receptors by fluorescence digital imaging microscopy using a charge-coupled device camera - low-density-lipoprotein and influenza-virus receptor mobility at 4-degrees-C. **Journal of Cell Science**, v. 101, p. 415-425, 1992.

139 GRUNWALD, D.; CARDOSO, M. C.; LEONHARDT, H.; BUSCHMANN, V. Diffusion and binding properties investigated by Fluorescence Correlation Spectroscopy (FCS). **Current Pharmaceutical Biotechnology**, v. 6, n. 5, p. 381-386, 2005.

140 SAMIR, M.; ALLOIN, F.; SANCHEZ, J. Y.; EL KISSI, N.; DUFRESNE, A. Preparation of cellulose whiskers reinforced nanocomposites from an organic medium suspension. **Macromolecules**, v. 37, n. 4, p. 1386-1393, 2004.

141 MASON, T. G. Estimating the viscoelastic moduli of complex fluids using the generalized Stokes-Einstein equation. **Rheologica Acta**, v. 39, n. 4, p. 371-378, 2000.

142 YAMAMOTO, R.; ONUKI, A. Dynamics of highly supercooled liquids: Heterogeneity, rheology, and diffusion. **Physical Review E**, v. 58, n. 3, p. 3515-3529, 1998.

143 VAN LOKEREN, L.; CARTUYVELS, E.; ABSILLIS, G.; WILLEM, R.; PARAC-VOGT, T. N. Phosphoesterase activity of polyoxomolybdates: diffusion ordered NMR spectroscopy as a tool for obtaining insights into the reactivity of polyoxometalate clusters. **Chemical Communications**, n. 24, p. 2774-2776, 2008.

144 CANET, D.; LaST, A. M.; TITO, P.; SUNDE, M.; SPENCER, A.; REDFIELD, C.; ROBINSON, C. V.; DOBSON, C. M. The solution dynamics of amyloidogenic Asp67His variant of human lysozyme: Insights from hydrogen exchange. **Biophysical Journal**, v. 78, n. 1, p. 4A-4A, 2000.

145 ROPARS, V.; BOUGUET-BONNET, S.; AUGUIN, D.; BARTHE, P.; CANET, DL.; ROUMESTAND, C. Unraveling protein dynamics through fast spectral density mapping. **Journal of Biomolecular Nmr**, v. 37, n. 3, p. 159-177, 2007.

146 BALINOV, B.; OLSSON, U.; SODERMAN, O. Structural similarities between the I3 and bicontinuous cubic phases in the aot-brine system. **Journal of Physical Chemistry**, v. 95, n. 15, p. 5931-5936, 1991.

147 ARAKI, J.; WADA, M.; KUGA, S.; OKANA, T. Influence of surface charge on viscosity behavior of cellulose microcrystal suspension. **Journal of Wood Science**, v. 45, n. 3, p. 258-261, 1999.

- 148 FLIER, B. M. I.; BAIER, M.; HUBER, J.; MUELLEN, K.; MECKING, S.; ZUMBUSCH, A.; WOELL, D. Single molecule fluorescence microscopy investigations on heterogeneity of translational diffusion in thin polymer films. **Physical Chemistry Chemical Physics**, v. 13, n. 5, p. 1770-1775, 2011.
- 149 DEBUIGNE, A.; HURTGEN, M.; DETREMBLEUR, C.; JEROME, C.; BARNER-KOWOLLIK, C.; JUNKERS, T. Interpolymer radical coupling: A toolbox complementary to controlled radical polymerization. **Progress in Polymer Science**, v. 37, n. 7, p. 1004-1030, 2012.
- 150 GEORGES, M. K.; VEREGIN, R. P. N.; KAZMAIER, P. M.; HAMER, G. K. Narrow molecular-weight resins by a free-radical polymerization process. **Macromolecules**, v. 26, n. 11, p. 2987-2988, 1993.
- 151 SCIANNAMEA, V.; JEROME, R.; DETREMBLEUR, C. In-situ nitroxide-mediated radical polymerization (NMP) processes: Their understanding and optimization. **Chemical Reviews**, v. 108, n. 3, p. 1104-1126, 2008.
- 152 BRAUNECKER, W. A.; MATYJASZEWSKI, K. Controlled/living radical polymerization: Features, developments, and perspectives. **Progress in Polymer Science**, v. 32, n. 1, p. 93-146, 2007.
- 153 OUCHI, M.; TERASHIMA, T.; SAWAMOTO, M. Transition metal-catalyzed living radical polymerization: toward perfection in catalysis and precision polymer synthesis. **Chemical Reviews**, v. 109, n. 11, p. 4963-5050, 2009.
- 154 DI LENA, F.; MATYJASZEWSKI, K. Transition metal catalysts for controlled radical polymerization. **Progress in Polymer Science**, v. 35, n. 8, p. 959-1021, Aug 2010.
- 155 MOAD, G.; RIZZARDO, E.; THANG, S. H. Toward living radical polymerization. **Accounts of Chemical Research**, v. 41, n. 9, p. 1133-1142, 2008.
- 156 DAVID, G.; BOYER, C.; TONNAR, J.; AMEDURI, B.; LACROIX-DESMAZES, P.; BOUTEVIN, B. Use of iodocompounds in radical polymerization. **Chemical Reviews**, v. 106, n. 9, p. 3936-3962, 2006.
- 157 POLI, R.; ALLAN, L. E. N.; SHAVER, M. P. Iron-mediated reversible deactivation controlled radical polymerization. **Progress in Polymer Science**, v. 39, n. 10, p. 1827-1845, 2014.
- 158 HURTGEN, M.; DETREMBLEUR, C.; JEROME, C.; DEBUIGNE, A. Insight into organometallic-mediated radical polymerization. **Polymer Reviews**, v. 51, n. 2, p. 188-213, 2011.
- 159 DELPLACE, V.; GUEGAIN, E.; HARRISSON, S.; GIGMES, D.; GUILLANEUF, Y.; NICOLAS, J. A ring to rule them all: a cyclic ketene acetal comonomer controls the nitroxide-mediated polymerization of methacrylates and confers tunable degradability. **Chemical Communications**, v. 51, n. 64, p. 12847-12850, 2015 2015.
- 160 MATYJASZEWSKI, K.; TSAREVSKY, N. V. Macromolecular engineering by atom transfer radical polymerization. **Journal of the American Chemical Society**, v. 136, n. 18, p. 6513-6533, 2014.

- 161 MCKENZIE, T. G.; FU, Q.; WONG, E. H. H.; DUNSTAN, D. E.; QIAO, G. G. Visible light mediated controlled radical polymerization in the absence of exogenous radical sources or catalysts. **Macromolecules**, v. 48, n. 12, p. 3864-3872, 2015.
- 162 PASQUALE, A. J.; LONG, T. E. Synthesis of star-shaped polystyrenes via nitroxide-mediated stable free-radical polymerization. **Journal of Polymer Science Part a-Polymer Chemistry**, v. 39, n. 1, p. 216-223, 2001.
- 163 NICOLAS, J. GUILLANEUF, Y.; LEFAY, C.; BERTIN, D.; GIGMES, D.; CHARLEUX, B. Nitroxide-mediated polymerization. **Progress in Polymer Science**, v. 38, n. 1, p. 63-235, 2013.
- 164 MIN, K.; GAO, H. F.; MATYJASZEWSKI, K. Preparation of homopolymers and block copolymers in miniemulsion by ATRP using activators generated by electron transfer (AGET). **Journal of the American Chemical Society**, v. 127, n. 11, p. 3825-3830, 2005.
- 165 CHIEFARI, J. CHONG, Y. K.; ERCOLE, F.; KRSTINA, J.; JEFFERY, J.; LE, T. P. T.; MAYADUNNE, R. T. A.; MEIJS, G. F.; MOAD, C. L.; MOAD, G.; RIZZARDO, E.; THANG, S. H. Living free-radical polymerization by reversible addition-fragmentation chain transfer: The RAFT process. **Macromolecules**, v. 31, n. 16, p. 5559-5562, 1998.
- 166 HILL, M. R.; CARMEAN, R. N.; SUMERLIN, B. S. Expanding the scope of raft polymerization: recent advances and new horizons. **Macromolecules**, v. 48, n. 16, p. 5459-5469, 2015.
- 167 SUGIHARA, S.; KONEGAWA, N.; MAEDA, Y. HCl.Et₂O-catalyzed metal-free raft cationic polymerization: one-pot transformation from metal-free living cationic polymerization to raft radical polymerization. **Macromolecules**, v. 48, n. 15, p. 5120-5131, 2015.
- 168 YAMAGO, S. Precision polymer synthesis by degenerative transfer controlled/living radical polymerization using organotellurium, organostibine, and organobismuthine chain-transfer agents. **Chemical Reviews**, v. 109, n. 11, p. 5051-5068, 2009.
- 169 ROSEN, B. M.; PERCEC, V. Single-electron transfer and single-electron transfer degenerative chain transfer living radical polymerization. **Chemical Reviews**, v. 109, n. 11, p. 5069-5119, 2009.
- 170 CHAMPOURET, Y. MACLEOD, K. C.; SMITH, K. M.; PATRICK, B. O.; POLI, R. Controlled radical polymerization of vinyl acetate with cyclopentadienyl chromium, beta-diketiminato complexes: atrp vs omrp. **Organometallics**, v. 29, n. 14, p. 3125-3132, 2010.
- 171 POLI, R.; SHAVER, M. P. Atom transfer radical polymerization (atrp) and organometallic mediated radical polymerization (omrp) of styrene mediated by diamino bis(phenolato)iron(II) complexes: a dft study. **Inorganic Chemistry**, v. 53, n. 14, p. 7580-7590, 2014.
- 172 POLI, R. New phenomena in organometallic-mediated radical polymerization (omrp) and perspectives for control of less active monomers. **Chemistry-a European Journal**, v. 21, n. 19, p. 6988-7001, 2015.
- 173 FISCHER, H. The persistent radical effect: a principle for selective radical reactions and living radical polymerizations. **Chemical Reviews**, v. 101, n. 12, p. 3581-3610, 2001.

174 WOLL, D.; UJI-I, H.; SCHNITZLER, T.; HOTTA, J. I.; DEDECKER, P.; HERRMANN, A.; DE SCHRYVER, F. C.; MULLEN, K.; HOFKENS, J. Radical polymerization tracked by single molecule spectroscopy. **Angewandte Chemie International Edition**, v. 47, n. 4, p. 783-7, 11, 2008.

175 STEMPFLE, B.; DILL, M.; WINTERHALDER, M. J.; MÜLLEN, K.; WÖLL, D. Single molecule diffusion and its heterogeneity during the bulk radical polymerization of styrene and methyl methacrylate. **Polymer Chemistry**, v. 3, n. 9, p. 2456-2463, 2012.

176 WOLL, D.; UJI-I, H.; SCHNITZLER, T.; HOTTA, J. I.; DEDECKER, P.; HERRMANN, A.; DE SCHRYVER, F. C.; MULLEN, K.; HOFKENS, J. Polymers and single molecule fluorescence spectroscopy, what can we learn? **Chemical Society Reviews**, v. 38, n. 2, p. 313-328, 2009.

177 YAMADA, B.; WESTMORELAND, D. G.; KOBATAKE, S.; KONOSU, O. ESR spectroscopic studies of radical polymerization. **Progress in Polymer Science**, v. 24, n. 4, p. 565-630, 1999.

178 SCHWEER, J.; SARNECKI, J.; MAYERPOSNER, F.; MULLEN, K.; RADER, H. J.; SPICKERMANN, J. Pulsed-laser polymerization/matrix-assisted laser desorption/ionization mass spectrometry: An approach toward free-radical propagation rate coefficients of ultimate accuracy? **Macromolecules**, v. 29, n. 13, p. 4536-4543, 1996.

179 HEATLEY, F.; LOVELL, P. A.; MCDONALD, J. Nmr-studies of free-radical polymerization and copolymerization of monomers and polymers containing allyl groups. **European Polymer Journal**, v. 29, n. 2-3, p. 255-268, 1993.

180 BOSCH, P.; CATALINA, F.; CORRALES, T.; PEINADO, C. Fluorescent probes for sensing processes in polymers. **Chemistry-a European Journal**, v. 11, n. 15, p. 4314-4325, 2005.

181 LOUTFY, R. O. Fluorescence probes for polymer free-volume. **Pure and Applied Chemistry**, v. 58, n. 9, p. 1239-1248, 1986.